FEDERAL UNIVERSITY OF TECHNOLOGY - PARANÁ
GRADUATE PROGRAM IN ELECTRICAL AND COMPUTER
ENGINEERING

LUÍS FELIPE SILVEIRA BOTTON

**TWIN DIRECT-IMAGING SENSOR FOR FLOW VELOCITY
PROFILING IN TWO-PHASE MIXTURES**

MASTER THESIS

CURITIBA

2019

LUÍS FELIPE SILVEIRA BOTTON

TWIN DIRECT-IMAGING SENSOR FOR FLOW VELOCITY PROFILING IN TWO-PHASE MIXTURES

Master Thesis submitted to the Graduate Program in Electrical and Computer Engineering of Federal University of Technology - Paraná as a partial requirement for the degree of "Master of Science"– Concentration Area: Automation and Systems Engineering.

Advisor: Prof. Marco Jose da Silva, Dr-ing

Co-advisor: Prof. Daniel R. Pipa, DSc

CURITIBA

2019

UTFPR

UNIVERSIDADE TECNOLÓGICA FEDERAL DO PARANÁ

CAMPUS CURITIBA

TERMO DE APROVAÇÃO DE DISSERTAÇÃO Nº 840

A Dissertação de Mestrado intitulada **Twin Direct-Imaging Sensor for Flow Velocity Profiling in Two-phase Mixtures** defendida em sessão pública pelo(a) candidato(a) **Luís Felipe Silveira Botton** no dia **10 de outubro de 2019**, foi julgada aprovada em sua forma final para a obtenção do título de Mestre em Ciências, Linha de Pesquisa – Sistemas de Mediação e Instrumentação, pelo Programa de Pós-Graduação em Engenharia Elétrica e Informática Industrial.

Banca examinadora:

Prof. Dr. Marco José da Silva - (UTFPR) - Orientador

Prof. Dr. Eduardo Nunes dos Santos - (UTFPR)

Prof. Dr. Eduardo Parente Ribeiro - (UFPR)

A via original deste documento encontra-se arquivada na Secretaria do Programa, contendo a assinatura da Coordenação após a entrega da versão corrigida do trabalho.

Curitiba, 10 de outubro de 2019.

_____
Carimbo e Assinatura do(a) Coordenador(a) do Programa

This work is dedicated to my wife Renata Cristina, who never stop believing.
La mia vita ti sei tu.

ACKNOWLEDGMENTS

If you want to find the secrets of the universe, think in terms of energy, frequency and vibration.
Nikola Tesla

ABSTRACT

BOTTON, Luís F.S.. TWIN DIRECT-IMAGING SENSOR FOR FLOW VELOCITY PROFILING IN TWO-PHASE MIXTURES. 105 f. Master Thesis – Graduate Program in Electrical and Computer Engineering, Federal University of Technology - Paraná. Curitiba, 2019.

The importance of multiphase flow measurement in many industries today is widely known. In the oil industry in particular, this type of flow is found within wells, flow lines and risers from the oil reservoir to the platform. Two-phase liquid-gas flow, a special type of multiphase flow formed by only liquid and gas phase, is of particular importance because of its recurrence and the effects produced in various processes and stages in oil exploration. Therefore, knowledge of flow parameters is fundamental for the design and sizing of production units and equipment, definition of constraints and efficiency parameters, process-related costs, safety factors for personnel and equipment. Traditional multiphase flow measurement techniques in the industrial environment are mainly based on the separation of multiphase flows into their different phases. Phase separation requires bulky, slow and expensive separators. This method has not satisfactorily met the increasing demands on oil production levels associated with stricter quality specifications and new exploration boundaries reached. Consequently, the development of a flow sensor for online and inline measurements is required to provide flow status information. To achieve this goal, a twin capacitive flow sensor called DIS was used in conjunction with a phase fraction sensitivity matrix and a spatial velocity sensitivity matrix. This study developed the spatial velocity sensitivity matrix by applying the inverse problem approach to the phase fraction sensitivity map of each DIS layer. In this strategy, the individual sensitivity of each upstream and downstream receiver was combined by the back-projection technique producing the spatial velocity sensitivity matrix. Then, the proposed technique was tested by processing synthetic data and experimental flow data with image reconstruction algorithms using the velocity sensitivity and original phase fraction matrices. This procedure allowed obtaining sufficient data to evaluate the velocity profile, the cross section of the gas phase distribution and, consequently, to estimate the gas phase volumetric flow rate by applying simple fluid mechanics equation. The results show that the new technique presented is viable, well adaptable and has great potential. Although it has explicit flow pattern dependence, for some flow conditions the method can achieve results with a deviation of less than 5% and, on average, gas flow is within 20% uncertainty.

Keywords: Multiphase flow, Tomography, Velocity profile, Flow rate estimation

RESUMO

BOTTON, Luís F.S.. SENSOR DUPLO PARA PERFILAMENTO DE VELOCIDADE EM MISTURAS BIFÁSICAS. 105 f. Master Thesis – Graduate Program in Electrical and Computer Engineering, Federal University of Technology - Paraná. Curitiba, 2019.

A importância da medição de fluxo multifásica em muitas indústrias hoje é amplamente conhecida. Na indústria de petróleo, em particular, esse tipo de fluxo é encontrado nos poços, linhas de produção e risers dos reservatórios de óleo para a plataforma. O escoamento bifásico gás-líquido, um tipo especial de fluxo multifásico formado apenas pela fase líquida e gasosa, é de particular importância devido à sua recorrência e aos efeitos produzidos em vários processos e estágios da exploração de petróleo. Portanto, o conhecimento dos parâmetros desse tipo de fluxo é fundamental para o design e dimensionamento de unidades e equipamentos de produção, definição de restrições e parâmetros de eficiência, dos custos relacionados ao processo, de fatores de segurança para pessoal e equipamento. As técnicas tradicionais de medição de fluxo multifásico no ambiente industrial baseiam-se principalmente na separação dos fluxos multifásicos em suas diferentes fases. A separação de fases requer separadores volumosos, lentos e de elevado custo de fabricação. Esse método não vem atendendo satisfatoriamente às crescentes demandas nos níveis de produção de petróleo associadas às especificações mais estritas de qualidade e aos novos limites de exploração alcançados. Consequentemente, é necessário o desenvolvimento de um sensor de fluxo para medições on-line e in-line para fornecer informações sobre o status do fluxo. Para atingir esse objetivo, um sensor de fluxo capacitivo duplo chamado DIS foi usado em conjunto com uma matriz de sensibilidade à fração de fase e uma matriz de sensibilidade à velocidade espacial. Este estudo desenvolveu a matriz de sensibilidade à velocidade espacial, aplicando a abordagem do problema inverso ao mapa de sensibilidade à fração de fase de cada layer do DIS. Nesta abordagem, a sensibilidade individual de cada receptor a montante e a jusante do sensor, foi combinada pela técnica back-projection produzindo a matriz de sensibilidade à velocidade espacial. Em seguida, a metodologia proposta foi testada por meio do processamento de dados de escoamento sintético e, depois, em dados experimentais, com diferentes algoritmos de reconstrução de imagem, utilizando as matrizes de sensibilidade à velocidade e à fração de fase. Esse procedimento permitiu obter dados suficientes para avaliar o perfil de velocidade, *i.e.*, a seção transversal da distribuição da fase gasosa e, conseqüentemente, estimar a vazão volumétrica da fase gasosa aplicando conceitos básicos da mecânica dos fluidos. Os resultados mostram que a nova técnica apresentada é viável, bem adaptável e com grande potencial. Embora tenha dependência explícita do padrão de escoamento, para alguns padrões de escoamento, o método obteve resultados com um desvio inferior a 5% em relação à referência e, em média, o desvio foi inferior a 20%.

Palavras-chave: Fluxo multifásico, Tomografia, Perfil de velocidade, Estimativa de vazão

LIST OF FIGURES

LIST OF TABLES

NOMENCLATURE

AC	Alternating Current
CAPES	Coordination for the Improvement of Higher Education Personnel
CPGEI	Graduate Program in Electrical and Computer Engineering
CT	Computerized Tomography
DAQ	Data Acquisition System
DC	direct current
DIS	Direct Image Sensor
ECT	Electrical Capacitance Tomography
ERT	Electrical Resistance Tomography
ET	Electrical Tomography
FBP	Filtered back Projection
FPCB	Flexible Printed-Circuit Board
IPT	Industrial Process Tomography
LASII	Laboratory of Sensors and Industrial Instrumentation
LBP	Linear Backprojection
LIM	Landweber's Iteration Method
MPFM	Multiphase Flow-Meter
NUEM	Multiphase Flow Research Center
NBP	Normalized Backprojection
PCB	Printed Circuit Board
PSD	point spread function
SAD	Sum of Absolute Differences
SSD	Sum of Squared Differences
UTFPR	Federal University of Technology - Paraná
WMS	Wire-Mesh Sensor

LIST OF SYMBOLS

ω	Angular frequency, radians per second ($^{rad}/_S$)
I	Current, Ampere (A)
Q	Electric charge, Coulomb(Q)
Γ	Electrodes surface, square meter (m^2)
q	Volumetric flow rate, cubic meter per second ($^{m^3}/_s$)
Z	Impedance, ohms (Ω)
$\varepsilon(x,y)$	Permittivity distribution, Farad per meter ($^F/_m$)
$\phi(x,y)$	Potential distribution, Volts (V)
α	Void fraction, percentage(%)
X	Reactance, ohms (Ω)
J_g	Superficial Velocity - gas phase, meter per second ($^m/_s$)
J_l	Superficial Velocity - liquid phase, meter per second ($^m/_s$)
R	Resistance, ohms (Ω)
V	Voltage, volts (V)

CONTENTS

1 INTRODUCTION

1.1 MOTIVATION

The importance of multiphase flow measurement in many industries today is widely known. In the oil industry in particular, this type of flow is found in the wells, flow lines and risers from the oil reservoirs to the platform (1). As multiphase flow, it is understood the concurrent stream of two, or more, immiscible substances that have different properties in restricted containers such as ducts, pipes, vessels or reactors.

In this context, a special type of multiphase flow formed only by a liquid and a gas phase, therefore called two-phase flow, is of particular importance. Among other reasons, the importance of two-phase flows is due to its recurrence in various processes and stages of oil exploration. Thus, knowledge of the characteristics of such flows is in demand, *e.g.*, when formed by the oil and gas phases parameters such phase fraction (α_p) ,superficial phase velocity (J_p) and flow pattern are required for design, scaling of production facilities and equipment, determining efficiency constraints, costs bound, safety factors of personnel and apparatus.

Also, increasing demands of oil production levels with more stringent product quality specifications and new frontiers of exploration that have been reached, *e.g.*, Brazil's pre-salt production area, are exponentially increasing the intensity and complexity of process during the last decades (2), which consequently increases the need for the development of technologies that meet these more restrict requirements.

The commercial measuring techniques for multiphase flow metering in the industrial environment are mostly based on the separation of the flows' different phases. The phase separation requires employing bulky, heavy and expensive separators as shown in Figure 1.1. Such process is expensive and time-consuming (3). For instance, after the phase separation, the measuring of the individual single-phase flows rate occurs employing differential pressure or variable area flow-meters as Pitot tubes, mechanical flow-meters as turbine or positive-displacement, electronic flow-meters as ultrasonic or magnetic flow meters among others (4) or yet, mass flow-meters as Coriolis.

Nevertheless, from the academic point of view, there is interest in the development of accurate measurement techniques to aid in better understanding the multiphase flow phenomenon, to refine and develop new multiphase flow models and to improve facilities flow control and management (3).

Therefore, as described, the development of flow sensors for inline and online measurements is currently desirable to eliminate the need for phase separators and providing immediate information on facilities and flow status. In this way solving the disadvantages

Figure 1.1: Illustration of three-phase separator used in oil industry

(a) Actual three-phase separator.
Source: Adapted from (5)
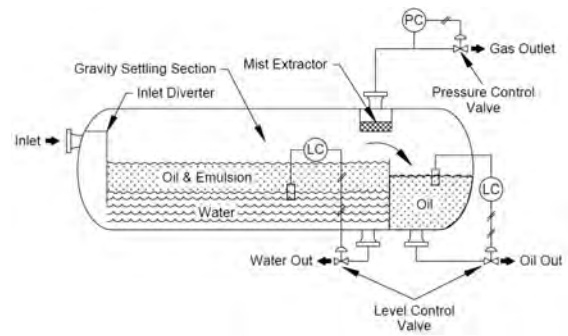
(b) Schematic of a horizontal three-phase separator with interface level control and weir.
Source: Adapted from (6)

of traditional methods and complying with modern efficiency standards requirements, for this purpose novel techniques are in search and development.

However, it is necessary to address some challenges posed by inline multiphase measurement. These challenges are largely related to the high degree of varying spatial distributions of the different phases concerning the flow path. Furthermore, the spatial distribution of different phases depends on many parameters such as fluids and pipes properties, *e.g.*, pipe size, pipe roughness, fluid density, fluid viscosity, etc. Hence, it is not trivial to measure all the phases simultaneously. For this reason, the algorithms behind MPFM (Multiphase Flow-Meter) commercial devices depend on empirical correlations, and we have not yet achieved high measurement accuracy in comparison with single-phase flow-meters.

While it is known that for a single phase flow Equation (1.1a), where A is the pipe cross-section area and v is the flow axial velocity, is relatively easily applicable. Also known that Equation (1.1a) can be adapted to the multiphase case by adding a term representing the phase fraction α_p yielding Equation (1.1b), where the index p indicates the phase, *e.g.*, gas (G) or liquid (L) (3).

$$Q = Av \tag{1.1a}$$

$$Q_p = A\alpha_p v_p \tag{1.1b}$$

This implies that, with the knowledge of the individual phase velocity, phase fraction and pipe cross-section area, it may be possible to estimate the flow rates of individual phases without the need of phase separation. One could state that the measurement of volume

fraction in multiphase flows has been for the most part resolved since many techniques such as gamma-ray densitometry and pressure transducers can produce highly reliable measurements independent of the operation mode (7) and, although dependent on operating conditions, techniques such as WMS (Wire-Mesh Sensor) an ERT (Electrical Resistance Tomography)can produce results with deviations below 20%.

Unfortunately, individual phase velocity measurement is still a hard task, as different phases in a multiphase flow may travel with different velocities and yet because the mentioned dependency of various parameters. The restriction on accurate estimation of the individual phase velocity given its complexity reflects in the work required to estimate the volumetric flow rate, q.

The set of techniques named Industrial Process Tomography (IPT) are characterized by the use of different physical properties of materials for remote sensing and recording phenomena data within process equipment (8), and generally consists of three main parts which are; hardware part, interfacing and software part (9). Tomography techniques have been in focus since the early 1990s. They provide the possibility of non-invasive, non-intrusive metering and generates rapid visualization of the internal structure of the flow process (10–12).

This work focuses attention on tomography techniques as a means of breakdown this deadlock involving individual phase velocity measurement. This characteristic of industrial process tomography of allowing non-invasive and non-intrusive measurement is valuable because it means that the flow is not disturbed during the measurement process and therefore its natural characteristic is preserved (13) , which are desired characteristics to multiphase flow measurement.

Depending on the process and characteristics of the materials under analysis, different modalities of tomography should be used. The IPT methods can be based on X-rays, gamma-rays, infrared radiation, ultrasound and electrical impedance (9). The Electrical Tomography techniques in turn can be divided into two modalities; ERT (Electrical Resistance Tomography) and ECT (Electrical Capacitance Tomography) (14).

Hence, ET has become a favored technique to obtain a cross-sectional image of the material flow in pipes (15). The ET techniques have many advantages over others, as not emitting ionizing radiation, robust and fast acquisitions and low cost. But, as cited by (14) there also difficulties, as a non-linear characteristic originated from a well know effect termed *soft field*. Once the electric field generated has low energy, its trajectory and magnitude are influenced by the environment. Solving these issues requires a lot of computational effort, so the problem is usually treated as linear with small disturbances.

However, the trade-off of these techniques is its dependence on image reconstruction algorithms, *i.e.*, the addition of complexity involved in the process since it involves an inverse problem solution (8, 13).

On the other hand, for the axial phase velocity, one of the most widely used techniques in multiphase flow are the ones based on similarity measurement between two time-series as, *e.g.*, spatial cross-correlation (3, 15).

Thus, the main motivation of this study is to evaluate the use of image reconstruction techniques within ECT to identify individual phase parameters and allow the use of Equation (1.1b) to estimating the dispersed phase flow, *i.e.*, the gas phase in this case. To do this, raw data provided by a non-invasive and non-intrusive sensor called DIS (Direct Image Sensor), which is a similar technique to ECT, will be processed to produce phase velocity and phase fraction concentration profiles, that together with the pipe cross-section are the terms of Equation (1.1b).

The DIS was introduced in earlier studies (16) for the fast direct-imaging of flow structures and comprises a twin array of 8 capacitive sensors. As a default of the DIS, the flow image is directly obtained by the interpretation of capacitive data from the sensors.

In this work, the sensor raw data will be treated by image reconstructing algorithms in order to obtain improved information on the phase fraction and, by correlating data from both layers of the sensor phase transit velocity in the form of spatial velocity distribution (profile) over the pipe cross-section. By this, it will be possible to apply the Equation (1.1b) previously shown as all of its terms will be known.

1.2   OBJECTIVES

In order to achieve the study motivation goal, the work was divide in follow objectives:

a) Evaluate an effective way to estimate transit velocity:

By transit velocity is meant the velocity of the interfaces measured between the two planes of the DIS. Due to the intrinsic nature of the flow and the measuring process (sample rates, noise, etc.) is needed to investigate which of many techniques available are more suitable to this specific problem approach. Hence, 3 different algorithms will be implemented; cross-covariation, SAD (Sum of Absolute Differences), SSD (Sum of Squared Differences)

b) Implement spatial velocity profile and flow rate estimation algorithms:

Known properties of the DIS cross section sensitivity will be used to develop a spatial or 3D sensitivity matrix for the transit velocity. Since the previous objectives are successful,

their results on the phase interface's transit velocity and the phase fraction are concatenated, finally producing the velocity profile. As the profile is integrated along the pipe area over the time, flow rate is obtained.

c) Validation method :

To adjust the algorithms and validate the results, extensive tests with both synthetic and experimental data will be performed. The synthetic data, although with limitations in terms of not representing all the two-phase flow diversity, remains a valuable tool since it allows fast parameter changes in a more agile way than in pilot facilities, and provide a greater level of certainty about some parameters been analyzed. Therefore, the synthetic data is useful for hypotheses tests and calibration-like procedures. To generate the synthetic data, an algorithm that emulates the DIS raw data will be developed.

After adjustments and classification, the chosen algorithms will be applied to experimental data acquired from air-water flows obtained in the test facility at NUEM on UTFPR (Federal University of Technology), in 1 inch horizontal pipes with 40 meters long. As the facility has calibrated reference sensors for measuring air and water flow rates, the quality of proposed method can be validated.

1.3 THESIS OUTLINE

The text of this thesis was organized as follows:

Chapter 2 offers a literature review; Screening multiphase flow and its state-of-the-art measuring techniques, details of electrical tomography theory, next explores elements of transit velocity measurement and closes with DIS sensor detailing.

Chapter 3 presents the work methodology, *i.e*, materials and methods applied. Thereby, itemizing the steps for spatial velocity estimation, synthetic data generation, the algorithms involved and the description of NUEM's test apparatus used for experimental data acquisition.

Chapter 4 contains obtained results analysis and presents insights over the different procedures tested and show the final estimated flow rate.

Finally, chapter 5 portray the conclusions obtained from the results data analysis and give suggestions for future researches and works continuity.

2 LITERATURE REVIEW

The purpose of this chapter is to provide the readers with a foundation in the concepts and technologies related to the proposed problem and listed in the first chapter. Therefore, a review of concepts in multiphase flow and measurement techniques, electrical tomography, transit velocity, and the DIS will be presented.

2.1 MULTIPHASE FLOW FUNDAMENTALS

The development and interest in multiphase flow is strong related to technological development and the demands of the economic-industrial sector, but their origins are related to fundamentals concepts of fluid mechanics, thermodynamics and heat transfer such as, *e.g.*, density, and mass-energy transference (17) and it is a natural phenomenon as Figure 2.1 show.

Figure 2.1: Natural multiphase flow occurring in nature
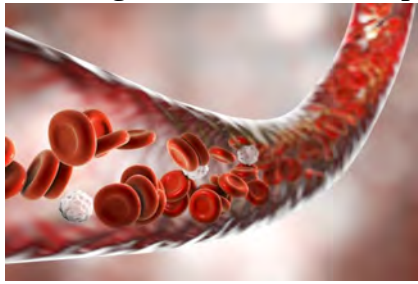
(a) Solid-liquid flow in bloodstream.
Source: Adapted from (18)
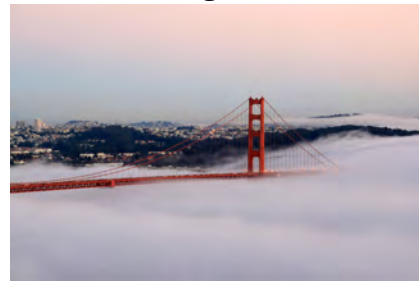
(b) Gas-liquid flow in fog moving with the wind.
Source: Adapted from (19)

(c) Gas-liquid-solid flow in a lava flow.
Source: Adapted from (20)

(d) Liq-liquid flow at rivers encountre.
Source: Adapted from (21)

The use of nuclear power for electricity generation in the 1940s is usually a reference for the beginning of field current development (22), due to extreme conditions of the flows in the various water-vapor circuits as illustrated in Figure 2.2.

Especially for the oil industry, the 1970s were significant due to increased demand and dependence on oil by the world economy (24), which produced an outbreak in the development of flow models. However, after the oil crisis in the 1980s, interest became stagnant. More recently, the Brazilian pre-salt production area and new paradigms of efficiency and concern for the environment have been encouraging new studies in the area.

Figure 2.2: Schematic diagram of a nuclear power plant using CANDU reactor type.
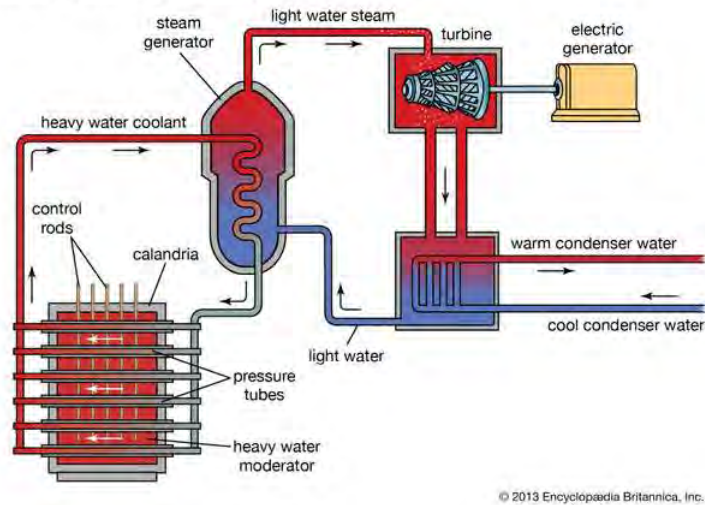
Source: Adapted from (23)

Figure 2.3: Actual oil production scenario representation.

(a) Brazils' Pre-salt production area. Source: Adapted from (25)

(b) Examples of offshore oil production systems. Source: Adapted from (26).
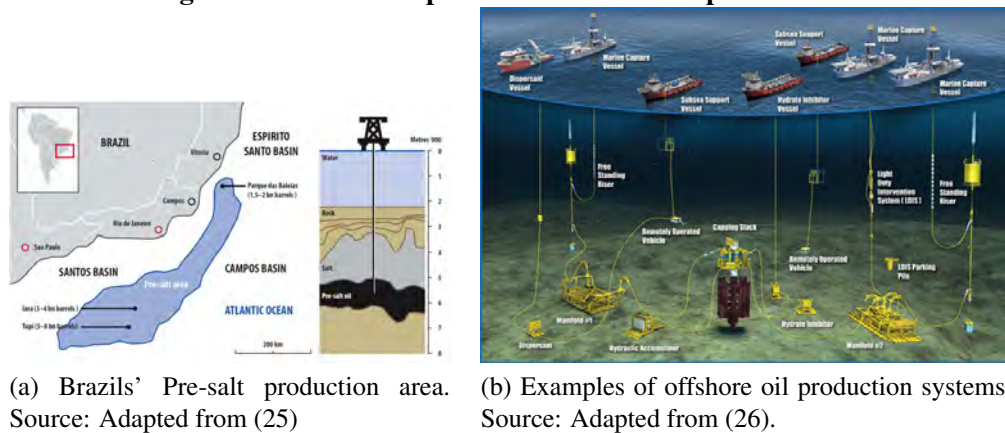
As mentioned before, multiphase flow is understood as the concurrent passage of a stream formed by two, or more, immiscible substances having different properties in restricted containers, such as ducts, pipes, vessels or reactors.Multiphase flows can be formed by substances in more than one physical state, *i.e.*, solid, liquid, gaseous, *e.g.*, steam-water flow, or different chemical substances (27), *e.g.*, air-water flow, in this case, the flow can also be named multi-component (1). Therefore, there must be a discontinuity between these substances or states which creates groups of physical properties called phases. (28). In this sense, one can state that the presence of boundaries, or interfaces, between phases as the main characteristic of these multiphase flows (29).

For this particular work, the two-phase case is of most interest. As cited by (30) the description of two-phase flow in pipes is complicated just by the essence of the interfaces.

Furthermore, the existence of a wide variety of interaction forms between these interfaces depending on, for example, the flow rates and physical properties of each phase, the pipe geometry and inclination, flow direction, environment and operating conditions its also an aggravation.

Since the gas-liquid flow is, in general, the most recurrent in the industry and it has a special interest in the petroleum exploration and transportation area, occurring in horizontal, vertical and inclined ducts, next follow a detailed description of its characteristics and flow patterns.

In particular, but not exclusively, in gas-liquid flows, both interfaces are, in principle, deformable and an extended number of interaction modes is possible. These interactions generate structures that are termed flow patterns or flow regimes. The classification of this flow pattern is usually done by the application of categorical data or based on air-water experiments, *i.e.*, empirical data. Thus, among the many patterns present in the literature, a select number of widely accepted are briefly described in the sequence for horizontal and vertical flow cases.

The horizontal flow regimes in restricted channels show a non-symmetrical pattern which is due to the effect of gravity on fluids with different densities. This generates a tendency of stratification in the vertical direction, which means that liquid flow tends to occupy the lower part of the vessel and force the gas phase to the upper parts. It is important to mention that the flow components, especially liquid, are also subject to other forces like surface tension, viscosity, and dynamically generated body forces (31). It is known that the interaction of these forces has a great influence on the formation of flow patterns, but the characterization of these interactions is beyond the scope of this section. For more detailed information, see the works such as (32–35).

For concurrent horizontal flows the most common regimes are listed next and shown in Figure 2.4. The list is organized from top to bottom, from the highest gas flow to the lowest one.

- Annular flow: This occurs when the gas flow is large enough to support a gas core with complete liquid film around the pipe walls. The effect of gravity forces in the liquid film to be thicker on the pipe bottom although this effect is diminished as the gas flow rate increase and eventually the film circumference becomes uniform.

- Slug flow: It is identified by the presence of elongated bubbles traveling at the top of the pipe with a diameter similar to the pipe, separated from each other by liquid slugs, which could develop large-amplitude waves, that may contain innumerable smaller bubbles entrained.

- Plug flow: Similar to the slug flow, but the bubble's diameters are relatively smaller and a continuous liquid film can be identified at the pipe bottom. Together with the slug flow, it may be classified as an intermittent flow class.

- Wavy flow: As the gas flow decreases, the phase separation becomes more clear. So, the liquid stays at the vessel bottom but wit distinguishable ripples caused by the gas flow.

- Stratified flow: Usually observed at relatively low flow rates of both gas and liquid. As the gravitational separation is completed, the liquid flows in the lower part of the pipe with gas over it in a smooth interface guide-mark. Although in real situations, ripples may appear eventually.

- Bubbly flow: Also refereed as disperse bubble flow, it occurs when a considerable low gas rate flows in a liquid continuum. Again, as a gravity effect, the bubbles tend to accumulate in the upper portion of the pipe.

- Bubbly flow: Also refereed as disperse bubble flow, it occurs when a considerable low gas rate flows in a liquid continuum. Again, as a gravity effect, the bubbles tend to accumulate in the upper portion of the pipe.

Figure 2.4: Two-phase flow patterns in horizontal flow.
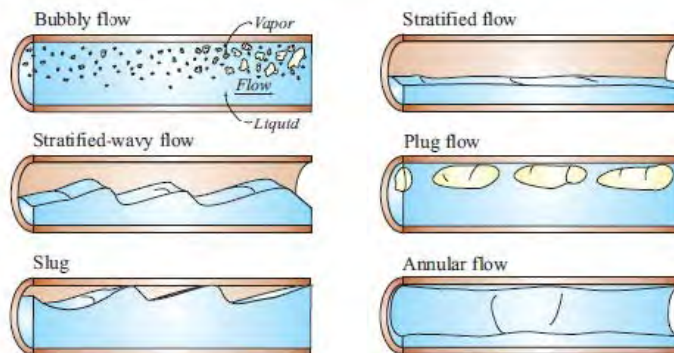
Source: Adapted from from (36)

In ascending vertical flow a variety of flow regimes are identified which have similarities to those seen in the horizontal case, unless the case of stratified flow. As the gravity effects are parallel to the direction of flow, the observed patterns tend to be more axis-symmetrical. The behavior of other flow characteristics, which depend on body forces tends to be the same as in the horizontal flow. Next, some most commonly observed two-phase flow in vertical circular cross-section channels are summarized, as before, from the highest gas flow rate to the lowest one.

- Annular flow: Relatively high gas flow rates with low liquid flow generate this regime in which both liquid and gas are continuous.

- Mist flow: In cases of very high gas flow rates or a high-density gas may cause some liquid flow to be entrained as droplets carried with the central continuous gas phase. This is called annular mist flow.

- Churn flow: With less gas rate to sustain the gas core, the liquid film collapses. As a result, distorted liquid slugs are created then break down into an unstable pattern with a characteristic liquid oscillatory motion.

- Slug flow: Usually occurs at higher elevations above the inlet to the vertical channel. One can observe a slug flow as a result of the bubbles' coalescence, producing a train of large (several times the pipe diameter) bubbles. Also, an increase in gas flow may cause this pattern at lower elevations.

- Plug flow: With even lower gas flow rate, the formation of Taylor's bubbles is noticed. Eventually, with the flow development, it may evolve to slug flow.

- Bubbly flow: It is characterized by a relatively small quantity of gas as in the form of a myriad of small bubbles that are mixed with a moderate flow rate of liquid.

Figure 2.5: Two-phase vertical upward flow regimes.
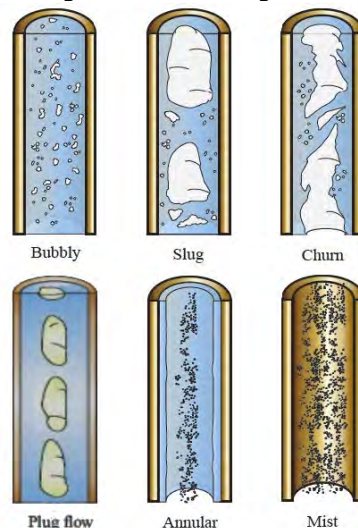
Source: Adapted from from (36).

One can notice that the previous descriptions are only qualitative. The determination of flow regimes classically depends on visual observations, which implies the use of transparent ducts and high-speed cameras, which is not always possible from a practical point of view.

Moreover, the patterns are the most frequently observed and accepted by the researchers. There are records in the literature of 84 different flow types (31). Furthermore, flow scenarios like counter-current flow, downward concurrent flow and inclined flow direction show its peculiarities. Even with a crescent but no larger yet research about this particular flows, more can be seen in the works (37–39).

Nevertheless, a designer needs a theoretical guideline or a reliable correlation to calculate the required conditions to establish a desired flow regime, or to analyze the state of a facility for illustration. In this sense, efforts to make theoretical and experimental studies for a quantitative description of the conditions that lead to a flow regime transition from one pattern to another need to be acknowledged.

For this, as is mentioned in numerous studies as pointed by (40) no single theory or correlation can satisfactorily predict the interactions over all possible flow regimes encountered in two-phase gas-liquid flow in pipes. Indeed, all the design variables are strongly dependent on the existing flow pattern (41). Consequently, the standard procedure used in several studies consists of the definition of parameters set which bring a direct and strong connection with the occurrence of flow regime transition. Usually, two main parameters are used for the definition of a coordinate system over which boundaries between flow patterns are drawn, resulting in what is called a flow regime map. Notwithstanding, it is necessary to understand that this procedure implies in maps that cover a limited range of fluid properties and pipe diameters yet in the presence of some discrepancies between the predicted and real flow especially in the proximity of the flow regime boundaries.

In these work context, the proposed maps by Backer (42), Taitel and Dukler (43), Taitel and Barnea (44) and Wiesman *et al.* (45) are significant since they establishes some mostly accepted references. For a deeper understanding of these particular subjects, the work of Corral (46) e Rouhani (31) present a deep comparative analysis of many regime flow maps.

In the listed works above, the use of a coordinate system defined by mass velocities of the phases or by the so-called superficial phase velocity (J_p), that if even simple (almost simplistic if compared to other proposes) is perhaps a reasonable discrimination criteria for identifying the operating conditions that produces several flow regimes for a given pipe diameter and wall surface nature (40), *e.g.*, pipe wall roughness and immiscibility. The flow pattern map produced by the superficial phase velocity approach is shown in Figure 2.6.

The Taitel and Dukler's map presented in (43), Figure 2.6a, is the most widely used flow pattern for horizontal gas-liquid flow, mostly because it is a result of a semi-theoretical method and the very satisfactory agreement of its results with the empirical ones provide by

Figure 2.6: Taitel's *et al.* proposed liquid-gas flow maps with superficial velocity for gas (VSG) and liquid (VSL) as coordinates.
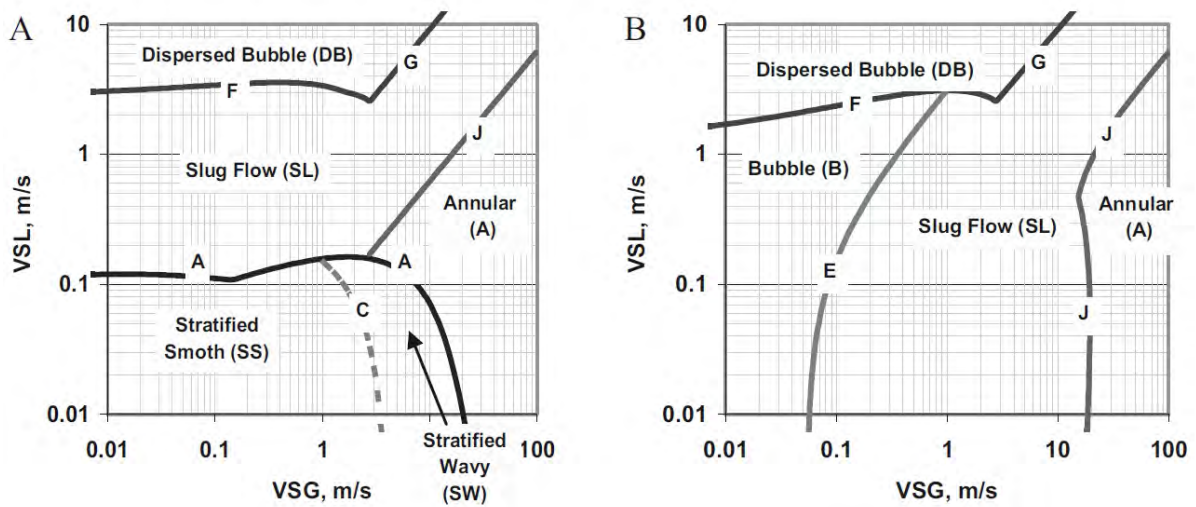
Where A is horizontal flow and B vertical flow, the letters over curves indicate transition conditions.
Source: Adapted from (41).

Mandhane (40). Later, in other work (44), a liquid-gas vertical flow map was proposed, Figure 2.6b, and it is possible to see the difference between flow patter transition conditions between horizontal and vertical cases

2.2 MEASUREMENT TECHNIQUES FOR MULTIPHASE FLOW

In the sequence, some multiphase flow metering techniques (MFPM) will be described. But at first, as given by (47) that there is no consensus in the notation and in the symbols used to describe the multiphase phenomena parameters. That may cause some understanding difficulties thus, key definitions of multiphase flow variables will be presented in advance, the other variables are described according to the need according to text development.

As anticipated in Equation (1.1b), the index p associated with one variable indicates the phase, *e.g.*, gas (G) or liquid (L). According to the equation context, the absence of the index may indicate a parameter relative to the mixture (all phases). These following definitions are based in (48–50).

- Volumetric flow rate, Q or q (m^3/s):

  The volumetric flow rate is defined by the volume of fluid which passes through cross-section per unit of time. For a given point in the flow or cross-section of a pipe, the volumetric flow of the mixture and phase p are represented respectively by q and q_p. Considering a flow in the absence of chemicals reactions, the total volume of the mixture is conserved such that for a two-phase gas-liquid flow the volumetric flow of the mixture

is the sum of individual phases volumetric flow, Equation (2.1).

$$q = q_G + q_L \qquad (2.1)$$

- Superficial Velocities, J_g and J_l or v_{sG} and v_{sL} (m/s)

  Also, represented as J_g and J_l, the superficial velocity of a phase represents the volumetric flow rate per unit area, as represented in Equation (2.2), where A is the pipe cross-section area.

$$J_l = \frac{q_L}{A} \qquad (2.2)$$

- Phase Fraction: Liquid Holdup (α_L) and Gas Void Fraction (α_G)

  Phase fractions in general, describe in space or time the ratio of one phase to the mixture. Hence, the phase volume fraction indicates the proportion of one phase volume to the total mixture volume, or the proportion of cross-section area occupied by one phase (51).

  The liquid holdup represents the fraction of a volume element in a two-phase flow field occupied by the liquid-phase, Equation (2.3). Similarly, the gas void fraction is the fraction of the volume element that is occupied by the gas-phase, eq.(2.4), (48).

$$\alpha_L = \frac{A_L}{A} \qquad (2.3)$$

$$\alpha_G = \frac{A_G}{A} \qquad (2.4)$$

Considering single-phase flows the values of α_L or α_G variates between 0 and 1. For two-phase flow, the closure condition presented by Equation (2.5) is imposed.

$$\alpha_L + \alpha_G = 1 \qquad (2.5)$$

This parameter is also called *mean phase content* by (52), which adds that there can be differences between the actual phase contents and those calculated from the volumetric phase flow rates due to different velocities of the phases.

For pipe flow studies, however, a more-useful definitions are required. The *instantaneous volume phase fraction*, that refers to a differential volume element and represents the phase fraction at a given time and space point in the flow field. Integration of the instantaneous volume phase fraction over time will yield the local liquid phase fraction at

a given location, as shown in Equations (2.6) and (2.7) for void fraction and liquid holdup respectively, according to (48).

$$\overline{\alpha_G} = \frac{\int \int \alpha_G(r,t)\, dr \quad dt}{\int dr \int dt} \qquad (2.6)$$

$$\overline{\alpha_L} = \frac{\int \int \alpha_L(r,t)\, dr \quad dt}{\int dr \int dt} \qquad (2.7)$$

Where $\alpha_G(r,t)$ and $\alpha_L(r,t)$ represent the instantaneous volume phase fraction for gas-phase and liquid-phase. More details may be found in lectures of (47, 49, 51).

- Actual Velocity, v (m/s)

The superficial velocities are not the actual velocities of the phases (48), as each phase occupies only a fraction of the pipe cross-section. Thus, the actual velocities of the liquid and gas phases are represented by Equations (2.8) and (2.9) respectively. In (47), it is also called the attention that this value represents an average of the phases velocity.

$$v_L = \frac{q_L}{A_L} = \frac{J_l}{\alpha_L} \qquad (2.8)$$

$$v_G = \frac{q_G}{A_G} = \frac{J_g}{\alpha_G} \qquad (2.9)$$

2.2.1   MULTIPHASE FLOW METERING PROBLEM

Following the presentation of fundamental concepts in multiphase flow, this section introduces the operational scenarios, advantages and limitations of multiphase flow metering. Thereby spelling out the problem of MPFM, centering in the oil industry. MPFM was first conceived for the non-intrusive metering of the simultaneous flow of two or more phases, without the need for phase separation.

The production from oil wells are rarely purely liquid or gaseous hydrocarbon mixtures. Most often, the fluid emerges as a multiphase mixture. In its simplest from, it is a mixture of natural gas and oil but, in many systems, water is present as are a variety of solid phases (sand, hydrates and asphaltenes) (1, 53). The base method used to meter the crude oil production consists in separation and treatment of the different phases them conventional single-phase flow instrumentation such as turbine meters, orifice plates, among others are used.

However, starting in the 1980's (1, 51), the economics of offshore oil recovery have moved towards sub-sea completions with multiphase pipelines over long distances to either

the shore or to existing platforms and to unmanned fields in remote onshore areas. The need for directly metering well stream production became acute. These challenges of MPFM must consequently be faced.

Multiphase flow metering has a series of complex problems that had to be solved. For exemplify, multiphase flows are intrinsically unstable, with several flow patterns, continuously fluctuating phase fractions, often differing velocities for the same phase and specif problems related to the oil composition (53). Thus, its requires stabilizing the flow to obtaing a steady velocity profile in the measurement section. Within the oil and gas industry, it is generally recognized that MPFM could lead to greater benefits in terms of (1): layout of production facilities, well testing, reservoir management, production allocation, production monitoring, subsea/downhole metering and costs when compared with construction of dedicated flow lines and separators (53).

Measurements performed by test separators have an uncertainty of between 7.5% and 10% (49), but require regular intervention by trained personnel and cannot provide continuous well monitoring. A further limitation of well testing with conventional separators is that wells suffer from shutdown cycles related to well testing. Hence, wells that are tested on a regular basis usually require more frequent work-overs to maintain their production rates. At the same time, advances in reservoir management and modeling have increased the need for frequent well tests to provide data (53). This can create technical problems which could impair test significance, such as severe slug flow.

In (1) two approaches are recommended to flow rate multiphase measures; the first with independent flow parameters (functions of the individual flow rates) are measured and relationships between them and the flow rates of the respective phases are established. The main problem of this approach is the need for calibration since the relationships can not be theoretically predicted, and it is known that calibration has an accuracy range limitation. So is not possible to calibrate with the same level of accuracy over full range operating conditions.

With the second approach, the basic parameters of phase velocities and phase fractions (or quantities that can be unequivocally related to these) are measured. The phase velocities and fractions are then combined to provide the phase flow rate. For an n-phase flow, n mean velocities and n-phase cross-sections are required. Thus, n velocities and (n-1)-phase fractions (the last fraction is obtained by difference between unity and the sum of the others measured fractions). The number of required measurements can be reduced by separation or homogenization since number of individual measurements, *e.g.*, 5 for three-phase flow, that may be difficult or impossible in some cases, particularly for different phase velocities (53).

Table 2.1 presents list of desirable characteristics for the MPFM in oil industry, according to (1),

Table 2.1: Desirable characteristics of MPFM.

Desirable characteristics
Repeatability
Accuracy
Wide range applicability
Ease of installation and intervention
Low-capital expenditure and operational costs
High mean time before failure (MTBF)
Official acceptance by the governments

Source: Reprinted from (1)

Even though the purpose of multiphase flow measurement is to determine the parameters of individual flow components, unfortunately, there is still not to the date a single instrument capable of measuring all individual n-phase parameters directly. Thus, it is necessary to combine several devices into one instrument package and to calculate specific phase flow rates from the combined readings.

2.2.2 KEY TECHNIQUES FOR MPFM

Since the fundamentals of multiphase flows and MPFM problem are stated, next some key meter techniques are described.

One way of classification for MPFM devices may be according to the parameter which they measure. According to (1), there are five basic parameters that can be measured by MPFM devices; density, velocity, momentum, mass flow and elemental analysis. Other classification should be based in the metering principle, *e.g.*, impedance, acoustic, optic or nuclear.

Though, it is a non-extensive review since it is not the objective of actual work and there are many studies in development. Hence, only metering methods related to variables pertinent to this study will be described next. Later, the ECT and cross-reference like methods for velocity estimation will be detailed in its own sections.

Phase fractions measurements are included in the density measurement category, according to the parameter classification proposed by (1), and examples of techniques and principles of they are:

- Acoustic Attenuation principle:

  The techniques based on this principle take advantage of the physic effect that sound waves are strongly altered in the presence of bubbles in liquids, in terms of wave speed

and attenuation (54). Thus, it may be possible to obtain information about phase fraction content by examining the transmission of sound through the mixture, using the variations in sound velocity in the two-phase mixture as a function of the gas content. The principle governor equation is represented in Equation (2.10), where $\frac{A}{A_0}$ represents the acoustic pressure attenuation with A_0 been the pressure amplitude in the absence of gas-phase, I is the sound intensity, I_0 is the incident sound intensity x is the distance traveled by the sound waves through the medium and μ an attenuation coefficient. Works as (55) and (56), illustrated in figures 2.7(a) and 2.7(b) are examples of implementations of these techniques.

Figure 2.7: Acoustic attenuation, apparatus and response.
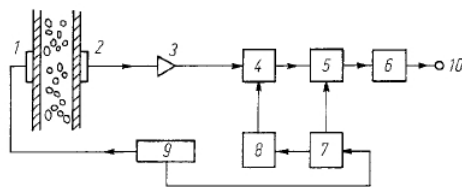
Data acquisition system: *1* Emitter, *2* Receiver, *3* Amplifier, *4* Peak detector, *5* Sample/hold circuit, *6* Low-pass filter, *7, 8* Monostables, *9* Wave generator, *10* Signal output

(a) Apparatus for acoustic atenuation experiment.
Source: Adapted from (55)
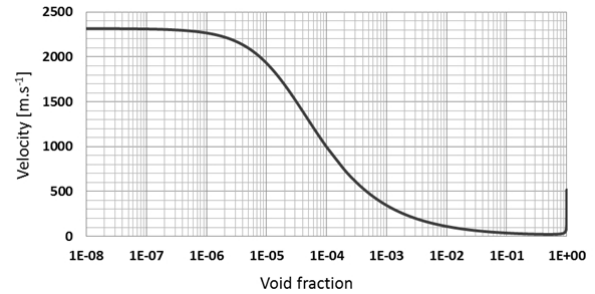
(b) Example of velocity attenuation response.
Source: Adapted from. (56)

$$\frac{I}{I_0} = \left(\frac{A}{A_0}\right)^2 = exp\left(-\mu x\right) \tag{2.10}$$

Acoustic attenuation represents a potentially powerful technique for diagnosing the characteristics of two-phase flows. Its predominately applied for bubbly two-phase flows, Studies In other flow patterns shown that the attenuation effect is much more complex (with macroscopic reflection from interfaces), but there are studies for other regimes as (57, 58) that examine slug pattern.

- Radiation attenuation principle:

It retains the same foundation as acoustic attenuation, but the radiation energy is stronger than the sound is. The intrinsic characteristics of radiation sources and their iteration with objects will define the particularities of the techniques that employ this principle. The most common configuration of radiation-attenuation-based techniques consists of a radioactive source (usually x-rays or gamma rays, but also neutrons), and a radiation detector located so that the beam passes through the container and is monitored on the other side of the two-phase mixture.

For a called chordal measurement, *i.e.*, that represents the attenuation of a collimated monoenergetic ray over an imaginary ray trajectory line, in a homogeneous medium, the radiaton attenuation follows the same exponential law in Equation (2.10), but the μ coefficient is adjusted for a radiation source.

By replacing the narrow beam with a linear source it is possible to do the measurement of the phase fraction in the complete cross-section, this is called single shot technique. However, for this configuration, the simple relationship given by Equation (2.10) is not generally valid because absorption depends on both the flow pattern and the pipe geometry, which poses major challenges for calibration. Another way to get this is by using a multi-beam densimeter device.

- Tomographic measurement technique:

A tomographic image is a two-dimensional representation of the cross-section of an object. Tomographic techniques are mostly known by its use in the medicine of diagnosis (59), and in fact, various viewing modes originally developed for medical diagnostics are now being adapted and refined for visualization of industrial processes. The use of tomography for the study of multiphase flows has been described in many review articles as (60, 61).

The general principle of computed tomography is to measure a physical property by a given number of integral independent measurements that are performed on the sensors (or electrodes), attached to the periphery of the object under investigation in different angular positions, either by rotation of the transceiver arrangements or by electronically switching electrodes, them reconstruct one image from these projections. In practice, before image reconstruction the signals from the sensor are treated by a signal acquisition and conditioning device.

The reconstruction of images on tomography implies the resolution of an inverse problem, that is, obtaining the spatial distribution of the visualized parameter from a set of measurements and the known geometry of the problem. The image reconstruction also implies in dealing with known non-linearities.

A conventional computer is often used for off-line image reconstruction. Real-time reconstructions are possible, but systems with parallel processing computational resources are required.

The tomographic technique may use various principles, as:

- Radiation Attenuation Tomography: X-ray, gamma-ray or neutron tomography can be seen as an evolution of the technique of radiation attenuation for void fraction

measurements in cross-sections as described previously in this section.

– Optical tomography: Optical tomography uses low energy electromagnetic radiation in the long-range infrared wave, visible or ultraviolet, to measure light attenuation characteristics by an object. It means that is safer than ionizing based methods. The Common feature of these systems is the use of low-cost light emitters and detectors (usually silicon integrated LEDs and photodetectors).

– Ultrasound tomography: The main difference over the acoustic attenuation technique is that on tomography ultrasound, several ultrasound transducers are mounted on the periphery of a pipe, which combined with appropriate image reconstruction techniques allows us to reconstruct an image of phase distribution. Basically, two modes of operation are possible, reflection and transmission. Image repetition rate in the order of hundreds of Hertz could be obtained. An advantage of the ultrasonic technique in relation to optical techniques is the possibility of measurement in opaque substances, however, the limitation is the impossibility of investigating flows with void fractions over 10% (62).

– Magnetic Resonant Imaging - MRI: MRI tomographs use the hydrogen core magnetic resonance phenomenon in conjunction with magnetic gradient and radio frequency pulses to map the object being investigated (63). Basically, MRI detects the concentration of hydrogen atoms, so liquid water has great contrast compared to other techniques. This principle of operation allows MRI not only determine core density, but also the velocity of the liquid in the case of flows.

However, there are some limitations to this technique, such as the need for non-conductive and non-magnetic piping, the low image repetition rate and the relatively high cost. A special MRI technique called echo-planar imaging (Echo-planar Imaging) can reach up to 140 fps and was used to investigate flows in gush. However, this technique requires an even higher hardware costs to achieve this repetition rate than conventional MRI.

• Impedance principle:

Liquid and gas phases present differences in its electrical properties, *e.g.*, electrical conductivity and, electrical relative permittivity. By applying electrodes to the perimeter of a pipe and by measuring the impedance through these electrodes, it is possible to determine the gas phase fraction of the pipe flow. As shown by (64) in their extensive review of analyzes on impedance techniques, there are several possibilities of geometric configuration of the electrode system to measure the gas phase fraction. Impedance

sensors offer high-frequency response, relatively low cost, and relatively low construction complexity.

For two-phase flows, the studies are concentrated in two kinds of impedance sensors, the conductive probes (sometimes also called resistive, since electrical conductance is the inverse of electrical resistance), and capacitive probes. Capacitive probes show advantages related to conductive probes when the liquid phase is an electrical insulator such as oil, for example, and offers the possibility of a totally non-intrusive void fraction measurement as the capacitive electrodes does not need to be in contact with the fluid. Conductive and capacitive measurement combinations have also been described in the literature, but this practice is less common.

In addition, good protection against parasitic capacitance and good signal to noise ratio are very important for phase fraction measurement. Complex impedance measurement has been described for three-component fraction measurements and for water measurements in oil-water mixtures.

- Wire Mesh Sensor:

Wire-mesh sensors are flow visualization devices that allow flow analysis with good spatial resolution and high temporal resolution. Although the technique does not belong to classical tomography techniques, because their principle of operation is based on intrusive electrodes. WMS is accepted as an alternative technique to the tomography systems described above. This type of sensor was initially proposed by (65) at the Dresden-Rossendorf Research Center (Forschungszentrum Dresden-Rossendorf - FZD). Since then this imaging modality has been continuously developed and has been widely used by researchers to investigate multiphase flow phenomena.

In the last decade, wire-mesh sensor electronics have been improved by (66) with the use of sinusoidal excitation signals that allow the measurement of fluid electrical permittivity (proportional to the capacitance of each intersection). With this, a much wider range of substances in a two-phase flow can be monitored, such as oil and gas.

- Contact probes technique:

Contact probes are a group of sensors that could be made based on many measurement principles. There are probes based on conductance, capacitance, temperature (hot wire) and optical that already been used for phase differentiation. Complete reviews can be found in (67, 68). However, the most common contact probes are electrical and optical ones.

In the case of optical probes, a beam of light is guided into the probe, usually through an optical fiber, to its tip. Depending on the phase present at the probes tip, light is transmitted in half or reflected. A photo detector at the other end of the fiber converts the reflected light intensity into a voltage signal. Light intensity is, therefore, an indicator of the phase.

Electrical probes use direct or alternating current excitation and the sensor acts primarily as a switch. When the phase at the probes tip is electrically conductive, an electric current passes from the internal electrode to an external electrode grounded. If the phase at the probes tip is non conductive the circuit is open and there is no current flowing. Normally the current value is transformed into a proportional voltage which is an indication of the phase present at the probes tip. Due to the signal reading and probe geometry influences, the measured voltage signal is usually converted to a binary signal across a voltage threshold (68). A probe based on the measurement of complex permittivity, *i.e.*, real and imaginary parts was described by (66).

For the velocity parameter is appropriate to mention the following techniques:

- Optical visualization technique:

  This technique is based on analysis and interpretation of flow images, that is, photographs or videos. To the date, high-speed cameras are easy to operate and typically reach up to 10,000 frames per second. In addition, through image processing algorithms, optical visualization techniques are useful for investigating the shape and behavior of bubbles as well as phase interfaces in liquid-gas flows. This technique has been widely described in the literature (69). The limitations of optical measurements are that only the pipe surface can be observed for high void fractions and both transparent walls and liquids are required for measurements.

- particle image velocimetry - PIV:

  Another classical optical measurement technique is the velocimetry by particle image velocimetry. It is used to measure the velocity of instantaneous flow. Images of small particles freely flowing in the liquid are made twice or more times by the pulsed actuation of a light source. The movement of these particles reflects the movement of the fluid and, consequently, the field of Integer vectors can be calculated. Recently, the PIV technique has been improved and applied with successful study of multiphase gas-liquid flows (70).

- Laser Doppler anemometry (LDA):

Another optical velocimetry technique that has been applied to two-phase flows is Laser Doppler anemometry (LDA) and derived techniques as (71), which produce localized values of liquid velocity. Measurements are generally fast, allowing measurement of speed fluctuations.

Hot film anemometry sensors have been applied to two-phase flows for flow velocity measurement since the 1960s (72). This technique is based on the cooling effect that a liquid flow has on an electrically heated wire. Wire resistance is proportional to this temperature and, based on heat transfer principles, heat flux relative to the surrounding fluid can be measured and thus the estimated liquid velocity. Recently 2 or 3 film sensors have been introduced to determine other velocity components (73).

2.3 ELECTRICAL TOMOGRAPHY

After reviewing the various techniques employed in multiphase measurement, this section returns to the topic of tomography techniques to further analyze the characteristics of ECT, which is the focus of the work presented.

Part of the process tomography techniques, ECT is in focus since the early 1990s as an alternative to traditional flow measurement techniques in order to avoid their disadvantage and comply with modern efficiency requirements as described in section 2.1. ECT may grant non-intrusive and non-invasive measurement with rapid visualization of the internal flow structure, hence, it has become a favored method to acquire cross-section images of non-conductive material flow in pipes, as ECT is sensitive to changes of the electrical permittivity distribution and can provide realistic data about the process state (74) even when the fluid involved is not characterized as electrically conductive without ionizing radiation involved and lost cost. Another central feature is that ECT is a soft-field technique, which means that the electromagnetic field does not follow a straight line, instead, its direction is dependent on the medium it traverses (14). The following description of a typical ECT system is based in the explanations provide in the works by (75–78).

The ECT system setup is usually composed of an array of several capacitance electrodes formed by simple metal plates. These electrodes could be placed inside or outside the vessel, depending on the wall material. If the sensing electrodes are mounted inside the pipe and are in contact with the medium but not disturbing the flow in any way, the ECT sensor is said to be non-intrusive. The traditional idea is to measure the changes in the electrical capacitance among all possible combinations of electrodes that occur when a dielectric material is introduced in the pipe.

As said, these inter-electrode capacitance changes are caused by variations in the

material permittivity inside the vessel. The electrodes are numbered from 1 to N, and the measurement protocol in the sensing electronics first measures the inter-electrode capacitance between electrodes one and two, then between one and three, and up to one and N. The measurements continue until all the inter-electrode capacitance is measured. The total number of measurements M is obtained by

$$M = \frac{N(N-1)}{2},$$
(2.11)

and the capacitance can be represented in a matrix, which is symmetric with respect to the diagonal due to $C_{i,j} = C_{j,i}$, with $C_{i,j}$ representing the inter-electrode capacitance between electrodes i and j.

$$\mathbf{g} = \begin{bmatrix} C_{1,2} & C_{1,3} & \cdots & C_{1,N-1} & C_{1,N} \\ C_{2,3} & C_{2,4} & \cdots & C_{2,N} \\ \vdots & \vdots \\ C_{N-2,N-1} & C_{N-2,N} \\ C_{N-1,N} \end{bmatrix}$$
(2.12)

From the measurement of these changes in capacitance, an image based on cross-section permittivity variation contents can be obtained by stating the capacitance variation as:

$$C_{i,j} = f(\varepsilon(x,y)).$$
(2.13)

The image reconstruction problem that emerges, consist in finding the inverse relationship where the permittivity distribution is estimated using the M capacitance measurements. This inverse relationship can be expressed as:

$$\mathbf{f_{or}} = \varepsilon(x,y) = f^{-1}(C_{1,2}, C_{1,3}, \cdots, C_{i,j}, \cdots, C_{N,N-1}),$$
(2.14)

where x,y are the cross section spatial coordinates and f_{or} represents the original image.

The process of image reconstruction will be further explained in section 2.3.2 of this chapter.

The capacitances values between electrodes are tiny, and sensitive measuring circuits are needed. While (76) says that capacitance values in an conventional ECT systems are in the range $0.1\,\mathrm{fF}$ to $500\,\mathrm{fF}$, more recent works like (77) state that these values are in the order of magnitude of attofarads $(\mathrm{aF}, \times 10^{-18})$.

The number and size of the capacitance electrodes used depends on the specific application. For example, a larger number of electrodes allows higher resolution images to

be obtained but the measurement sensitivity will be lowered compared with a sensor with fewer electrodes. The system sensitivity can be increased by using longer electrodes, but this will lower the axial resolution of the system.

The sensor design therefore, needs to be optimized for each particular application taking this trade-off in account. Figure 2.8 ilustrate one ECT system.

Figure 2.8: A basic ECT system overview.
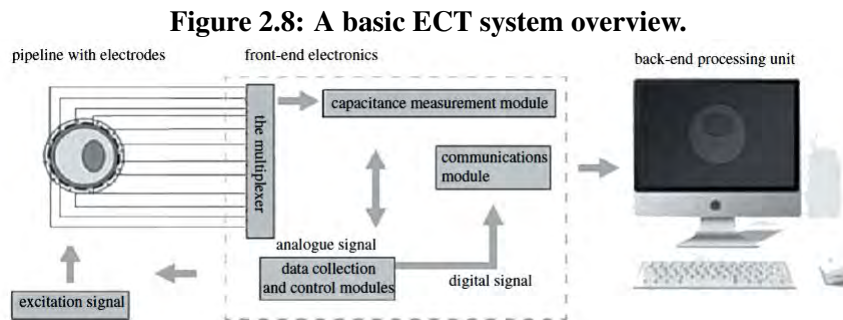
Source: Adapted from (77)

2.3.1 HARDWARE

The second step is related do the signal acquisition and conditioning. Usually, this is the middle-stage of the tomographic measurement process and is related as the hardware part. The data acquisition system is the portion responsible for control and register the measures of the capacitances between the electrodes in all possible combinations as explaned in last section. These signals are conditioned, them, they are sent to the image reconstruction software.

The most suitable measurement circuits for ECT are charge/discharge and ac-based circuits (79). The two circuits operate similarly, charging/discharging the measured capacitance continuously. The magnitude of the charge/discharge current is proportional to the measured capacitance. But, for practical purposes, the current need to be amplified. So usually by a current detector. The output of the current detector is connected to a low-pass filter to eliminate the noise that is created during charge and discharge.

Other aquisition system example is described in (66) for the WMS. The circuit is constituted by a direct digital synthesizer (DDS) circuit with selectable frequency in the range of 0.1–5 MHz, which is responsible for generating the excitation voltage. The excitation voltage is then time-multiplexed to each of the excitation electrodes by means of analog switches. In order to create a low impedance path, the outputs of the switches are buffered by operational amplifiers (op-amp).

A microcontroller controls the switches, program the DDS and controls the analog-to-digital conversion (ADC) timing. Each receiver electrode is connected to an AC current

amplifier (integrated into the OPA656 op-amp), which converts the current from the crossing points into voltages. The output voltage amplitude of the op-amp is proportional to the capacitance value of a crossing point (see section 2.1).To demodulate the sine wave signal to a proportional DC voltage, the ac current amplifier is connected to a logarithmic detector (AD8307, Analog Devices Inc.). The DC signals are then digitalized by a USB data acquisition card (Measuring Computing Inc., USB1616FS, 16-bit resolution, max. 10 kHz sampling rate per channel by simultaneous sampling of the 16 channels). Furthermore, the USB data acquisition card is connected to a computer, where the digitized data are processed and visualized.

2.3.2 IMAGE RECONSTRUCTION

The goal of image reconstruction is the recovery of an original image $\mathbf{f_{or}}$ from its observation, $\mathbf{g}$. However, the observations, or measurements, come with several limitations, *e.g*, polluted with noise, the relationship between the permittivity distribution and capacitance is non-linear and the electric field is distorted by the material presence, the soft-field effect. Also, the number of independent measurements is limited, what yield an under-determined problem, and the inverse problem is ill-posed and ill-conditioned making the solution sensitive to measurement deviations and noise (75).

The relationship between capacitance and permittivity is described by Equation (2.15)

$$C = \frac{Q}{V} = -\frac{1}{V} \int \int_{\Gamma} \varepsilon(x,y) \nabla \phi(x,y) d\Gamma, \tag{2.15}$$

where $\varepsilon(x,y)$ is the permittivity distribution in the sensing field, V represents the potential difference between two the electrodes forming the capacitance, $\phi(x,y)$ is the potential distribution, Q is the electric charge and Γ is the electrode surface.

In Equation (2.15), the potential distribution $\phi(x,y)$ also depends on the permittivity distribution $\varepsilon(x,y)$. Thus, the capacitance between electrode combinations can be considered as a function of permittivity distribution, as seen in Equation (2.16).

$$C = \xi(\varepsilon) \tag{2.16}$$

The change in capacitance in response to a perturbation of the permittivity distribution is given by

$$\Delta C = \frac{d\xi}{d\varepsilon} + O((\Delta \varepsilon)^2), \tag{2.17}$$

where $\frac{d\xi}{d\varepsilon}$ is the sensitivity of the capacitance versus permittivity distribution and $O((\Delta\varepsilon)^2)$ represents $(\Delta\varepsilon)^2$ and higher order terms. In ECT applications, $\Delta\varepsilon$ is usually small, thus by neglecting $O((\Delta\varepsilon)^2)$, Equation (2.17) can be simplified to the linear form.

$$\Delta C = s\Delta\varepsilon, \tag{2.18}$$

where $s = \frac{d\xi}{d\varepsilon}$ is the sensitivity of capacitance transducer to changes in permittivity. In this way, the non-linear problem is simplified to a linear approximation. This satisfies most applications with a small permittivity contrast or perturbation, according to (75).

Thus, taking image reconstruction as an algebraic problem, it can be written as a system of equations that represents an image degradation model that take the form:

$$g(x,y) = s * f_{or}(x,y) + b(x,y), \tag{2.19}$$

where $f_{or}(x,y)$ is the original image with size M X N, $g(x,y)$ is the measured image with degradation of the same size, s now is understood as a point spread function (PSD) and $b(x,y)$ is the addictive noise as before. The image coordinates are represented by (x,y) and $*$ denotes de convolution operator. Usually eq. (2.19) is write in matricidal form:

$$\mathbf{g} = \mathbf{S}\mathbf{f_{or}} + b, \tag{2.20}$$

where vector $\mathbf{g}$ represents measured signal, vector $\mathbf{f_{or}}$ the original image, b the noise and matrix $\mathbf{S}$ is the sensitivity matrix, that works as an observation operator approximating the blurring or convolution (80), and so, for an unknown vector $\mathbf{f_{or}}$ one can, ideally solve it by multiplying the observation operator inverse matrix with the measurement data to obtain an estimation image $\hat{\mathbf{f}}$ stating an inverse problem, *i.e.*:

$$\hat{\mathbf{f}} = \mathbf{S}^{-1}\mathbf{g}. \tag{2.21}$$

Unfortunately, in most of the cases $\mathbf{S}$ is not invertible; because it is not a square matrix or it is too large to compute, yet as mentioned by (80) , at the very least $\mathbf{S}$ is ill-conditioned, and in fact, recovery $\mathbf{f_{or}}$ is an ill-posed problem that (74) classify as intractable and (14) adds that even if possible the inverse approach would amplify the noise resulting in a very degraded image, since small noise can produce large alterations in estimation $\hat{\mathbf{f}}$, complement (81) and (82). Yet (14) call this approach as a naive way.

One intuitive option to solve the ill-posed problem is substitute the original ill-posed problem by other, well-posed. This substitution is done according the regularization theory which says that to remedy the ill-posedness of a problem, one needs to embed additional

knowledge in the problem formulation, in order to *regularize* it (83).

That may be done by replacing $\mathbf{S^{-1}}$ with S transpose version, $\mathbf{S^T}$ and to normalize the matrix S.

Currently a variety of methods have been proposed to treat the ill-posedness condition in ECT image reconstruction (74), and there are many possible classification criteria that could be applied. The variety of reconstruction methods or algorithms, and its evolution can be seen in various reviews over time, as for example, (84–86)

On the other hand, the class of algorithms used in ECT based on linear approximation theory can further be categorized in two groups: non-iteratice, or direct, and iterative methods. The role-played by chosen reconstruct method is critical to the final results (82, 87).

Non-iteractive algorithms are faster and hold the assumption that the sensitivity does not change as a function of the permittivity distribution. Iterative algorithms are slower with regard to the speed but usually have better performances.

Among iterative methods once can cite Landweber Iteration, the conjugate gradient method (CG), the algebraic reconstruction techniques (ART) (88), the simultaneous iterative reconstruction technique (SIRT) (89), the total variation (TV) regularization method (90) and others.

From those, the Back Projection and the Landweber Iteration method was chosen to be exploited in this work, since its capabilities are well-known.

a) Linear Back projection:

The Back Projection, shown in eq. 2.22 is the simplest reconstruction method used in Computerized Tomography (CT). The LBP is based mainly on the sensitivity matrix model and assume that sensitivity matrix is invariant. It is usual that the LBP generates blurred images. The cause of this blurry may be explained by the Fourier slice theorem, which shows how the tomographic setup of acquiring object projections is sampled in such a way that low frequencies are evaluated much more densely than higher frequencies. In image processing, the low frequencies take care of the smooth surfaces and the high frequencies take care of the details and the sharp edges, the result is that back projections' images appear unsharp (90). To solve this limitation variations as Filtered Back Projection (FBP) was developed. FBP is an analytic reconstruction algorithm designed to overcome the limitations of conventional LBP, *i.e*, comes to solve the blur problem. It applies a convolution filter to remove blurring at the same angles at which the projections are taken. The results obtained by the use of FBP are clearly better in terms of accuracy (more than

49% of difference) according to (91) in medical applications. On the other hand, as a non-iterative method it takes advantage of time resolution and can work in real-time state (82). It was, up until 1990s the primary method in cross-sectional image reconstruction and remains a very popular technique.

$$\hat{\mathbf{f}} = \mathbf{S}^{\mathbf{T}}\mathbf{g} \tag{2.22}$$

A variation of the LBP was proposed by (92) and called Iterated Normalized Back Projection (nBP). Normalized Back Projection method assumes that each back projected term is normalized and that normalization is both pixel and sensor projection dependent, as presented in Equation (2.23) where, subscript j is the pixel number, subscript i indicates the origin sensor of the projection, x represents the signal density, as named by the author, r stands for the length of intersection of the i-th sensor with the j-th pixel and y is measurement vector.

$$x_j = \sum_{i=1}^{I} \eta_{i,j} r_{i,j} y_i \tag{2.23}$$

Thus, the pixel density value is normalized according to its distance to each sensor and measurement value. Despite the name, the method can be implemented in a matrix form presented in Equation (2.24),

$$\mathbf{x} = \mathbf{N}^{\mathbf{T}}\mathbf{y} \tag{2.24}$$

with $\mathbf{x}$ as the reconstructed image, $\mathbf{N}^{\mathbf{T}}$ the normalization matrix.

b) Landweber Iteration Method - LIM:

The restrictions of LBP add with the advancement of computers power has cause the iterative algorithms to start replacing this method of image reconstruction. Works like (93) has show that iterative reconstruction methods improve image quality by qualitative and quantitative evaluation, and that they excel by its spatial resolution (82).

The main difficulty found in iterative methods is to determine the stop criteria (81), since after a certain number of iterations the image reconstruction quality starts to degrade instead of continuing to improve, this is called semi-convergence.

The LIM algorithm is an attempt to regularize the problem, and its one of the alternatives to Tikhonov regularization. LIM belongs to the steepest descent method and has been widely used in reconstruction problems on the ECT imaging.

A briefly,but complete, review of LIM approach is presented by (94), that within

describes the basic LIM algorithm, with k represents the iteration number and K is the maximum number of iterations, the stop criteria and μ; the step size, as the algorithm (1)shows.

$\hat{f}^0 = 0$;
for k=*1:1:K* **do**
 | $\hat{f}^k = \hat{f}^{k-1} - \mu H^T (H\hat{f}^{k-1} - g)$
end

Algorithm 1: Landweber Iteration Method algorithm

The LIM algorithm requires numerous iterations in order to obtain satisfactory results. The slow convergence is due to use of a bounded step-size constant to update the estimate image. The major drawbacks of the Landweber approach are issues linked to the step size μ. In order to ensure stability μ must satisfy the condition (2.25)

$$0 < \mu < \frac{2}{\sigma_{max}} \tag{2.25}$$

where σ_{max} is the largest eigenvalue of $\mathbf{H}^T\mathbf{H}$.

c) Adaptive Landweber Iteration algorithm:

Compute $\mathbf{H}^T\mathbf{H}$ is often difficult in practice. Many works as (94, 95) are dedicated to find a mechanism to update μ, that ensure stability without pre-computing σ_{max}, when μ satisfies eq. (2.25).

The step size μ has an interesting influence into the convergence speed of the Landweber algorithm, It is well-known the fact that when μ is increased the convergence speed increases. Continuing to increase the step size above a certain point, the convergence speed starts to decrease. This is a notorious phenomenon and the optimal step-size that ensures the fastest convergence is given by:

$$\mu_{opt} = \frac{2}{\sigma_{max} + \sigma_{min}}. \tag{2.26}$$

In practice as $\sigma_{max} \gg \sigma_{min}$ the optimum step size can be approximate as $\frac{2}{\sigma_{max}}$, which coincides with the upper bound. In (95) is proposed a time varying step size algorithm when the step size equals to the ratio between the L_2 norm of the first derivative of the estimated image at two consecutive iterations. The idea is that at early stages of the adaptation this ratio is large since the restoration effect is high and changes in the estimated image are significant. As the algorithm converges toward the optimum, the changes in the estimated image start to stabilize and the ratio of the norm converge to unity.

Later (94) implemented a variation in which three different steps sizes are computed at

each iteration for three different cost functions (mean squared error between the measured and the iteration estimation). The algorithm selects the estimate that produces the smallest coast function.

2.4 DIRECT IMAGE SENSOR

The DIS initially proposed by (28), was developed considering the needs of industry an academy, i.e., monitor and visualize phase distribution, understanding phase distribution physical phenomena and refinement of flow models.

The DIS was planned to combine advantages and avoid drawbacks of other techniques. In this sense, it combines the non-intrusiveness of tomographic systems with the high spatial and temporal resolution from WMS avoiding limited time resolution due the rotating mechanical parts in tomographic and the intrusive characteristic of WMS. Nevertheless, the fact that the DIS presents a lower sensitivity in its center must be taken in account(14).

Yet, by using the principles of electrical permittivity difference between fluids to evaluate phase distribution, the DIS is able to work with non-conductive fluids such as oil or organic liquids which are very common in the industry.

In the sequence is presented a brief description of the technical characteristics and functioning of the DIS as presented in (16, 28), the consultation to these works for more details on the technical characteristics, FEM simulations, determination of electrodes quantity and the confection process is recommended to the reader.

Sensor's basic structure is compounded by two emitter rings and a central receiver ring. In this work, the receiver ring is divided in eight electrodes equally distributed in the internal pipe wall in a way that enables capacitance measurements. Kapton tape is used as base material to the sensor fabrication, and a thin cooper sheet is applied over it. The materials are processed in a standard lithographic PCB (Printed-Circuit Board) fabrication process to form the electrodes. Thereby producing what can be termed as a FPCB (Flexible Printed-Circuit Board), Figure 2.9 shows the FPCB design with electrode dimensions.

The guard electrodes are used to confine the electrical field in the sensing region avoiding external interference. The installation of an extra electric shielding electrode on the external part of pipeline is another measure adopted to avoid interference originating from external sources to the measurement system when mounting the sensor inside the pipeline. Figure 2.10 shows the guard electrodes G, the emitter E and the receivers R.

The pipe must be punctured in order to electrical connections with the internal electrodes be made. This interface connection between the sensor and the measuring system

Figure 2.9: Direct Image Sensor.
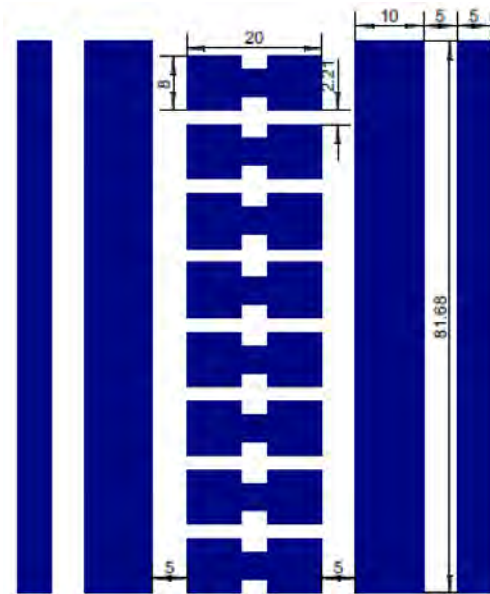
(a) DIS flexible PCB project.
Source: Adapted from (28)
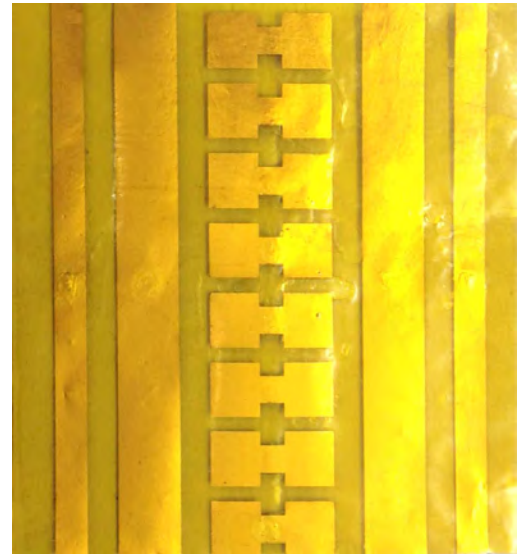
(b) Actual flexible PCB before insertion.
Source: Adapted from (28).

Figure 2.10: DIS - Simulated inside tube placement.
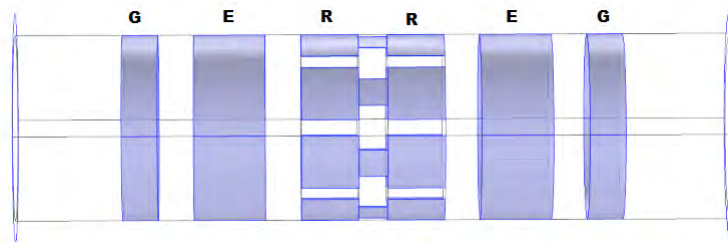
Source: Adapted from (14)

uses coaxial cables welded to the sensor electrodes and a standard DB-26 connector on the measuring system side. The DIS measuring system is based on the wire-mesh electronics (28, 29, 66). A schematic representation of the WMS measuring system in contrast with the DIS is shown in Figure 2.11. One can note in Figure 2.11(b) the two emitter electrodes corresponding to the upward and downward sides and the central array of 8 receive electrodes. In this arrangement, switching the source between the upstream and downstream emitter electrodes causes each DIS emitter-receiver pair to act as an individual sensor for upstream and downstream sides.

One input electrical (displacement) current flowing from the emitter to each receiver is converted into a proportional AC voltage level by the eight trans impedance amplifiers. These sinusoidal signals are converted into DC voltages (demodulated) by means of eight logarithm detectors. The signals are digitized by a DAQ (Data Acquisition System) and processed by a

Figure 2.11: Comparison of WMS and DIS acquisition systems.

(a) WMS like circutry.
Source: Adapted from (66)

(b) DIS Circutry.
Source: Adapted from (28)
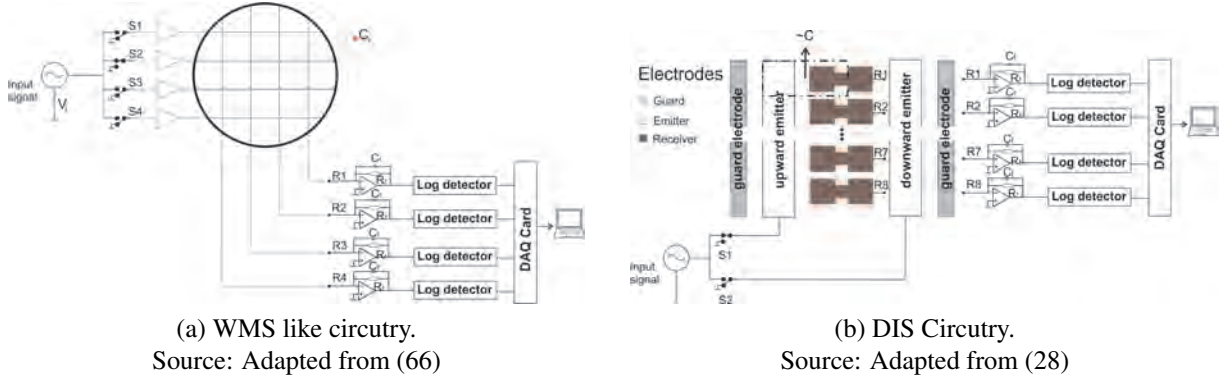
computer.

The acquisition rate of the system is up to 900 fps (limited by current DAQ used). The circuit shown in the block diagram of the Figure (2.11b) has a response of each trans impedance amplifier calculated by:

$$V_o = -V_i \left(\frac{j\omega C R_f}{1 + j\omega C_f R_f} \right), \tag{2.27}$$

where C_f and R_f are the capacitance and resistance of the feedback circuit at frequency f and where $\omega = 2\pi f$ is the angular frequency of the excitation voltage. If the circuit calibration is executed aiming to choose a frequency that cancel the conductive part of the circuit, $i.e$, $(\omega R_f C_f) \gg 1$ the output V_o of the circuit can be rephrased as:

$$V_o = -V_i \left(\frac{C}{C_f} \right). \tag{2.28}$$

Which implies that the output voltage of the Operational Amplifier is directly proportional to the capacitance between electrodes. Nevertheless, eq. 2.28 is a good approximation eq. 2.27 may also be used if more accurate capacitance values are needed.

Next, the Operational Amplifier voltage output, feeds the log-detector (AD8307). It is observed that the smallest changes in the capacitance C, and thereafter, in the voltage output V_0 can be measured maintaining a fast response time. Eq. sows the log-detector response form:

$$V_{log} = -V_a ln \left(\frac{V_0}{V_b} \right), \tag{2.29}$$

where $V_a = 0.2171$ and $V_b = 18.3864 \times 10^{-6}$ are AD8307 integrated circuit constants that are experimentally determined according to (66).

Figure 2.12: The way DIS perceives the phase distribution.
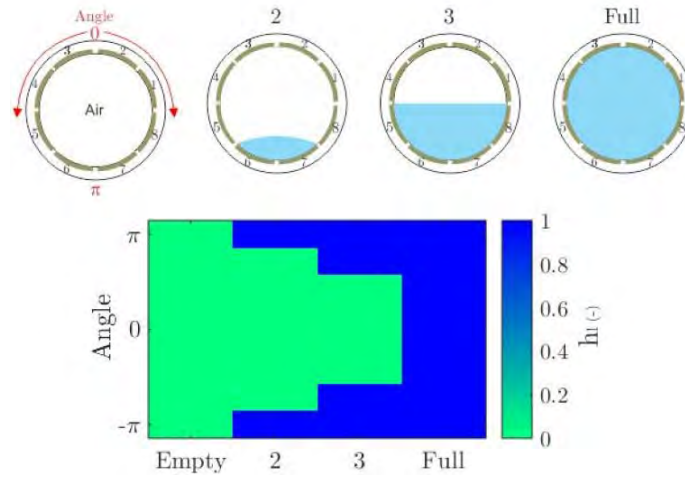
Source: Adapted from (28)

Combining eq. 2.28 and eq. 2.29 one can find the emitter-receiver par response in the form:

$$V_{log} = a\,ln\,(\varepsilon_r) + b, \tag{2.30}$$

where a and b are constants that involves V_a, V_b, κ_g, R_f and C_f. So the digitized signals by the DAQ are directly proportional to the relative electrical permittivity of the fluid between the emitter-receiver electrodes pair.

It is need to perform a calibration routine to correctly determine a and b for each sensor transmitter-receiver pairs. Once these parameters are obtained, it possible to describe de fluid permittivity by means of equation. , as follows:

$$\varepsilon_r(j,k) = exp\left(\frac{V_{log}(j,k) - b(j)}{a(j)}\right), \tag{2.31}$$

whit j and k standing for the receiver index and the frame number respectively.

Wrasse (16) give three cross-sectional views as examples of DIS output for gas-liquid mixture and one for a pipe full of liquid. In this example of DIS output, Y-axis represents the angle of the sensor at the pipe perimeter, *i.e.*, as the observer is looking the pipe from above, $\pm\pi$ is the horizontal center of the pipe and 0 the top. X-axis represents the filling steps shown. The liquid holdup content h_l is represented by image color scale, whereby the green color is the null h_l, which means only gas, and the blue color the maximum h_l, meaning only liquid present.

Hence, Figure 2.12 shows theoretical direct images for the given situations. Wrasse also provide a formula for the liquid holdup h_l quantitative estimation, as shown in eq. (2.32). However, before applying this equation, one needs to normalize the measured data so that ε_r^m.

Values are scaled between 0 and 1 representing the liquid holdup h_l, j and k represents the receivers and frame number respectively:

$$h_l(j,k) = \frac{\varepsilon_r^m(j,k) - \varepsilon_r^L(j)}{\varepsilon_r^H(j) - \varepsilon_r^L(j)}. \tag{2.32}$$

As the purpose of this work, aim not the liquid holdup but the void fraction (α), thereat and considering that the relation between liquid holdup and void fraction can be expressed as:

$$\alpha + h_l = 1, \tag{2.33}$$

the DIS outputs will be considered as shown in the sequence,

$$\alpha(j,k) = 1 - h_l(j,k). \tag{2.34}$$

Still, other models like Maxwell-Garnet and series model can be used to relate permittivity and phase distribution (16).

2.5   FLUID VELOCITY ESTIMATION

Usually the *transit velocity* [1] determination depends on two factors, the distance between two sensor points (in this work identified as upstream and downstream) and the time delay that the signal has between these points, represented in Figure 2.13. Since the distance is a known parameter, the main question is about the estimation of the time delay or lag.

These techniques for time delay estimation are most based in some form of similarity measurement between the upstream and downstream signals. This approach has been extensively studied, and a number of different methods and implementations have been reported in the literature in many fields. However, this approach implies that the process been studied need to presents some form of variation in time (turbulence), otherwise there will not be a characteristic signal reference to be compared between the two signals to generate the time delay estimation. Also, is important to observe that noise level, or signal degradation can reduce de accuracy of the estimation.To the flow rate measurement proposed, an accurate estimation of the time delay is a key factor that may determines the performance of the flow rate measurement(97).

To evaluate what different time delay method has to offers as trade-off between accuracy, spatial resolution, and computational efficiency, the methods of cross-covariance,

---

[1]In these work this term is used as reference to the velocity between two points along the axial direction of the flow.

Figure 2.13: Time delay between sensors.
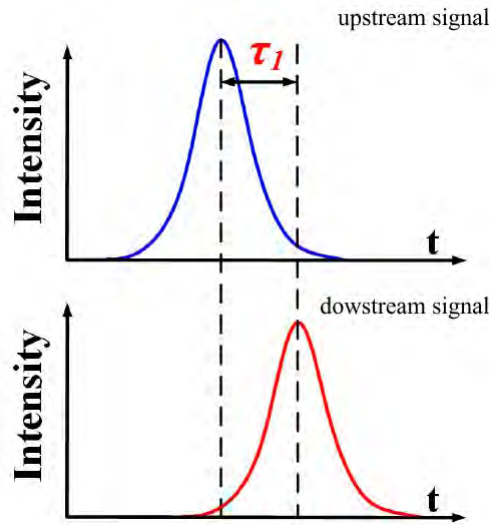
sum of absolute differences and sum of squared differences was chosen for inspection. The general way of calculating the transit velocity is presented and in the sequence particularities of the methods inspected are discussed.

The common principle is to apply a pattern matching function, which usually includes correlation coefficient and squared difference. The length of the sampling window and window overlap determines the axial resolution, which can be improved with decreasing window length or increasing window overlap (97).

The generalized discrete cross-correlation function is the base method for this approach. When applied to upstream and downstream signals it yields:

$$C_{u,d}(n) = \sum_{m=0}^{N} u[n]d[m+n], \tag{2.35}$$

where $C_{u,d}(n)$ represents the **correlation magnitude** at instant n between the reference upstream signal $u[n]$ and the delayed downstream signal $d[m+n]$, N as the sampling window size. The nature of the signals been correlated depends on the system properties, *e.g.*, for ECT systems the signals been analyzed are the medium permittivity variation.

As mentioned by Fuchs (15), this method may works better when the input signals can be considered white noise, since the white noise constant power spectral density should favor the peak detection. Also (15), suggest that the sensor can act as a low-pass filter, due to its intrinsic characteristics. In this case, a pre-whitening filter can be applied to yield sharper peaks

Figure 2.14: Example of Cross correlation function.
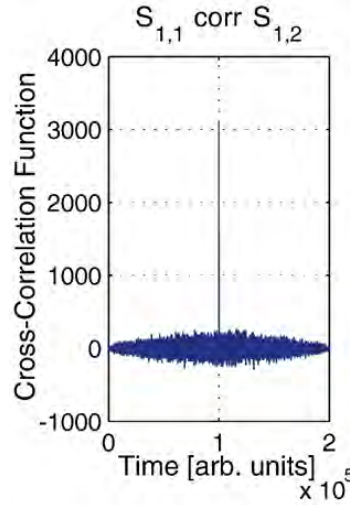
Source: Adapted from (15).

in the cross-correlation function, which leads the Equation 2.35 to:

$$C_{u,d}(n) = \sum_{m=0}^{N} u[n]d[m+n]WF[n],$$
(2.36)

where WF is the pre-whitening filter. This point is relevant because the peak location uncertainty refers to the smallest determinable flow velocity scale, and therefore the standard deviation of the time delay imposes important limitation to the measurements (98).

The obtained vector $C_{u,d}(n)$ is then scrutinized for the instant of peak covariance which when multiplied by the sampling time (t_s), yields the signal time delay between the upstream and downstream sensors, as show in eq. (2.37) provide by (99).

$$t_{u,d} = \underset{n}{\mathrm{argmax}}(C_{u,d}(n))t_s.$$
(2.37)

Thus, knowing the time delay and the sensors distance $d_{sensors}$ one can apply basic physic, *i.e.*, the velocity equation shown in Equation (2.38) to estimate signal velocity sensed amid the sensors.

$$\mathsf{v}_{u,d} = \frac{d_{sensors}}{t_{u,d}}$$
(2.38)

Many discussions can be found about cross-correlation and cross-covariance functions. According to (99), a cross-covariance function can be defined as shown in eq. (2.39).

$$C_{u,d}(n) = \sum_{m=0}^{N} u[m - \overline{u}]d[m + n - \overline{d}]. \tag{2.39}$$

If compared to Equation (2.36), one can easily identify that the difference is that the cross-covariance has the arithmetic means $\overline{u}$ and $\overline{d}$ removed from its respective signal.

The practical issue with cross-correlation as presented is that it will not exist (or be infinite) if the signals been analyzed have non-zero mean. So, in order to do the calculation, one really should subtract the mean beforehand. Yet, if the analysis is performed with finite length signals, the results end up with an underlying triangular offset as per the fig 2.15. Thus, knowing in advance that the data to be studied with the DIS have non-zero mean the choice of the cross covariance function is natural.

Figure 2.15: Triangular offset for non-zero mean signal over same function with mean subtracted.
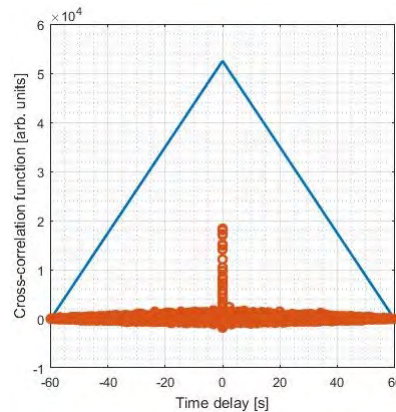
Source: Personal collection.

Sum of Absolute Differences (SAD) and Sum of Squared Differences (SSD) are functions widely used in the image processing area for pattern recognition. In this contest, a tracking procedure is done specifying a target, or reference. Then, an image-registration algorithm searches for the target in each sub-sequence image obtained. Thus, the image-registration algorithm finds the centroid of the target in the current frame by registering the target reference image with the current frame (100). From the view point of mathematics, SAD and SSD are algorithms where the displacement is found out by measuring the delay that minimizes L_2 (Euclidean distance) and a L_1 (Taxicab or Manhattan norm) respectively between the upstream and downstream signals (101).

In practice, the reference signal is aligned with each pixel int the current searched frame and subtracted from them. As explained by Raol in (100), this process yields a SAD signal, in which each pixel contains the SAD value. Pursuant to, the SAD value will be minimum at the position where similarity is maximum.

In the scope of this work, the upstream signal of each receiver is used as the target sample, to which will be compared with circular-shifted downstream signals versions, as showed in eq. (2.40)

$$SAD_{u,d}[m] = \sum_{n=0}^{P-1} |d(n) - u(n+m)|,$$ (2.40)

$$SSD_{u,d}[m] = \sum_{n=0}^{P-1} [d(n) - u(n+m)]^2,$$ (2.41)

where P is the number of samples m the shift count.

Thereby, counting the numbers of shifts to the minimum value one can find the time delay. What can be done by adapting Equation (2.37), as follows:

$$t_{u,d} = \underset{n}{\operatorname{argmin}}(SAD_{u,d}(n))t_s.$$ (2.42)

$$t_{u,d} = \underset{n}{\operatorname{argmin}}(SSD_{u,d}(n))t_s.$$ (2.43)

Thus, as SAD or SSD delay time is found by means of Equations (2.42) — (2.43) and one can apply Equation (2.38) normally in order to find the transit velocity.

It is expected that the transit velocity results obtained by SAD be more robust to the presence of outliers values in the measurements, while the results obtained by SSD be more sensitive to small variations.

2.6   VELOCITY PROFILE

By velocity profile, it is describing the distribution of velocities over the pipe cross-section. The idea of the velocity profile for multiphase flows is unusual outside the PIV field.

The velocity estimation techniques tend to work with time series, so it could be said that the flow is understood as homogeneous, that is, there is no spatial distribution of velocity. Therefore, references for it are limited. In (15), is proposed a way to exploit correlation function intensity values to obtain spatial resolution in a CT-like approach, that is presented in Equation (2.44),

$$v_K = \sum_{i=1}^{E} \sum_{j=1}^{E} W_{K,i/j} \cdot v_{i/j},$$ (2.44)

where v_K is the spatial velocity distribution, with K representing a specific area of the cross-section, E is the number of electrodes per layer, $W_{K,i/j}$ represents the back projection weights for area K with respect to the velocities determined between electrodes i and j, from the upward and downward layer respectively and $v_{i/j}$ is the axial velocities estimated between sensors i and j. As a first approximation, the weights may be assigned according to the sensitivity:

$$W_{K,i/j} = \frac{\frac{\partial S_{i,u}}{\partial \varepsilon_K} \cdot \frac{\partial S_{i,d}}{\partial \varepsilon_K}}{\sum_{j=1}^{N} \sum_{i=1}^{N} \frac{\partial S_{i,u}}{\partial \varepsilon_K} \cdot \frac{\partial S_{i,d}}{\partial \varepsilon_K}} \quad (2.45)$$

Where $S_{i,u}$ and $S_{j,d}$ stands for the sensitivity on upward sensor i and in downward sensor j respectively. This method generate a cross-section segmentation in K areas as shown in Figure 2.16, where the numbered bars represents the sensors position.

However, (15) adverts that, the velocity sensitivity determined by the cross-correlation function is not a linear combination of the element velocities, but rather affected by the region with high sensitivity, while regions with low sensitivity are suppressed.

Figure 2.16: Pipe cross-section segmentation.
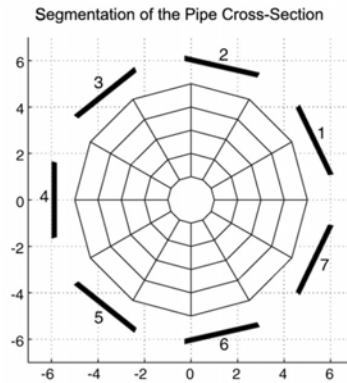
Source: Adapted from (15)

3 MATERIALS AND METHODS

> This chapter describes the procedures taken in the development of the study. Thus, implementation of the algorithms evaluated in chapter 2 are shown, the experimental apparatus and facilities are described. Also, workflow and strategies are outlined.

The steps adopted to evaluate the technique proposed in this work were based on works such as (15, 75, 102), in which questions about ECT velocimetry, image reconstruction algorithm evaluation, and synthetic data were discussed. Therefore, the first step taken was the generation of synthetic data emulating the DIS. These data were used to experiment and adjust the algorithms. After this, experimental data acquisition in NUEM's workbench was realized and the adjusted algorithms were tested and its results compared with the workbench instrumentation data. The next sections detail these steps.

3.1   SYNTHETIC DATA GENERATION

Synthetic data were generated by means of Matlab scripts which creates a simplified flow as a series of rectangular prismatic gas pockets (bubbles). One can control the cross-sectional size of these bubbles, as well the bubble length, the liquid body length and, of course, the axial velocity of the bubble. In this way generating what is called a unitary cell. Adding several unitary cells to the same simulation, changing bubbles sizes and velocities permit reproducing different flow patterns.

The upstream readings are obtained by adding noise to the synthetic flow data, simulating the measurement process. The downstream reading is obtained shifting the synthetic data in time, according to the sensor distance and flow axial velocity. Also, noise is added again to reproduce the flow chaotic variability.

The main disadvantage of this method is the fact that the synthetic flow is not able to replicate the intrinsic stochastic characteristics of actual two-phase flow, *i.e.*, the flow produced is predictable, with a strong periodic property.

On the other hand, since the objective proposed is not the faithful simulation of a flow, but rather, only to generate trustworthy flow data to evaluate reconstruction and estimation method proposed. In this sense, the predictability, in fact, comes in handy. Even the prismatic characteristics of the synthetic bubbles can be used to qualitatively measure the blurring degree levels in the reconstruction process and its effect in flow estimation.

Simulations were planned to represent slug flow, stratified flow, wavy stratified flow, bubbly flow, and also an "unnatural" horizontal flow with three bubbles of different sizes and velocities as shown in Figure 3.1.

Figure 3.1, provides the synthetic flows cross-section view with the bubbles'

Figure 3.1: Synthetic flow patterns cross-section view

(a) Slug flow

(b) Stratified flow

(c) Annular flow

(d) Bubbly flow

(e) Unnatural flow
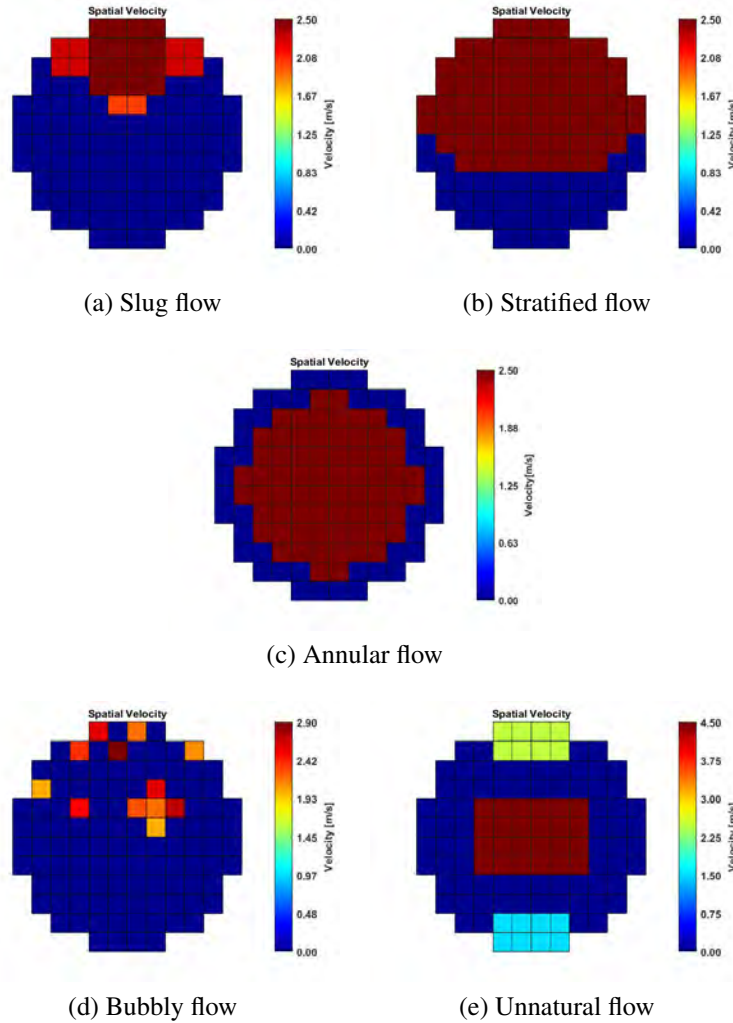
Source: Personal collection.

representation with their velocities. Table 3.1 presents basic quantitative data about these synthetic flows.

3.2 AXIAL VELOCITY ESTIMATION

This step is a straight application of the discussed algorithms in section 2.4, *i.e.*, Cross-covariance, Sum of Absolute Differences and Sum of Squared Differences. By considering the DIS emitter rings and its receiver electrodes as individual sensors, the gas-liquid interface can be identified by passing through the first ring, hereinafter referred to as "upstream sensor", u, and the second ring, referred to as "downstream sensor", d. Thus, we have in fact eight upstream signals and eight downstream.

It was chosen to do acquisitions with 60 seconds long and 900 fps. The initial assumption for that duration in acquisition was to avoid the common flow instabilities and variations effects, *i.e.*, thus seeking to stabilize the measurement as recommended in section

Table 3.1: Synthetic data flow info

	V_g m/s	α	Qg m^3/s
Slug	2.85	0.1866	1.4288E-04
Stratified	2.50	0.5714	4.0450E-03
Wavy stratified	2.50	0.4838	1.3384E-02
Annular	2.50	0.6072	5.5420E-02
Bubbly	2.35	0.0057	2.9717E-06
Unnatural	3.50	0.1795	3.3368E-04

Source: Personal collection.

2.2.1. Hence, each electrode produced a signal in the form of a data vector with 53940 samples.

As illustration, the resulting signals for individual correlation pairs can be seen for synthetic data in Figure 3.2a and 3.2b, and for experimental data in Figure 3.2c and 3.2d.

Figure 3.2: Correlation signals for Synthetic and experimental data
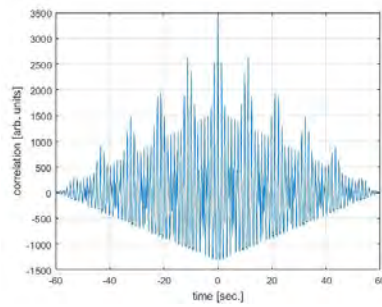
(a) Synthetic Data Slug Flow, eletrodes Up1-Down1
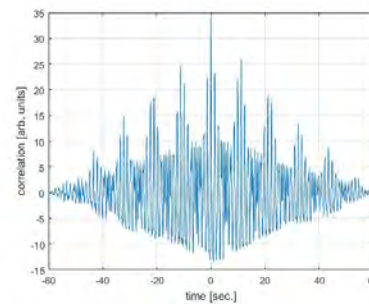
(b) Synthetic Data Slug Flow, eletrodes Up1-Down5
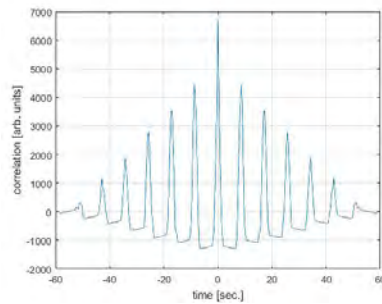
(c) experimental data Slug Flow, eletrodes Up1-Down1
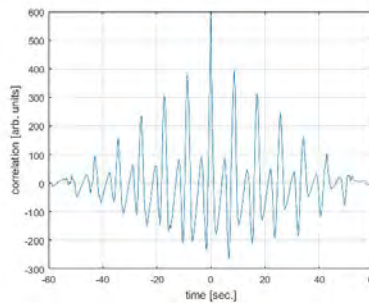
(d) experimental data Slug Flow, eletrodes Up1-Down5

Source: Personal collection.

Therefore, after correlating all upstream signals with all downstream, then searching for the delay in each correlation according to Equations (2.33), (2.38) — (2.39) and finally estimating the velocities by Equation (2.38) the results were organized in the form of a called axial velocity matrix, V as shown in Equation (3.1),

$$V = \begin{bmatrix} v_{1,1} & v_{1,2} & v_{1,3} & \cdots & v_{1,8} \\ v_{2,1} & v_{2,2} & v_{2,3} & \cdots & v_{2,8} \\ v_{3,1} & v_{3,2} & v_{3,3} & \cdots & v_{3,8} \\ \vdots & \vdots & \vdots & \ddots & \vdots \\ v_{8,1} & v_{8,2} & v_{8,3} & \cdots & v_{8,8} \end{bmatrix}, \qquad (3.1)$$

where the matrix elements has the form $v_{u,d}$, in a manner that, *e.g.*, element $v_{1,2}$ represents the velocity estimated between upstream electrode 1 and downstream electrode 2. This procedure was executed for the cross-covariance, SAD and SSD algorithms in each measurement condition, *i.e.*, flow pattern in the synthetic data and J_l — J_g setup for the experimental data, in order to evaluate computation time and the accuracy of the algorithm velocity estimation.

3.3   VELOCITY PROFILING OVER PIPE CROSS-SECTION

The sensitivity matrix or the blurring matrix is a key point in the image reconstruction process. The accuracy, noise robustness and overall final quality of the reconstruction algorithm relay much on its ability to correctly interpret the permittivity raw data from the DIS back into spatial volume fraction information. The sensitivity matrix S that was employed in this work was initially developed for (14), where the objective was to compare phase fraction image reconstruction based in over completed dictionaries. In that original work, the DIS reconstructed data was compared with a 12×12 WMS. Hence, the matrix S has a size of 8×144, where the lines represent the sensors of the DIS and the columns represent the cross-section pixels of the WMS. The actual work acknowledges the fact that the matrix S was not fine-tuned for spatial velocity, even so as it performed well in his original study it is been used without adjusts.

Following the method described in section 2.6, which states that axial velocity profile over the pipe cross-section may also be described as a linear operator and, considering the sensor configuration, as described in section 3.1, then should be possible to describe the velocity profile forward problem in the matrix form:

$$\mathbf{v} = \mathbf{W}\mathbf{U} \qquad (3.2)$$

where $\mathbf{v}$ is the 64×1 axial velocity V matrix in lexical order, $\mathbf{W}$ is the 64×144 spatial velocity sensitivity matrix, and $\mathbf{U}$ is the 144×1 vector denoting true axial velocity distribution over the pipe cross section.

The matrix $\mathbf{W}$, has its 64 lines representing correlations between upward and downward layers, and its columns represents 12×12 cross-section area in lexical form, *i.e.*,

144×1 vector. Its was obtained applying Equation (2.45), as follow:

$$\mathbf{W}([u,d],[x,y]) = \frac{S(u,x,y) \cdot S(d,x,y)}{\sum\limits_{u=1}^{8} \sum\limits_{d=1}^{8} S(u,x,y) \cdot S(d,x,y)} \tag{3.3}$$

So, the velocity distribution $\mathbf{U}$ at the position (x,y) in the pipe cross-section may be obtained solving the inverse problem of Equation (3.2) by means of image reconstruction methods, *e.g.*, Linear Back Projection as shown in Equation (3.4):

$$\mathbf{U} = \mathbf{W}^{\mathbf{T}}\mathbf{v} \tag{3.4}$$

As pointed in (15), the cross-covariance between the corresponding receivers, *e.g.*, upstream 1- downstream 1, provides information on the velocity in outer areas of the duct, while, on the other hand, the opposite receptors, *e.g.*, c1,5, provide data on the velocity in the central portion of the duct. This can be visualized in figure 2 where de elements of the matrix $\mathbf{W}$ are shown.

Figure 3.3: Spatial sensitivity distribution matrix

(a) Adjacent electrodes (u1-d1) (b) Opposite electrodes (u1-d5)
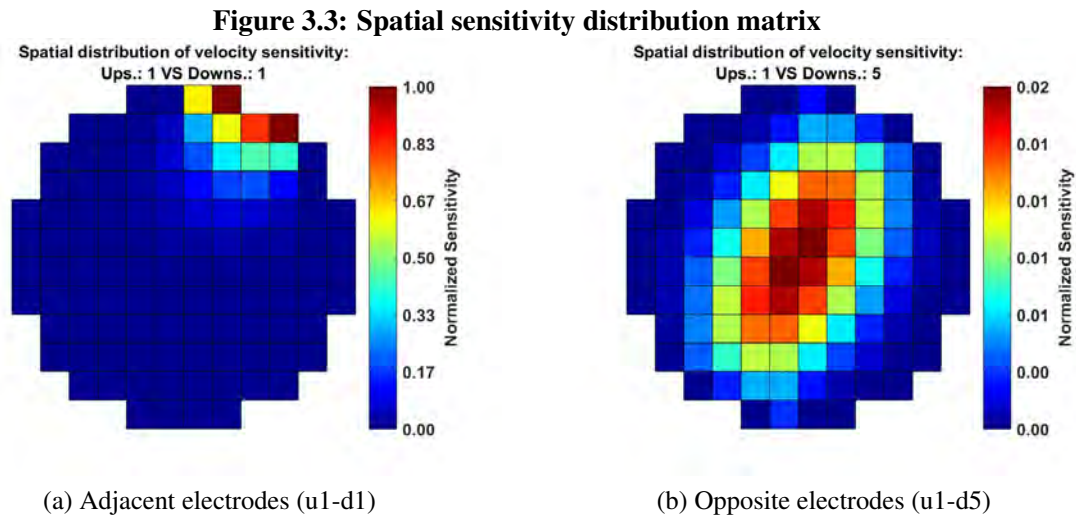
Source: Personal collection.

In order to obtain the in-situ gas phase velocity profile the velocity profile the spatial velocity distribution has to be element-wise multiplied by the gas phase distribution. That is done defining the Hadamard product operator $\odot$, that yields,

$$\mathbf{v_G}(x,y) = \mathbf{U}(x,y) \odot \alpha_{\mathbf{G}}(x,y) \tag{3.5}$$

This operation acts correcting the velocity profile by the in-situ gas-phase fraction

(α_G), hence modulating the velocity values by the presence of more or less gas.

The proposed gas flow rate estimation is done adapting Equation (1.1b) to a matrix form as illustrated in Equation (3.6),

$$Q_G = A_{\mathbf{p}} \sum_x \sum_y \mathbf{v_G}(x,y) \tag{3.6}$$

where $A_{\mathbf{p}}$ represents the image pixel area.

3.4 ALGORITHMS EVALUATION

For the algorithms and reconstruction methods evaluation the synthetic data was tested with a combination of reconstruction methods and velocity algorithms preset in Table 3.2.

Therefore, the parameters analyzed were the estimation deviations relative to the averaged axial velocity, the void fraction and the flow rate. The flow rate was estimated by two approaches, the direct wise-point multiplication of the velocity and void fraction estimation matrices, called Hadamard method and by the multiplication of the averages of the same matrices, called bulk estimation.

The LBP and the NBP has no parameters to adjust, the Landweber iteration, in turn, has questions about the number of iterations, the relaxation parameter and the stopping criteria to be defined.

The main question that emerged was about the relationship between the stop criteria and the number of iterations. More precisely, it was observed that even defining a high number of iterations, some flows stopped earlier. As the stop criteria is usually a measure of image reconstruction evolution from one step to the next, this implies that some flows reconstruction evolution stagnated early. No direct cause for this phenomenon was appointed at time, but a slight correlation with the flow pattern complexity may be suggested.

It was concluded that this variation produced an unfair comparison between processing conditions. Thus, and considering that the number of variables being observed was not small, it was decided to eliminate the stopping criterion. Therefore, all processed flows would go through the total number of designated steps. It did not pass unnoticed that in this condition a careful analysis of the event of semi-convergence phenomenon must be taken.

It was also defined that the relaxation parameter would be kept constant for all flows, following the suggestions of the researched references, (94, 95, 102).

To proceed with a comprehensive analysis of the algorithms, the maximum number of iterations has been set to 10,000, even though it is known that the number of interactions is

Table 3.2: Test matrix for the evalaution of estimation algorithms.

Reconstruction Method	Velocity Algorithms	Iterations
Backprojection	CCOV	1
	SAD	1
	SSD	1
Normalized Backprojection	CCOV	1
	SAD	1
	SSD	1
LIM	COV	1
		5
		10
		50
		100
		500
		1000
		5000
		10000
	SAD	1
		5
		10
		50
		100
		500
		1000
		5000
		10000
	SSD	1
		5
		10
		50
		100
		500
		1000
		5000
		10000

usually no more than 150.

3.4.1 QUANTITATIVE ANALYSIS

Since there was no reference image for the experimental data, as was for synthetic data, the deviation estimation was determined to be a relationship between the scalar reference provided by the loop instrumentation and an average value obtained from the reconstructed data.

For the phase fraction, this value was obtained by averaging the estimated values in time, i.e., all frames, and in the cross-section, that means all pixels. Thus yielding a scalar value that represents the mean phase fraction of the entire flow as represented in Equation (3.7),

$$\overline{\alpha_G} = \frac{1}{FP} \sum_{f=1}^{F} \sum_{x=1}^{X} \sum_{y=1}^{Y} \alpha_G(f, x, y), \qquad (3.7)$$

where F is the number of frames, X and Y the number of pixels in horizontal and vertical directions of the cross-section and P is the total pixel number with flow information ,$i.e.$, $P = XY - dp$ with dp representing the pixels not measured due difference between circular duct area and squared sensitivity matrix.The final value of P is 112.

For velocity profile as the entire flow was used to generate the axial velocity matrix, there was not a necessity of averaging in time. Thus, the procedure adopted to determine the scalar velocity value to be used in comparison with the loop reference and to estimate the velocity deviation was to identify which profile pixels had non-null values, i.e. velocity equal to zero. The motivation for this approach comes from the interpretation that as velocities were identified from interface correlation signals, then zero velocity pixels would imply that there was no gas passage at this location. Therefore, this pixel must be ignored; otherwise, an area larger than the one actually occupied by the gas phase would be considered. Equation (3.8) represents this interpretation.

$$\overline{v_G} = \frac{1}{n} \sum_{x=1}^{X} \sum_{y=1}^{Y} v_G(x, y), \qquad (3.8)$$

The same procedure was adopted for the synthetic data for maintain the analysis consistency.

This kind of deviation analysis is usually taken in absolute form, but as there was interest in observe if the values estimated by the algorithms were biased for more or for less, this procedure was not taken. Hence, positive deviations indicate that the velocity was super estimated and negative deviations indicate that velocity was underestimated, Equation (3.9) synthesizes the methodology adopted.

$$DEV = \left(\frac{measured}{reference} - 1 \right) \cdot 100\% \qquad (3.9)$$

3.5 EXPERIMENTAL APPARATUS

The second dataset was produced at NUEM's flow loop. These experimental data allow to evaluate the robustness of the proposed method in real world situations on which there is less control over the characteristics of the flow.

The NUEM's Loop structure consists of a horizontal flow workbench that possess transparent polycarbonate ducts whit 1 inch internal nominal diameter (26.0 mm), show in Figure 3.4. The facility has capability to produce air-water two-phase flows in the stratified, stratified-wavy, slug, plug and bubbly flow patterns. To do this, it has a single-phase line of gas (air) and single-phase water line, one mixer, a two-phase line, water buffer, water pump with electronic flow control (frequency inverter), single-phase Coriolis flow measurement in gas and water lines each, manual control valves, differential and absolute pressure meters and temperature transducers mounted in the two-phase line.

Figure 3.4: NUEM's Installations and DIS setup

(a) NUEM's Flow Loop Instalations.

(b) DIS and DAQ System detail.

(c) DIS mounted.
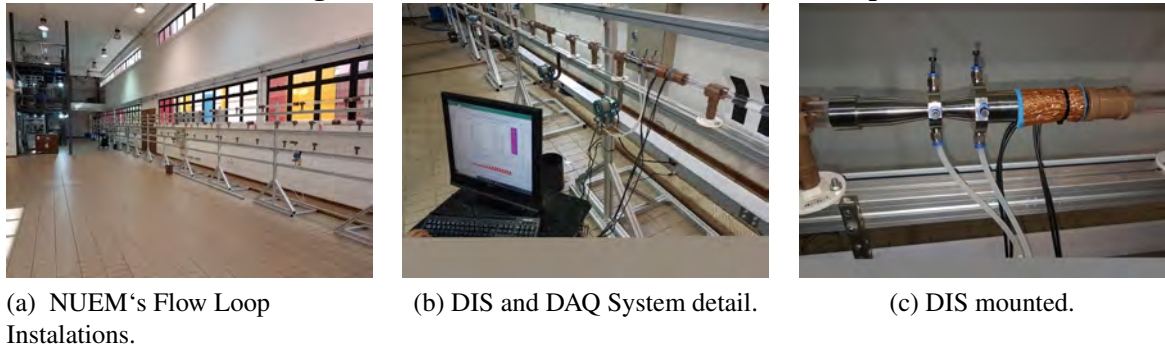
Source: Personal collection.

The facility control and data acquisition system is carried out by a supervisor developed in house, based on LabView. Commands sent from LabView to a frequency inverter (WEG-CFW08), activates and control the centrifugal pump (Fabo brand, model BCIE602 / 7822), allowing the liquid flow rate control. Coriolis meters (Micromotion model F050S11) monitors the single-phase flow of liquid to 1.5 liters per second with 1% uncertainty and through a Foundation Fieldbus network the data is sent to a computer. In addition to the flow measurement, the Coriolis meter provides data on the liquid phase temperature and density. The two-phase line starts from the mixer joining the gas and liquid lines, the mixer also ensures that the water does not enter the gas line.

The two-phase line is formed by a transparent polycarbonate ducts with a thickness of 3 mm, 1 inch nominal internal diameter and 40 m length. The DIS is installed at 24 m meters from the mixer, with the intention of ensuring a flow as developed as possible. DIS read data is sent to a computer via its own DAQ board, based on the wire-mesh sensor electronics.

Figure 3.5: NUEM's flow loop schematics
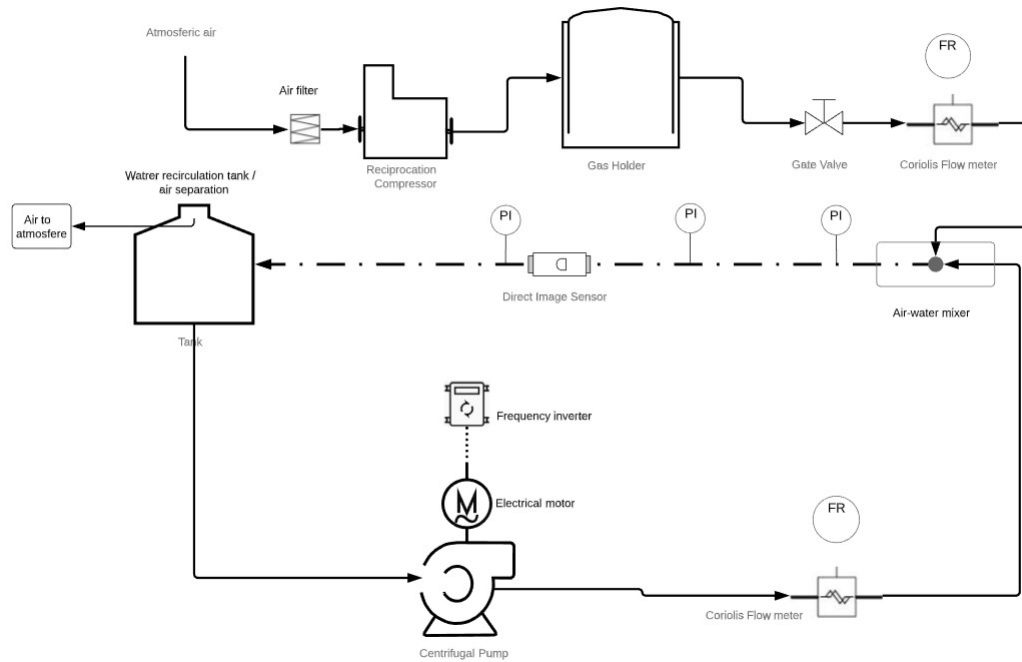
Source: Personal collection.

The select test points cover all stable combinations of superficial velocities for gas and liquid over the nominal facility range at the date, ranging from $0.038\mathrm{ms}^{-1}$ to $3.8\mathrm{ms}^{-1}$ to the gas phase and $0.10\mathrm{ms}^{-1}$ till $3.32\mathrm{ms}^{-1}$ to the liquid phase. The Figure 3.6 shows the test points over the Taitel's flow map (Figure 2.6A). Although the majority of test points are in the slug pattern region, the experiment was able to generate points at the dispersed bubble, stratified and slug-annular transition regions.

3.6   BULK ESTIMATION

The therm bulk, *e.g.*, bulk velocity or bulk temperature is used in mechanical engineering as reference to the average of the value in question.In this work the bulk estimation refers to an alternative procedure to the Hadamard multiplication initially proposed to estimate the flow rate. It consists of averaging each parameter individually, *i.e.*, axial velocity and void fraction, and then multiplying these mean values by the pipe cross-section.

This approach was developed based in the results obtained by (103), where was observed a great deviation in the RMS error in the image but a convergence with the reference

Figure 3.6: Select test points for experimental data set
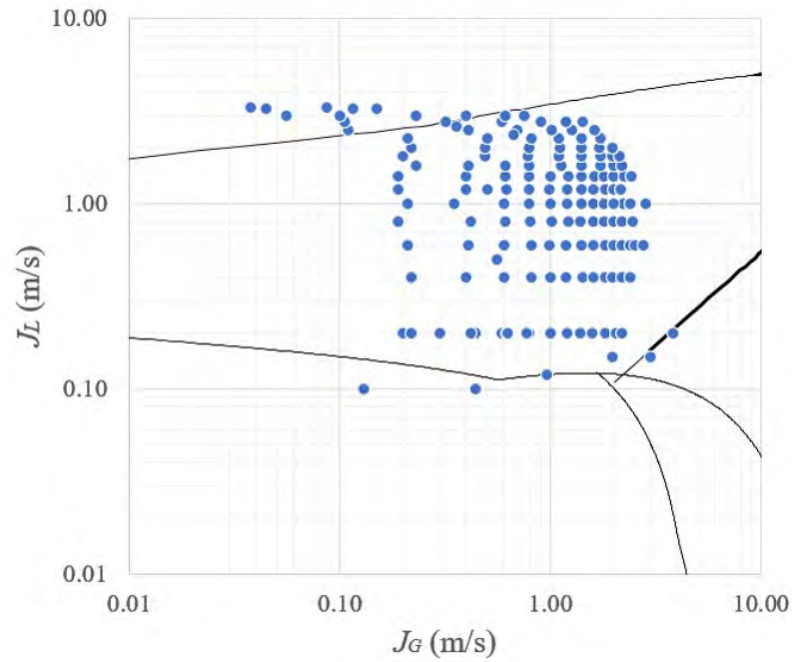
Source: Personal collection.

values in the mean values.

In this sense, it can be considered that the image reconstruction technique plays the role of a regularization method, retrieving information about the velocity and the void fraction from the DIS initial data and so improving the estimation obtained by the direct utilization of the DIS raw data, Equations (3.10) shows how the bulk estimation is processed.

$$q_{bulk} = A \times \overline{V_g} \times \overline{\alpha_G} \tag{3.10}$$

The differences between the Hadamard approach and the bulk estimation can be used to fine tune the spatial distribution of the image reconstruction.

4 RESULTS AND DISCUSSIONS

This chapter is dedicated to the analysis and discussion of the reconstructed data obtained with the methodology described in Chapter 3 and the treatment chosen to be applied to it.

4.1 ALGORITHMS PARAMETERS ADJUSTMENTS

The questions initially posed to be analyzed were: which velocity algorithm provides the best data set for velocity profile reconstruction and what is the optimal number of iterations for both velocity and phase fraction.

For those in which this intermittent attribute was not present the method fail. Thus, confirming the initial assumption of intermittence dependence and also, displaying the differences in sensibility for the algorithms. The cross-covariance yielded a deviation of -100% for the flows without intermittence, which means no velocity at all was perceived. The deviation presented by SAD and SSD only indicates that the algorithms are more sensitive to the flow noise. Figure 4.1 show deviation the LBP and the NBP axial velocity and void fraction, 4.2 shows the deviation and flow rate for LBP and NBP.

Figure 4.1: Deviations for back-projection based reconstruction - Synthetic Data

(a) Axial velocity   (b) Void fraction
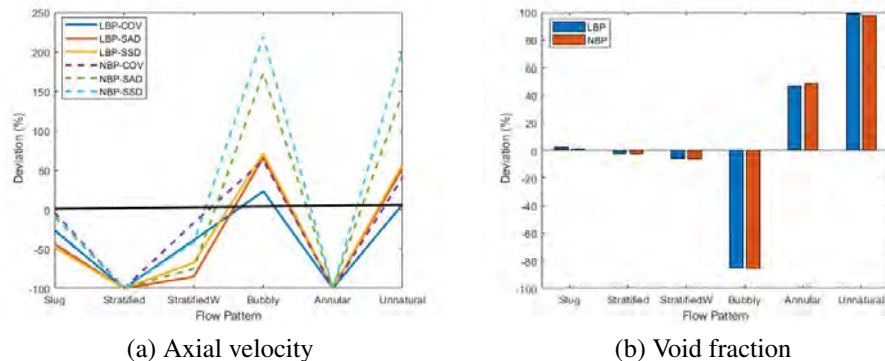
Source: Personal collection.

Figure 4.2: Deviations for back-projection based reconstruction - Synthetic Data

(a) Flow Rate - Hadamard   (b) Flow Rate - Average
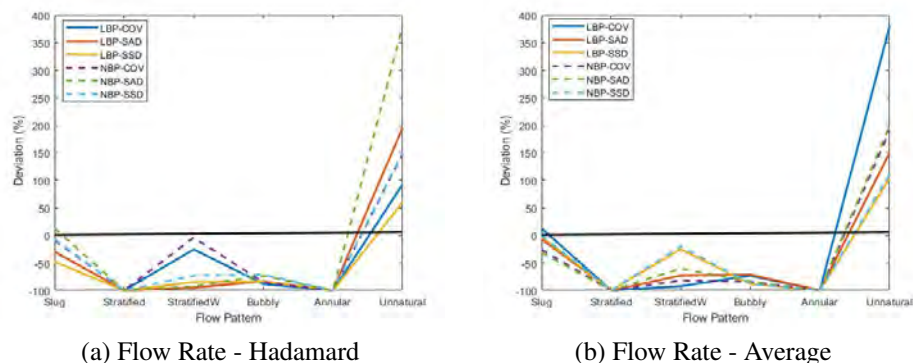
Source: Personal collection.

For the velocity profile reconstruction with the Landweber iteration, the results of the tests suggest that better outcomes are obtained starting from 100 iterations with no improvement been observed after 500 iterations. The deviations for the LIM estimation are shown in figures 4.3 and 4.4.

However, for the flow pattern bubbles the reconstruction with Landweber Iteration obtained good results, that is $+/- 20\%$, with 5 and 10 iterations. Suggesting that the number of iterations can also be considered as a function of the flow pattern in analogy with what (102) suggests about the sensitivity matrix having a flow pattern bias.

Figure 4.3: Deviations for Void Fraction LIM based reconstruction - Synthetic Data
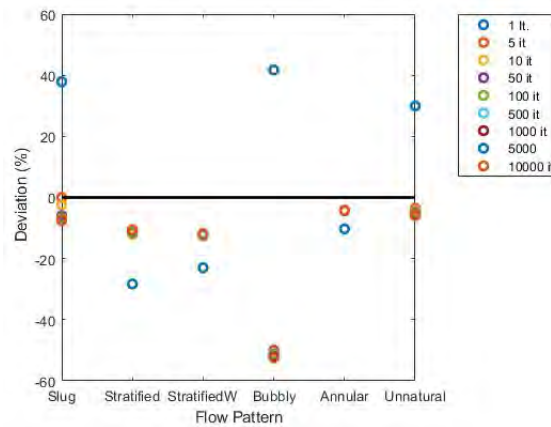
Source: Personal collection.

In Table 4.1 is possible to observe the primary differences between the velocity profiles yielded by the algorithms. The first column presents the gold standard, *i.e.*, the velocity profile calculated from the so-called logical data used to emulate the signal generated by the DIS. The other columns present examples of image reconstruction results for the LBP, nBP, and the Landweber iteration.

The reference standard deviation was calculated by means of the temporal average of all cross-section, that is, of all 53940 frames, thus producing a unique image that represents the flow velocity profile. It is possible to observe that the intermittence of the flow produces an attenuation effect in the magnitude of the velocities. That is, the flow structures that repeat less are attenuated more. That may be compared to the long exposure photography.

For the phase fraction unexpected results was observed. At first a strong tendency to underestimation for all reconstruction methods and velocity algorithms tested as Figure 4.5a shows.

Investigations of the deviation cause were performed by comparing the reference values for the void fraction from the synthetic data with the reconstructed values. The

Figure 4.4: Deviations for Axial velocity LIM based reconstruction - Synthetic Data

(a) COV Algorithm

(b) SAD Algorithm

(c) SSD Algorithm
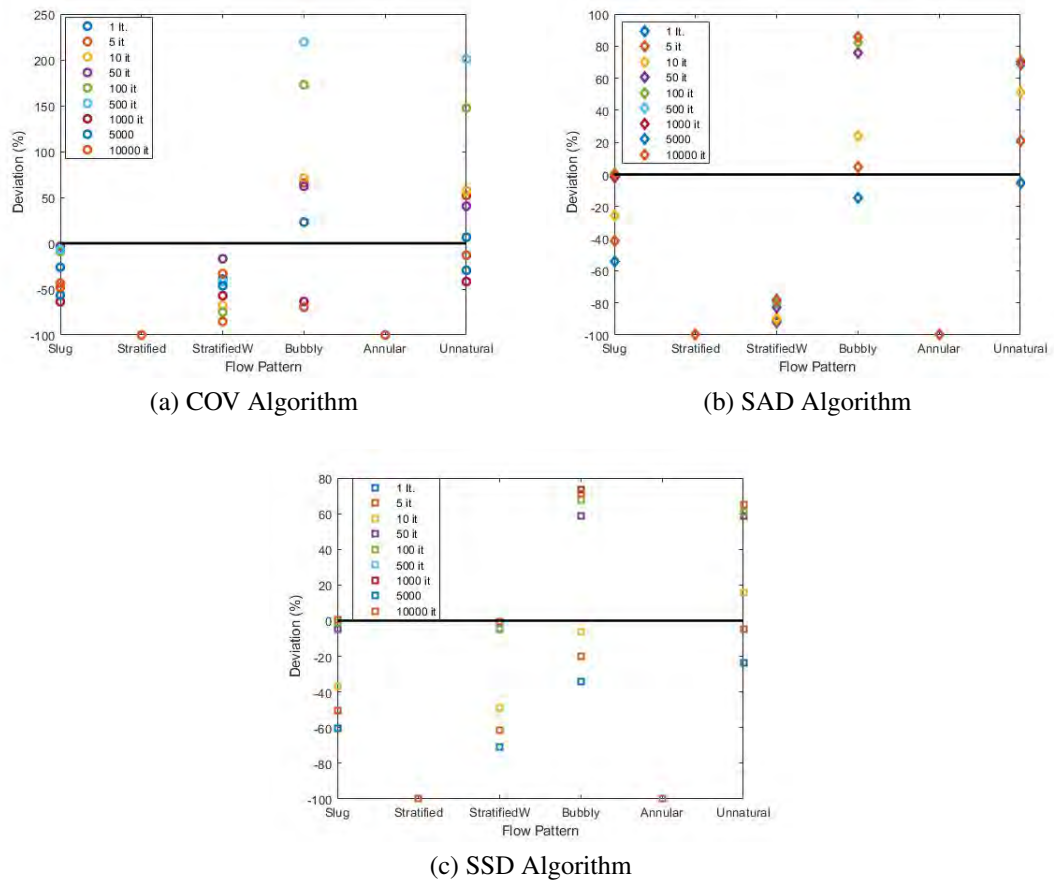
Source: Personal collection.

comparison showed that despite the attenuation the phase fraction variations profile were present.

From these observations, it was investigated if there was a constant between the reference void fraction data and the reconstructed one. This should indicate the presence of a systematic error in the methodology proposed. For each flow-condition tested, similar but not identical ratio values were found between reference and reconstructed data. This confirmed the systematic error hypothesis and suggested that a hysteresis-like phenomenon was happening, that is, the resolution of the inverse problem was consuming part of the signal energy, so the result data was proportional but inferior to the original data.

Therefore, considering that the element common to all reconstructed flows is the sensitivity matrix, its normalization was reevaluated. Tests with air-only and water-only flows proved the correctness of the matrix. However, new tests with other standards indicated that the sensitivity matrix had a susceptibility to flow noise level.

Since, for the velocity profile, this hysteresis-like phenomenon did not occur so

Table 4.1: Synthetic data velocity profile reconstruction with Cross-covariance

Reference	LBP	nBP	LIM
Synthetic Slug			
Synthetic Stratified			
Synthetic Wavy stratified			
Synthetic Bubbly			
Synthetic Annular			
Synthetic Unnatural			
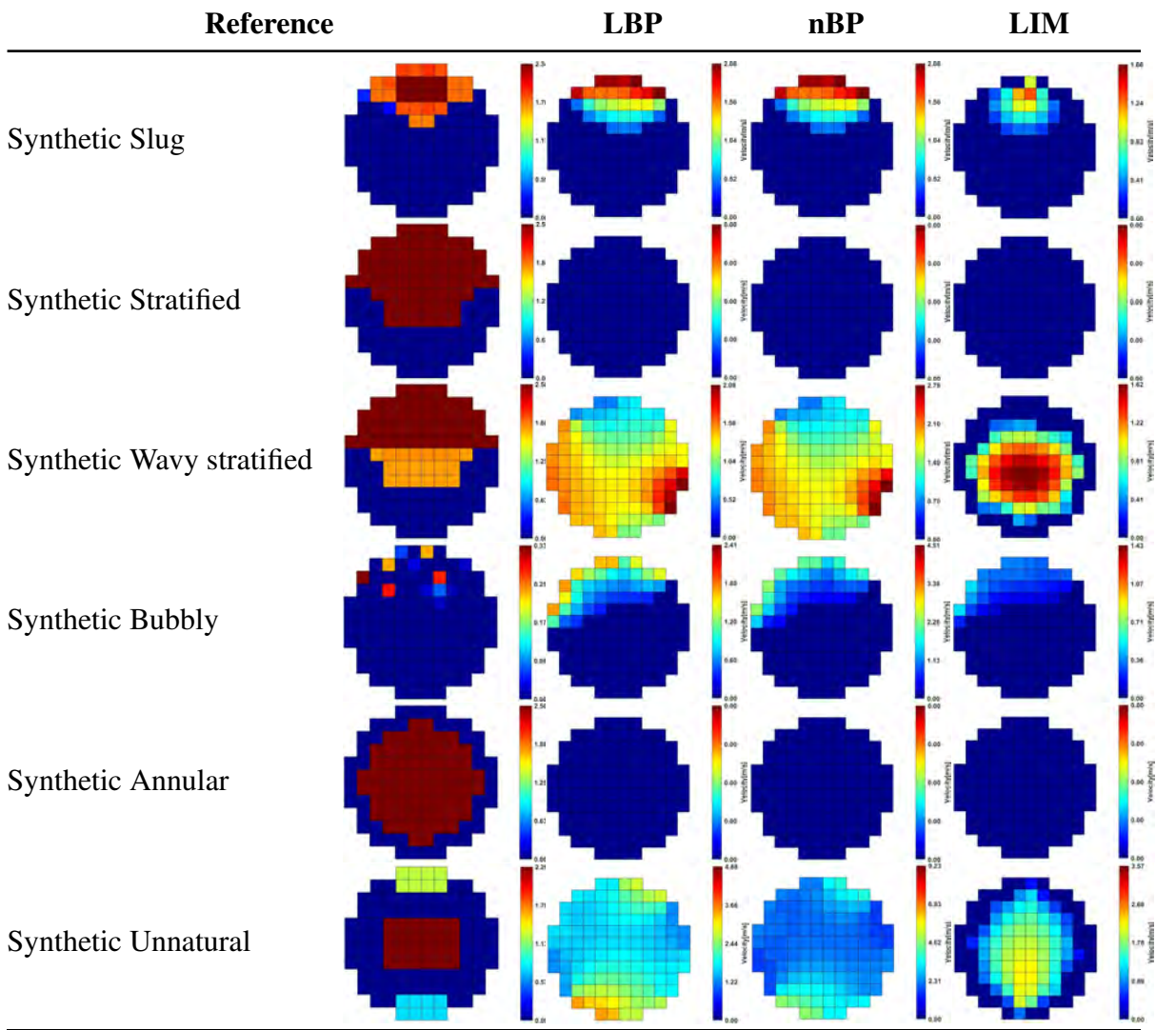
Source: Personal collection.

pronounced, it was tried to re-normalize the S sensitivity matrix similarly to what was done to produce the spatial sensitivity matrix W then producing a new sensitivity matrix defined as S_2, as shown in Equation (4.1), where i, j and k represents the lines, (x, y) the pixel of matrices S and S_2.

$$\mathbf{S_2}(i, [x,y]) = \frac{1}{8} \sum_{k=1}^{8} \left(\frac{S(i,x,y) \cdot S(k,x,y)}{\sum\limits_{i=1}^{8} \sum\limits_{j=1}^{8} S(i,x,y) \cdot S(j,x,y)} \right) \tag{4.1}$$

The new results for void fraction deviation using S_2 can be viewed in Figure 4.5b.

Figure 4.5: Deviation correction of void fraction.

(a) Velocity deviations for LBP

(b) Velocity deviations corrected for LBP
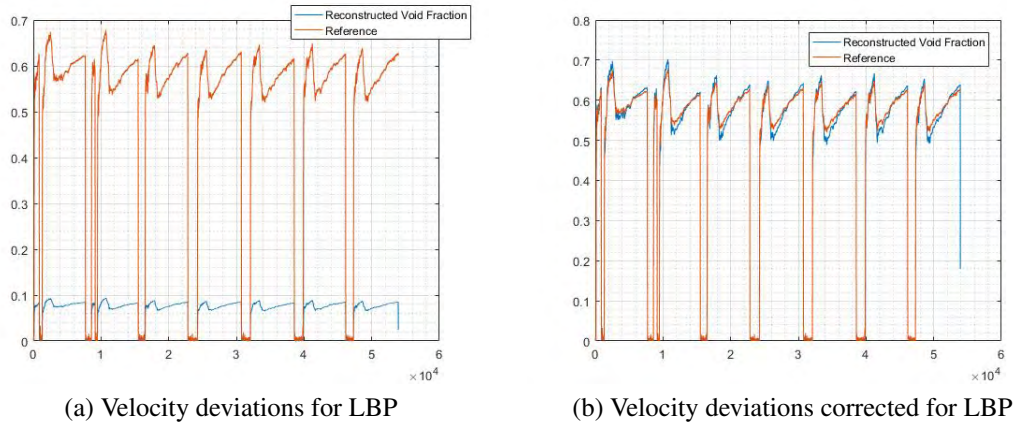
Source: Personal collection.

4.2   EXPERIMENTAL DATA RESULTS

Based on what was observed with the synthetic data in terms of computation time and deviation results the algorithm SAD was elected to be tested with the experimental data using the nBP reconstruction algorithm for the axial velocity estimation and the LIM with 10 iterations for the void fraction.

The next charts summarize the obtained results. To assure the repeatability of the experiment, each point was tested three times. The series of tests was called a batch. Therefore, are three batches covering all experimental points.

Worthwhile to mention that the facility instrumentation only direct provide the volumetric flow rate of the gas phase. The axial velocity used as reference is obtained by mathematical manipulation of Equation 1.1b where the flow rate and the mean void fraction provided by the Coriolis meter and the DIS respectively, hence yielding Equation 4.2;

$$v_p = \frac{Q_p}{A\alpha_p}. \tag{4.2}$$

Although there is no demerit in the use of this data as a reference, it is important to note that this reference was not obtained directly and, therefore, is subject to intrinsic deviations from the calculation. Thus, the emphasis should be given to the flow rate plot.

The Estimated flow rate, Figure 4.6, was generated by applying (3.6). The flow estimation inherits characteristics of velocity and phase fraction reconstructions. In this way, it is possible to identify trends of underestimation at low flow rates and overestimation at high flow rates. This implies that the technique has a limited range of applications in its actual form, which is usual for multiphase measurement systems as already pointed out in section 2.2.1.

Figure 4.6: Gas-phase flow rate estimation
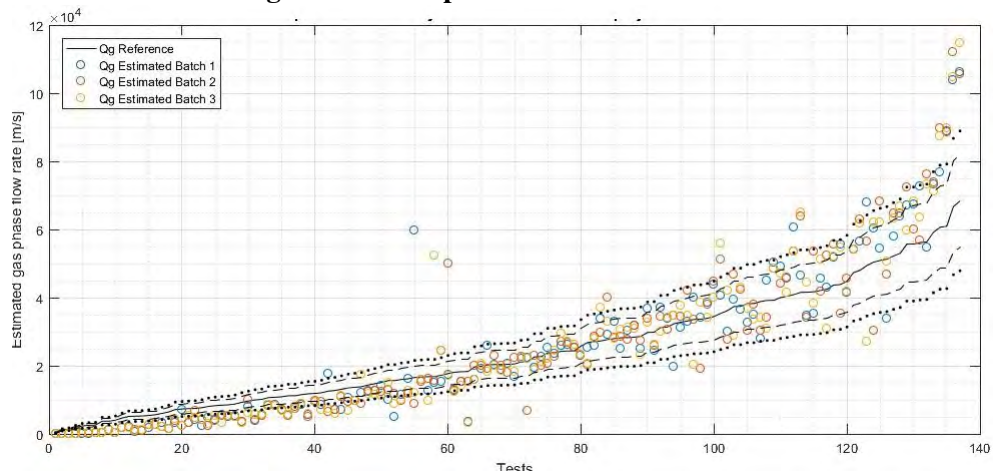
Source: Personal collection.

In the Table 4.2 is possible to observe some velocity profiles that was reconstructed. These images were chosen to represent the variety of phenomena fond, the totality of images may be accessed at $https://github.com/LuisFelipeBotton/VelocityProfiles.git$.

Even though most of the estimated flow rates have fallen within the $+/-20\%$ set, this situation reinforces the previous indication of the need to adjust the sensitivity matrix parameters to the flow conditions.

Table 4.2: Select velocity profiles
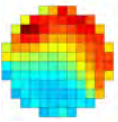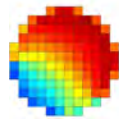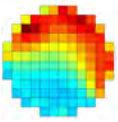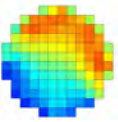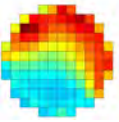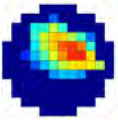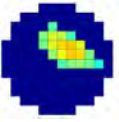
Pattern	$J_g(^m/_s)$	$J_l(^m/_s)$	Reconstruction				
				COV	SAD	SSD	Void Fraction
			LBP				
Slug Flow	1,420	1,402	NBP				
			LIM				

Table 4.2 continued from previous page

Pattern	$J_g(^m/_s)$	$J_l(^m/_s)$		Reconstruction			
				COV	SAD	SSD	Void Fraction
Bubble Flow	0.057	3.000	LBP				
			NBP				
			LIM				
Stratifed Flow	0.132	0.100	LBP				
			NBP				
			LIM				
Stratifed Wavy Flow	3.060	0.148	LBP				
			NBP				
			LIM				

Table 4.2 continued from previous page

Pattern	$J_g(^m/_s)$	$J_l(^m/_s)$		Reconstruction			
				COV	SAD	SSD	Void Fraction
			LBP				
Slug-Annular Flow	3.846	0.180	NBP				
			LIM				

5 CONCLUSIONS

In the following chapter are exposed and contextualized the achievements obtained in the work as well some issues observed and suggestions for the continuity and improvement of the ideas presented.

5.1 CONCLUSION

Knowledge of the parameters of gas-liquid flows is an important factor for the oil industry at various stages of the extraction, refining and distribution process. The current needs of these processes such as accuracy, response time and reliability, among others, drive the development of multiphase measurement techniques.

The research developed in this work focused on reuse and adaptation of known techniques discussed in Chapter 2 like the DIS , ECT, and correlation velocimetry to produce a new methodology that would allow the retrieval of more accurate velocity information by means of velocity profile flow reconstruction (Chapter 3), in order to allow the use of familiar flow ratios relations mostly applied to single-phase for the case of two-phase flow. Thus, simplifying the calculation of gas-phase flow.

Given that the proposed approach is not widespread and therefore there was no substantial prior knowledge of the expected results to be displayed, extensive tests were done and numerous initial assumptions were taken. Hence, the observations and analysis of the results produced by these addressed assumptions presented in Chapter 4 provide some new reference parameters, guides and interesting insights for the continuation of this method development.

Therefore, the present study is characterized as a contribution to the two-phase flow instrumentation area, presenting a new approach to the measurement of the gas-phase velocity with the addition of information about the spatial distribution of the velocity of this phase and as well the gas flow rate.

5.2 FUTURE WORKS

For future works, the main task shall be the extension and evolution of this technique to investigate three-phase flows, e.g., gas-oil-water and the addition of liquid phase information

The following suggestions to future refinement of the technique should be observed:

- Application study of multi-scale processing techniques to reduce the computational time of algorithms and better identify flow characteristics.

- Implementation of SAD algorithm in C language, or applying GPU processing aiming to increase code efficiency and consequently reduce computational time.

- The development of a technique for identification of periodic structures in the flow, then determining an optimal time window interval for velocity data acquisition. Thus including the contribution of smaller structures such as dispersed bubbles in the final flow calculation.

- Test spatial resolution variations of the velocity profile so that the element-wise operation proposed produces more reliable data on the flow rate distribution, *e.g.*, analysis of the effect of changing the resolution of the reconstructed image, from 12 x 12 to 8 x 8, to verify whether the misalignment effect between velocity and weight fraction is mitigated.

- Application of flow pattern identification techniques together with a sensitivity matrix adjustment mechanism.

- Continue development of the direct image sensor data emulation application. Seeking to add physical properties for the generation of flow patterns, e, g, based on statistical distribution of bubbles. Add the ability to work with three-phase air, water and oil flows and create a GUI.

REFERENCES

1 FALCONE, G.; HEWITT, G. F.; ALIMONTI, C. Multiphase Flow Metering: Principles and Applications. *Annals of Physics*, Elsevier, v. 54, p. 300, 2009. ISSN 03767361.

2 BAWAZEER, K.; ZILOUCHIAN, A.; SENIOR, I. Prediction of Products Quality Parameters of a Crude Fractionation Section of an Oil Refinery Using Neural Networks. *Proceedings of International Conference on Neural Networks (ICNN'97)*, IEEE, v. 1, p. 157–162.

3 SULAIYAM, A.-h.; GARY, L. A Flowmeter for Measuring the Dispersed Phase Velocity in Multiphase Flow with Non-uniform Velocity Profiles. *Journal of JSEM*, v. 9, n. Special, p. 7–12, 2009.

4 LIPTAK, B. G. *Flow Measurement*. 1st. ed. [S.l.]: CRC Press, 1993. 211 p. ISBN 9780801983863.

5 COMPANIES, V. *Three-Phase Separator*. Disponível em: <https://vmecompanies.com/oil-water-separator/>.

6 ARNOLD, K.; STEWART, M. *Surface Production Operations*. Cambridge: Elsevier, 2008. ISBN 9780750678537.

7 HERNANDEZ-ALVARADO, F. et al. Comparison of void fraction measurements using different techniques in two-phase flow bubble column reactors. *International Journal of Multiphase Flow*, v. 102, n. February, p. 119–129, may 2018. ISSN 03019322.

8 YAO, J.; TAKEI, M. Application of Process Tomography to Multiphase Flow Measurement in Industrial and Biomedical Fields: A Review. *IEEE Sensors Journal*, v. 17, n. 24, p. 8196–8205, 2017. ISSN 1530437X.

9 Abdul Wahab, Y. et al. A Review of Process Tomography Application in Inspection System. *Jurnal Teknologi*, v. 70, n. 3, p. 35–39, sep 2014. ISSN 2180-3722.

10 WANG, M. *Industrial Tomography Systems and Applications*. 1st. ed. 80 High Street, Sawston, Cambridge, CB22 3HJ, UK: Woodhead Publishing, 2015. 727 p. ISBN 978-1-78242-123-8.

11 XIE, C. G. et al. Electrical capacitance tomography for flow imaging: system model for development of image reconstruction algorithms and design of primary sensors. *IEE Proceedings G Circuits, Devices and Systems*, v. 139, n. 1, p. 89–98, 1992. ISSN 09563768.

12 JIA, J. et al. A novel tomographic sensing system for high electrically conductive multiphase flow measurement. *Flow Measurement and Instrumentation*, Elsevier Ltd, v. 21, n. 3, p. 184–190, 2010. ISSN 09555986.

13 Abdul Wahab, Y. et al. Non-invasive process tomography in chemical mixtures - A review. *Sensors and Actuators, B: Chemical*, v. 210, p. 602–617, 2015. ISSN 09254005.

14 MOURA, H. L. de et al. Image reconstruction algorithms using overcomplete dictionaries for ECT sensor. *8th World Congress on Industrial Process Tomography*, p. 1–8, 2016.

15 FUCHS, A.; ZANGL, H.; WYPYCH, P. Signal modelling and algorithms for parameter estimation in pneumatic conveying. *Powder Technology*, v. 173, n. 2, p. 126–139, 2007. ISSN 00325910.

16 WRASSE, A. D. N. et al. Capacitive Multielectrode Direct-Imaging Sensor for the Visualization of Two-Phase Flows. *IEEE Sensors Journal*, v. 17, n. 24, p. 8047–8058, 2017. ISSN 1530437X.

17 BRENNEN, C. E. Introduction to Multiphase Flow. In: *Fundamentals of Multiphase Flow*. Cambridge: Cambridge University Press, 2014. p. 1–29. ISBN 9783319587172.

18 KON, K. *Easy way to improve your blood circulation*. 2019. Disponível em: <https://gilvydisvein.com/easy-ways-to-improve-your-blood-circulation/>.

19 INAGLORY, B. *Golden Gate Bridge at sunset and coverd by fog*. 2009. Disponível em: <https://en.wikipedia.org/wiki/File:Golden_Gate_Bridge_at_sunset_1.jpg>.

20 SIGURDSSON, H. et al. *The Encyclopedia of Volcanoes*. [S.l.]: Academic Press, 1999. 1417 p. ISBN 978-0-08-054798-5.

21 IMMELMAN284. *Meeting of waters from the air manaus brazil*. 2011. Disponível em: <https://pt.wikipedia.org/wiki/Ficheiro:Meeting_of_waters_from_the_air_manaus_brazil.JPG>.

22 BRENNEN, C. E. Multiphase flow. In: ____. *Thermo-Hydraulics of Nuclear Reactors*. [S.l.]: Cambridge University Press, 2016. p. 90–126.

23 SPINRAD, B. I.; MARCUM, W. *Nuclear reactor*. 2019.

24 SUN, B. *Multiphase Flow in Oil and Gas Well Drilling*. Singapore: John Wiley & Sons Singapore Pte. Ltd, 2016. 1–217 p. ISBN 9781118720288.

25 UEBEL, R. Coordinating geopolitics, political geography and energy: some inputs from the recent history to the present days. *Energy Bulletin*, 01 2016.

26 COMPANY, M. W. C. *MWCC Takes Delivery of Full Containment System*. 2015. Disponível em: <https://www.oilandgaspeople.com/news/1658/mwcc-takes-delivery-of-full-containment-system/>.

27 SANTOS, E. N. dos. *Development and application of wire-mesh sensors for high-speed multiphase flow imaging*. 205 p. Tese (Doutorado) — Federal University of Technology, 2015.

28 WRASSE, A. d. N. *Sensor capacitivo para imageamento direto de escoamentos bif{á}sicos*. 82 p. Tese (Doutorado) — Federal University of Technology-Paran{á}, 2015.

29 Da Silva, M. J. *Impedance Sensors for Fast Multiphase flow*. 170 p. Tese (Doutorado) — Technische Universität Dresden, 2008.

30 MCQUILLAN, K. W.; WHALLEY, P. B. Flow patterns in vertical two-phase flow. *International Journal of Multiphase Flow*, v. 11, n. 2, p. 161–175, 1985. ISSN 03019322.

31 ROUHANI, S. Z.; SOHAL, M. S. Two-phase flow patterns: A review of research results. *Progress in Nuclear Energy*, v. 11, n. 3, p. 219–259, 1983. ISSN 01491970.

32   CHUANG, T. J.; HIBIKI, T. *Interfacial forces used in two-phase flow numerical simulation*. [S.l.]: Pergamon, oct 2017. 741–754 p.

33   TALPERT, A. C. N. *ANALYSIS OF INTERFACIAL FORCES ON THE PHYSICS OF TWO-PHASE FLOW AND HYPERBOLICITY OF THE TWO-FLUID MODEL*. 77 p. Tese (Doutorado) — University of Illinois, 2013.

34   YU, Z.; ZHU, B.; CAO, S. Interphase force analysis for air-water bubbly flow in a multiphase rotodynamic pump. *Engineering Computations (Swansea, Wales)*, v. 32, n. 7, p. 2166–2180, oct 2015. ISSN 02644401.

35   KIM, T. H. et al. Visual observations of flow patterns in downward air-water two-phase flows in a vertical narrow rectangular channel. *Annals of Nuclear Energy*, Pergamon, v. 114, p. 384–394, apr 2018. ISSN 0306-4549.

36   THOME, J. R.; CIONCOLINI, A. *Encyclopedia of Two-Phase Heat Transfer and Flow*. [S.l.: s.n.], 2017. 5–45 p. ISBN 9789814623216.

37   BHAGWAT, S. M.; GHAJAR, A. J. Similarities and differences in the flow patterns and void fraction in vertical upward and downward two phase flow. *Experimental Thermal and Fluid Science*, Elsevier, v. 39, p. 213–227, may 2012. ISSN 0894-1777.

38   WANG, G. et al. Experimental study on interfacial structure and interfacial area transport in downward two-phase flow. *International Journal of Heat and Mass Transfer*, Pergamon, v. 106, p. 1303–1317, mar 2017. ISSN 0017-9310.

39   De Kerpel, K. et al. Capacitance sensor measurements of upward and downward two-phase flow in vertical return bends. *International Journal of Multiphase Flow*, Pergamon, v. 64, p. 1–10, sep 2014. ISSN 0301-9322.

40   MANDHANE, J.; GREGORY, G.; AZIZ, K. A flow pattern map for gas—liquid flow in horizontal pipes. *International Journal of Multiphase Flow*, Pergamon, v. 1, n. 4, p. 537–553, oct 1974. ISSN 0301-9322.

41   PEREYRA, E. et al. A methodology and database to quantify the confidence level of methods for gas–liquid two-phase flow pattern prediction. *Chemical Engineering Research and Design*, Elsevier, v. 90, n. 4, p. 507–513, apr 2012. ISSN 0263-8762.

42   BAKER, O. Designing for Simultaneous Flow of Oil and Gas. *The Oil and Gas Journal*, v. 53, n. July, p. 185–195, 1954.

43   TAITEL, Y.; DUKLER, A. E. A model for predicting flow regime transitions in horizontal and near horizontal gas-liquid flow. *AIChE Journal*, v. 22, n. 1, p. 47–55, 1976. ISSN 15475905.

44   TAITEL, Y.; BORNEA, D.; DUKLER, A. E. Modelling flow pattern transitions for steady upward gas-liquid flow in vertical tubes. *AIChE Journal*, Wiley-Blackwell, v. 26, n. 3, p. 345–354, may 1980. ISSN 0001-1541.

45   WEISMAN, J. et al. Effects of fluid properties and pipe diameter on two-phase flow patterns in horizontal lines. *International Journal of Multiphase Flow*, Pergamon, v. 5, n. 6, p. 437–462, dec 1979. ISSN 0301-9322.

46   Pinto del Corral, N. *Analysis of Two-Phase Flow Pattern Maps*. Brno, 2014.

47 ROSA, E. S. *Escoamento Multifásico Isotérmico*. 1st. ed. Porto Alegre: [s.n.], 2012. 260 p. ISBN 9788540700703.

48 SHOHAM, O. *Mechanistic modeling of gas-liquid two-phase flow in pipes*. [S.l.]: Society of Petroleum Engineers, 2006. ISBN 9781555631079.

49 FALCONE, G. et al. Multiphase Flow Metering: Current Trends and Future Developments. In: *SPE Annual Technical Conference and Exhibition*. [S.l.]: Society of Petroleum Engineers, 2001.

50 ARNOLD, K. *Surface production operations*. Burlington, MA: Elsevier, 1999. ISBN 0884158225.

51 YADIGAROGLU, G. *Introduction to multiphase flow : basic concepts, applications and modelling*. Cham: Springer, 2018. ISBN 978-3-319-58717-2.

52 AZZOPARDI, B. J. *Gas-liquid flows*. New York: Begell House, 2006. ISBN 9781567002331.

53 FLACIMAIGE, J.; DECARRE, S. *Multiphase Production: Pipeline Transport , Pumping and Metering*. 1st. ed. Paris, France: IFP Publications, 2008. ISBN 978-2-718-0913-5.

54 ZHANG, Y. et al. Acoustic wave propagation in bubbly flow with gas, vapor or their mixtures. *Ultrasonics Sonochemistry*, Elsevier, v. 40, n. February 2017, p. 40–45, 2018. ISSN 18732828.

55 JONES, S. W.; AMBLARD, A.; FAVREAU, C. Interaction of an ultrasonic wave with a bubbly mixture. *Experiments in Fluids*, v. 4, n. 6, p. 341–349, Nov 1986. ISSN 1432-1114.

56 CAVARO, M. A void fraction characterisation by low frequency acoustic velocity measurements in microbubble clouds. *Physics Procedia*, v. 70, p. 496–500, 2015. ISSN 18753892.

57 AL-LABABIDI, S. et al. Gas Void Fraction Measurement in Two-Phase Gas/Liquid Slug Flow Using Acoustic Emission Technology. *Journal of Vibration and Acoustics*, v. 131, n. 6, p. 0645011–0645017, nov 2009. ISSN 1048-9002.

58 ADDALI, A. et al. Measurement of two-phase slug velocity in pipes with acoustic emission. n. October, p. 1–9, 2014.

59 KAK, A.; SLANEY, M. Principles of computerized tomographic imaging ieee press. *New York*, 1988.

60 DYAKOWSKI, T. Process tomography applied to multi-phase flow measurement. *Measurement Science and Technology*, IOP Publishing, v. 7, n. 3, p. 343, 1996.

61 WILLIAMS, R. A.; JIA, X. Tomographic imaging of particulate systems. *Advanced Powder Technology*, Elsevier, v. 14, n. 1, p. 1–16, 2003.

62 SUPARDAN, M. D. et al. The investigation of gas holdup distribution in a two-phase bubble column using ultrasonic computed tomography. *Chemical Engineering Journal*, v. 130, n. 2-3, p. 125–133, 2007. ISSN 13858947.

63   GLADDEN, L. et al. Mri visualisation of two-phase flow in structured supports and trickle-bed reactors. *Catalysis Today*, Elsevier, v. 79, p. 203–210, 2003.

64   CECCIO, S.; GEORGE, D. A review of electrical impedance techniques for the measurement of multiphase flows. *Journal of fluids engineering*, American Society of Mechanical Engineers Digital Collection, v. 118, n. 2, p. 391–399, 1996.

65   PRASSER, H.-M.; BÖTTGER, A.; ZSCHAU, J. A new electrode-mesh tomograph for gas–liquid flows. *Flow measurement and instrumentation*, Elsevier, v. 9, n. 2, p. 111–119, 1998.

66   Da Silva, M. J.; SCHLEICHER, E.; HAMPEL, U. Capacitance wire-mesh sensor for fast measurement of phase fraction distributions. *Measurement Science and Technology*, v. 18, n. 7, p. 2245–2251, 2007. ISSN 13616501.

67   CARTELLIER, A. Measurement of gas phase characteristics using new monofiber optical probes and real-time signal processing. *Nuclear Engineering and Design*, Elsevier, v. 184, n. 2-3, p. 393–408, 1998.

68   DELHAYE, J.-M.; JR, O. C. J. *Summary on experimental methods for statistical transient analysis of two-phase gas-liquid flow*. [S.l.], 1976.

69   LAGE, P.; ESPÓSITO, R. Experimental determination of bubble size distributions in bubble columns: prediction of mean bubble diameter and gas hold up. *Powder technology*, Elsevier, v. 101, n. 2, p. 142–150, 1999.

70   HASSAN, Y. A.; DOMINGUEZ-ONTIVEROS, E. Flow visualization in a pebble bed reactor experiment using piv and refractive index matching techniques. *Nuclear Engineering and Design*, Elsevier, v. 238, n. 11, p. 3080–3085, 2008.

71   BOYER, C.; DUQUENNE, A.-M.; WILD, G. Measuring techniques in gas–liquid and gas–liquid–solid reactors. *Chemical Engineering Science*, Elsevier, v. 57, n. 16, p. 3185–3215, 2002.

72   JR, O. C. J.; DELHAYE, J.-M. Transient and statistical measurement techniques for two-phase flows: a critical review. *International Journal of Multiphase Flow*, Elsevier, v. 3, n. 2, p. 89–116, 1976.

73   BRUUN, H. Hot-film anemometry in liquid flows. *Measurement Science and Technology*, IOP Publishing, v. 7, n. 10, p. 1301, 1996.

74   GUO, G. et al. Iterative reconstruction algorithm for the inverse problems in electrical capacitance tomography. *Flow Measurement and Instrumentation*, Elsevier Ltd, v. 64, n. December 2017, p. 204–212, 2018. ISSN 09555986.

75   YANG, W. Q.; PENG, L. Image reconstruction algorithms for electrical capacitance tomography. *Measurement Science and Technology*, v. 14, n. 1, p. R1–R13, jan 2003. ISSN 0957-0233.

76   HE, R. et al. Principles and Industrial Applications of Electrical Capacitance Tomography. *Measurement and Control*, v. 30, n. 7, p. 197–200, 2015. ISSN 0020-2940.

77   SAIED, I.; MERIBOUT, M. Electronic hardware design of electrical capacitance tomography systems. *Philosophical Transactions of the Royal Society A: Mathematical, Physical and Engineering Sciences*, v. 374, n. 2070, 2016. ISSN 1364503X.

78   ALME, K. J.; MYLVAGANAM, S.; MEMBER, S. Electrical Capacitance Tomography — Sensor Models , Design , Simulations , and Experimental Verification. *IEEE Sensors Journal*, v. 6, n. 5, p. 1256–1266, 2006.

79   WANG, B. et al. A high-speed data acquisition system for ECT based on the differential sampling method. *IEEE Sensors Journal*, v. 5, n. 2, p. 308–311, 2005. ISSN 1530437X.

80   GROHS, P.; KERETA, Ž.; WIESMANN, U. A shearlet-based fast thresholded Landweber algorithm for deconvolution. *International Journal of Wavelets, Multiresolution and Information Processing*, v. 14, n. 05, p. 1650032, 2016. ISSN 0219-6913.

81   PAREDES, L. L. T.; VILOCHE, F. S. B. Métodos iterativos para reconstrução de imagens. *Proceeding Series of the Brazilian Society of Applied and Computational Mathematics*, v. 2, n. 1, p. 1–6, 2015.

82   SUN, B. et al. A new linear back projection algorithm to electrical tomography based on measuring data decomposition. *Measurement Science and Technology*, IOP Publishing, v. 26, n. 12, p. 125402, 2015. ISSN 13616501.

83   KITIĆ, S. et al. Physics-driven inverse problems made tractable with cosparse regularization. *IEEE Transactions on Signal Processing*, 2016. ISSN 1053587X.

84   LI, K.; CONG, S. A review of image reconstruction algorithms in electrical capacitance tomography. In: *2018 Tenth International Conference on Advanced Computational Intelligence (ICACI)*. [S.l.]: IEEE, 2018. p. 128–133. ISBN 978-1-5386-4362-4.

85   CUI, Z. et al. A review on image reconstruction algorithms for electrical capacitance/resistance tomography. *Sensor Review*, v. 36, n. 4, p. 429–445, sep 2016. ISSN 0260-2288.

86   ISAKSEN, Ø. A review of reconstruction techniques for capacitance tomography. *Measurement Science and Technology*, v. 7, n. 3, p. 325–337, mar 1996. ISSN 0957-0233.

87   LIU, Z. et al. Landweber iterative algorithm based on regularization in electromagnetic tomography for multiphase flow measurement. *Flow Measurement and Instrumentation*, Elsevier Ltd, v. 27, p. 53–58, 2012. ISSN 09555986.

88   GUAN, H.; GORDON, R.; ZHU, Y. Combining various projection access schemes with the algebraic reconstruction technique for low-contrast detection in computed tomography. *Physics in Medicine and Biology*, v. 43, n. 8, p. 2413–2421, 1998. ISSN 00319155.

89   WOLF, D.; LUBK, A.; LICHTE, H. Weighted simultaneous iterative reconstruction technique for single-axis tomography. *Ultramicroscopy*, North-Holland, v. 136, p. 15–25, jan 2014. ISSN 03043991.

90   AARLE, W. van et al. The ASTRA Toolbox: A platform for advanced algorithm development in electron tomography. *Ultramicroscopy*, North-Holland, v. 157, p. 35–47, oct 2015. ISSN 0304-3991.

91   BERNAL, J.; JAVIER, S. Use of Filtered Back-projection Methods to Improve CT Image Reconstruction. n. September 2009, 2015.

92 NOWINSKI, W. L. The iterated normalized backprojection method of image reconstruction. *Lecture Notes in Computer Science (including subseries Lecture Notes in Artificial Intelligence and Lecture Notes in Bioinformatics)*, v. 719 LNCS, p. 556–563, 1993. ISSN 16113349.

93 A., F. et al. Impact of iterative reconstruction vs. filtered back projection on image quality in 320-slice CT coronary angiography. *Medicine (United States)*, v. 96, n. 48, p. 1–5, 2017. ISSN 1536-5964.

94 BILCU, R. C. et al. Landweber image restoration with adaptive step-size. *2007 9th International Symposium on Signal Processing and its Applications, ISSPA 2007, Proceedings*, p. 1–4, 2007.

95 Lei Liang; Yuanchang Xu. Adaptive Landweber method to deblur images. *IEEE Signal Processing Letters*, v. 10, n. 5, p. 129–132, may 2003. ISSN 1070-9908.

96 ZHU, L. et al. Analysis of flow cytometric fluorescence lifetime with time-delay estimation of pulse signals. *Sensors (Switzerland)*, v. 18, n. 2, p. 1–14, 2018. ISSN 14248220.

97 SHASWARY, E.; XU, Y.; TAVAKKOLI, J. Performance study of a new time-delay estimation algorithm in ultrasonic echo signals and ultrasound elastography. *Ultrasonics*, Elsevier B.V., v. 69, p. 11–18, 2016. ISSN 0041624X.

98 TAL, B. et al. Cross-correlation based time delay estimation for turbulent flow velocity measurements: Statistical considerations. *Physics of Plasmas*, v. 18, n. 12, 2011. ISSN 1070664X.

99 BOTTON, L. F. et al. Twin Direct-Imaging Sensor for Flow Velocity Profiling in Two-Phase Mixtures. In: *Proceedings of IEEE Sensors*. [S.l.]: IEEE, 2018. v. 2018-Octob, p. 1–4. ISBN 9781538647073. ISSN 21689229.

100 RAOL, J. R. *Multi-sensor data fusion with MATLAB*. Broken Sound Parkway, NW: CRC Press, 2009. 568 p. ISBN 9781439800034.

101 SAMBASUBRAMANIAN, S. *Comparison of the performance of different time delay estimation techniques for ultrasound elastography*. 67 p. Tese (Doutorado) — Texas A&M University, 2010.

102 YANG, W.; SPINK, D.; YORK, T. An image-reconstruction algorithm based on Landweber's iteration method for electrical-capacitance tomography. *Measurement Science and Technology*, v. 10, n. 11, p. 1065–1069, 1999.

103 ZHENG, J. et al. A Benchmark Dataset and Deep Learning-Based Image Reconstruction for Electrical Capacitance Tomography. *Sensors*, v. 18, n. 11, p. 3701, oct 2018. ISSN 1424-8220.

104 CALLEGARO, L. *Electrical impedance: Principles, measurement, and applications*. [S.l.: s.n.], 2012. 1–279 p. ISBN 9781439849118.

105 GRIFFITHS, D. J. *Introduction to Electrodynamics*. Fourth edi. Upper Saddle River, N.J: Prentice Hall, 1999. 302 p. ISBN 9780321856562.

APPENDIX A – IMPEDANCE METERING

This chapter is dedicated to describe the Direct Image Sensor, its application characteristics, properties and DAQ electronics. For a more comprehensive background, the joint electrical impedance measurement theory underneath it is also presented at the beginning and connections with previous chapter ECT theory are established.

A.1 ELECTRICAL IMPEDANCE

Matter in general can be classified based in its electromagnetic properties. Still, even that some fluids such as ferrofluids have appreciable magnetic properties, that's not the rule, as cited by Da Silva (29). Notwithstanding, all fluids present electrical properties. The following description is focused in this property, and based on the previous works from Da Silva (29) and the books of Callegaro (104) and Griffiths (105).

In electrodynamics electrical impedance (Z) is a concept which describes the opposing relationship between current (I) and voltage (V) in an electrical circuit. So, impedance extends the concept of resistance (R) for alternating current (AC) circuits, and can also be understood as the total opposition of the circuit to current flow. Hence, considering a sinusoidal voltage input $v(t) = V cos(\omega t + \theta_V)$ at angular frequency $\omega = 2\pi f$, to which a phasor $V = V_{MAX} exp(j\theta_V)$ can be associated with and an also sinusoidal current $i(t) = I_{MAX} cos(\omega + \theta_I)$ at same angular frequency, where $I = I_{MAX} exp(j\theta_I)$ is the associated phasor to $i(t)$, the driving point impedance $Z(\omega)$ of the circuit at frequency ω can be defined as the ratio of the phasors V and I, as shown in Eq. (A.1).

$$Z(\omega) = \frac{V}{I} \tag{A.1}$$

Although not a phasor itself, impedance shall be represented as a complex grandeur with resistance as the real portion, representing the losses as heat (Joule effect), and reactance (X), representing the measure of reactive energy stored in the circuit during one period, as the complex portion.

However Cartesian complex number representation, $Z = R + jX$, where $j = \sqrt{-1}$ represents the imaginary unit, is often more powerful representation for circuit analysis use, the polar form $Z = R\angle\theta$ with resistance as magnitude and θ as phase angle is also found in literature. Immediately thereafter, impedance is also expressed in ohms (Ω).

For ideal DC (Direct Current) driven circuits, there is no distinction between impedance and ohmic resistance (R), thus the reactance (X) component may be neglected since in ideal steady state DC circuits the frequency is null. One can also interpret this case as an impedance with zero phase angle, eq.(A.2).

$$R \equiv Z(0) = \frac{V}{I} \tag{A.2}$$

Occasionally it becomes more convenient to use other derived quantities related to impedance in order to obtain information about the physical system at analysis. One of these other quantities, generally called immittances, is the inverse of the impedance which is called admittance and is expressed according to eq.(A.3), where G represents the conductance and B the susceptance, opposite terms to the resistance and reactance respectively.

$$Y = \frac{I}{V} = \frac{1}{Z} \equiv G + jB \tag{A.3}$$

This notion of impedance is useful for performing analysis of material characteristics in presence of AC signals, because it allows relating an applied sinusoidal voltage $v(t)$ and the resulting electrical current $i(t)$ to a material property called permittivity in the form of a simple linear law.

Permittivity is a physical grandeur which describes the behavior of a dielectric material in presence of an electric field (E). It quantifies the tendency to polarization of this material, and consequentially, the material ability to store the field E in its interior. The standard SI unit for permittivity is Farad per meter (Fm^{-1}).

In impedance measurement to investigate fluids it is appropriate to deepen this definition. The parameter used to characterize materials is, in fact, a dimensionless quantity called complex relative permittivity (ε) gives by (29) and described in Eq. A.4,

$$\varepsilon = \varepsilon' - j\varepsilon''. \tag{A.4}$$

The real portion ε' represents the material capacity to store energy (often refereed as permittivity) and the complex portion ε'', describing the losses within the material. Among these losses, we can mention dieletric loss due to the effects of ionization and by relaxation. The detailing on the concepts of complex electrical permittivity based on Maxwell's equations and on losses phenomena is found in (29).

This quantity is related to the complex absolute permittivity (ε_a) and the permittivity of free space (ε_0) as shown in eq. (A.5). The free space, or vacuum, permittivity is the lowest possible and has an approximate value of $8,85x10^{-12}Fm^{-1}$.

$$\varepsilon = \frac{\varepsilon_a}{\varepsilon_0} \tag{A.5}$$

Considering that most insulating materials can be treated as a linear and homogeneous dielectric (104), which implies that between the induced dipole in material and the external electric field, there is a linear relationship. This relationship between the dielectric displacement field (D) and the electric field (E) is given by a scale factor corresponding to the complex permittivity as shown in equation A.6. The fields D and E describe the interaction between charged objects, and are assumed to present sinusoidal alternating variations with time (29), D is related to charge densities associated with this interaction and E is related to the forces and potential differences.

$$D = \varepsilon E \tag{A.6}$$

The process to obtain impedance values for investigating properties of material substances usually employs a measure cell or probe. The simplest cell is composed by two identical parallel plane electrodes as shown in Figure A.1. The relationship connecting electrical properties of the substance between the plates with the measure cell admittance is,

Figure A.1: Simple measure cell.
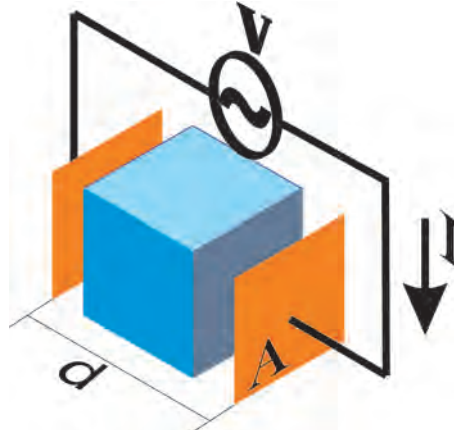
Source: Adapted from (66)

$$Y = j\omega \kappa_g \varepsilon_a. \tag{A.7}$$

Where the geometry factor κ_g reflects the ratio of cross-sectional area of the sampled fluid volume and the length or distance between electrodes. For a simple cell like one shown it could be approximated by,

$$\kappa_g = \frac{l^2}{d} = \frac{A}{d}. \qquad (A.8)$$

Being A the squared plates area and d the distance separating the plates.

It is known that relaxation functions like ones proposed by Debye and Cole-Cole intent to predict the permittivity behavior of fluids up to GHz frequency range. On the other hand, as the utilized sensor (DIS) work only in the MHz frequency range, the permittivity can be given as proposed by (29),

$$\varepsilon_? = \varepsilon_r - j\frac{\sigma}{\omega\varepsilon_0} \qquad (A.9)$$

with $\varepsilon_?$ representing dielectric constant and σ the material's conductivity

While the complex permittivity ε is only dependent from the material, Y and Z also depends on the experimental setup via κ_g. Da Silva (29) also brings useful relations between some impedance-related functions alongside with the known capacitance equation:

$$C = \kappa_g \varepsilon_0 = \varepsilon_0 \frac{A}{d} \qquad (A.10)$$

gives base to rewrite Y as follows;

$$Y = G + j\omega C = \kappa_g \sigma + j\omega\varepsilon_0 \frac{A}{d} \qquad (A.11)$$

Finally, eq.(A.11) demonstrates how variations in the material and consequently in the permissiveness of the medium interrogated can be related to voltage and current variations by means of the impedance.

A.1.1 IMPEDANCE MEASUREMENT TECHNIQUE - AUTO BALANCED BRIDGE

In view of that permittivity and the associated impedance are complex quantities, both the real and the imaginary portions need to be measured, in what is commonly called vector of measurements.

There are a wide range of techniques for impedance measurement. The choice of the most indicated technique is not arbitrary, lean on the measurement requirements, such as measurement range, accuracy and precision required, system complexity physical conditions and others.

Besides the question of choosing the most appropriate technique, there are the input or stimulus signal one. The general approach is to apply a known input, voltage or current, to the

electrodes and observe the response, i.e., resulting current or voltage.

The most common form of stimuli is to measure impedance by applying a single-frequency, a pure sinusoidal wave, voltage and measuring the phase shift and amplitude, that correspond to real and imaginary parts of the resulting current flow at that frequency by means of analog circuits or analog-to-digital conversion and signal processing algorithms to analyze the response.

Other techniques and some additional background in impedance measurements are available in (29).

The implemented technique in this work was the auto-balanced bridge, It is an I-V method improved variant, also known as trans-impedance amplifier, that according to (27) is the simplest impedance measurement form, is accurate, has fast response, high signal-to-noise ratio and a stray capacitance immune circuit. Thus, being well suited for high-speed impedance measurements in multiphase flows, and is commonly used in modern low frequencies impedance measurements instruments. Yet, (28) points that this circuitry has already been used with success in ECT systems.

Figure A.2: Auto-balanced bridge circuit implementations.
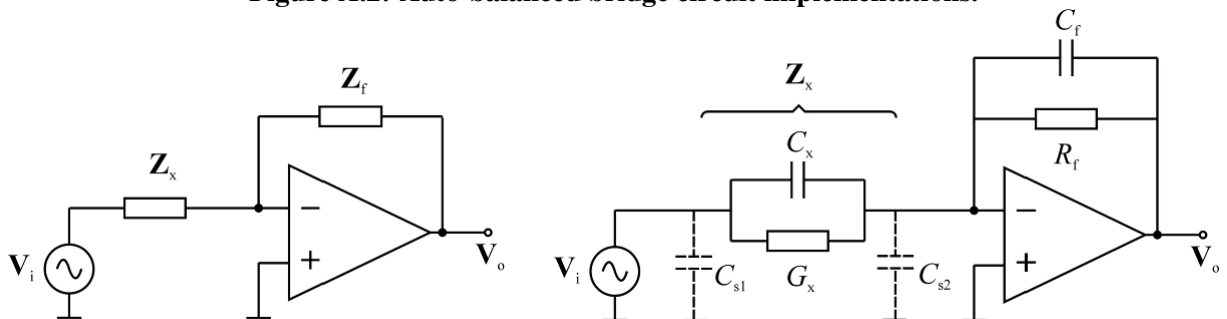
(a) Auto-balanced Bridge basic circuit configuration

(b) Auto-Balanced Bridge pratical implemetation for capacitive impedance measuremt

Source: Adapted from (27, 28, 66)

Figure A.2a present the auto-balanced bridge basic circuit, where $\mathbf{V}_i$ is the excitation voltage, $\mathbf{Z}_x$ represents the unknown impedance and $\mathbf{Z}_f$ the feedback network. The operational amplifier inversion pin potential is maintained at level zero, thus being called virtual ground. In this way, the $\mathbf{Z}_f$ flowing current balances with $\mathbf{Z}_x$ current due to the operational amplifier action, which increases its output voltage to compensate the $\mathbf{Z}_f$ current. Therefore, the impedance can be calculated using the voltage values measured at the operational amplifier output. Since, assuming an ideal operational amplifier, $\mathbf{V}_0$ can be writed as:

$$\frac{\mathbf{V}_0}{\mathbf{V}_i} = \frac{\mathbf{Z}_f}{\mathbf{Z}_x} = -\frac{\mathbf{Y}_x}{\mathbf{Y}_f} \tag{A.12}$$

However, for the practical measurement of capacitance, as this work proposes, a circuit according to presented in A.2b is necessary. Directly based in the Wire Mesh Sensor (WMS) circuitry proposed by (66), the $\mathbf{Z}_x$ and $\mathbf{Z}_f$ impedance are formed by a resistor and capacitor parallel circuit. Although in the practical circuit stray capacitances, designated as C_{s1} and C_{s2}, from connections and cables connected to the measuring circuit can be seen, they have no influence on the measured impedance values. This fact is due to C_{s1} being driven directly between the voltage source and the earth, and C_{s2} being connected to the operational amplifier virtual ground. Following indications from (28), as the scope of the work focus only in the fluid capacitive portion C_x, the G_x is considered null.

By means of replacing eq.(A.3) in eq. (A.12), one obtains:

$$\mathbf{V}_0 = -\mathbf{V}_i\frac{\mathbf{Z}_f}{\mathbf{Z}_x} = -\mathbf{V}_i\frac{\mathbf{Y}_f}{\mathbf{Y}_x} = -\mathbf{V}_i\left(\frac{G_x + j\omega C_x}{G_f + j\omega C_f}\right). \tag{A.13}$$

Being, voltage $\mathbf{V}_0$ proportional to the electric current flowing by the fluid, and the current proportionally inverse to the interrogated impedance $\mathbf{Z}_x$.

APPENDIX B – SYNTHETIC DATA

This appendix bring detailed representation about the synthetic flows generated.

B.1 SYNTHETIC SLUG FLOW

Elongated Bubble:

- Velocity: $2.5 \, \mathrm{m\,s^{-1}}$

- Bubble Length: 2.3 m

- Piston Length: 0.9 m

Dispersed bubbles:

- Velocities: $2.0 \quad 2.9 \, \mathrm{m\,s^{-1}}$

- Bubble length bubbles: 0.5 m

- Pistons Length: 2.0 m

Mean flow characteristics:

- Flow averaged void fraction: 18.5965 %

- Interface averaged transit velocity: $2.48257 \, \mathrm{m\,s^{-1}}$

- Gas volumetric flow rate: $1.648068\text{E-}06 \, \mathrm{m^3\,s^{-1}}$

Figure B.1: Synthetic Slug flow bubble cross-section design
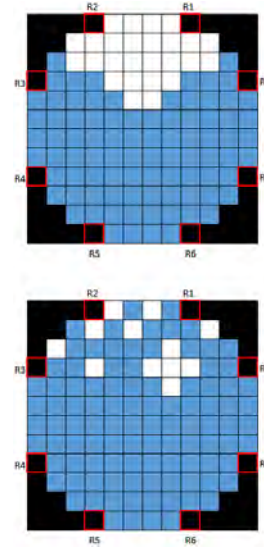
Source: Personal collection.

Figure B.2: Synthetic slug flow parameters
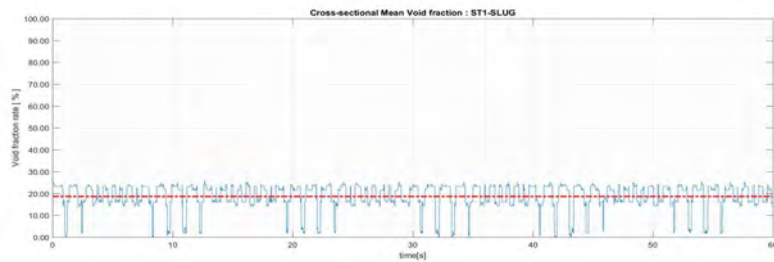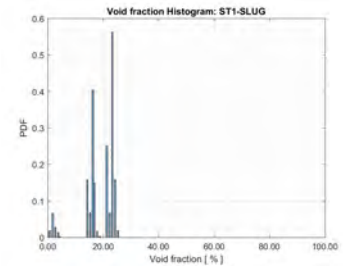
(a) Synthetic slug flow void fraction over time

(b) Synthetic slug flow void fraction hystogram
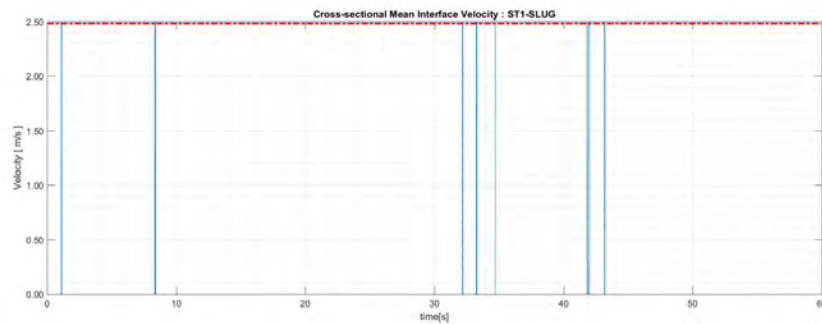
(c) Synthetic slug flow axial velocity
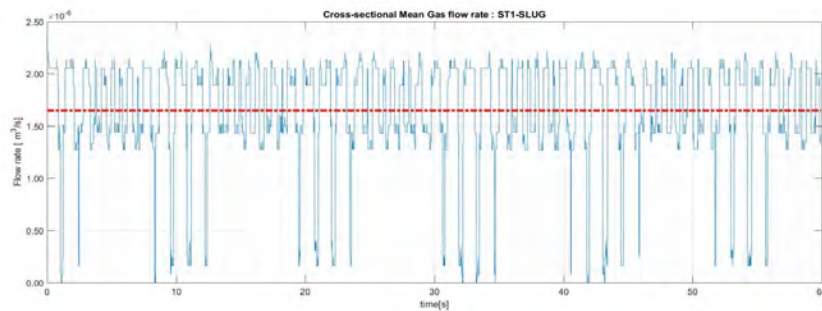
(d) Synthetic slug flow gas flow rate over time

Source: Personal collection.

B.2 SYNTHETIC STRATIFIED FLOW

Elongated Bubble:

- Velocity: $2.5\,\mathrm{m\,s^{-1}}$

- Bubble Length: infinity

- Piston Length: 0 m

Mean flow characteristics:

- Flow averaged void fraction:

Figure B.3: Synthetic Stratified flow bubble cross-section design
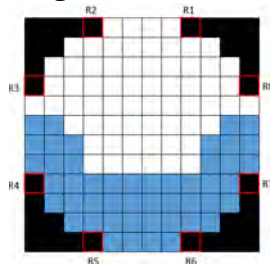
Source: Personal collection.

57.1429 %

- Interface averaged transit velocity: $2.5\,\mathrm{m\,s^{-1}}$

- Gas volumetric flow rate: $5.091013\text{E-}06\,\mathrm{m^3\,s^{-1}}$

Figure B.4: Synthetic Stratified flow parameters
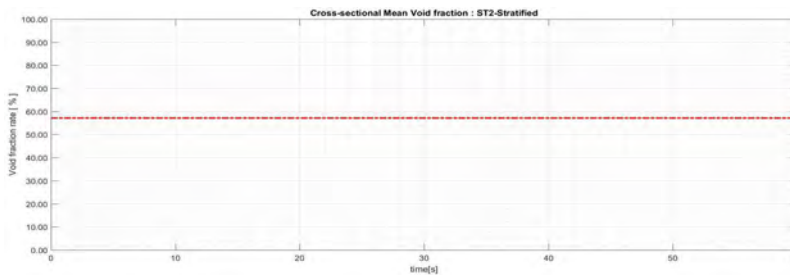
(a) Synthetic Stratified flow void fraction over time
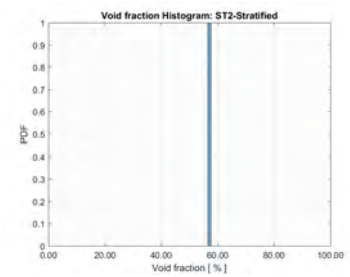
(b) Synthetic Stratified flow void fraction hystogram
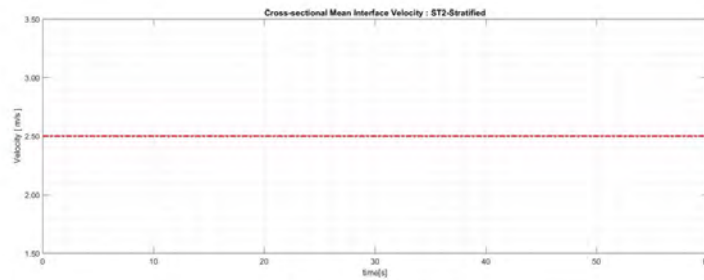
(c) Synthetic Stratified flow axial velocity
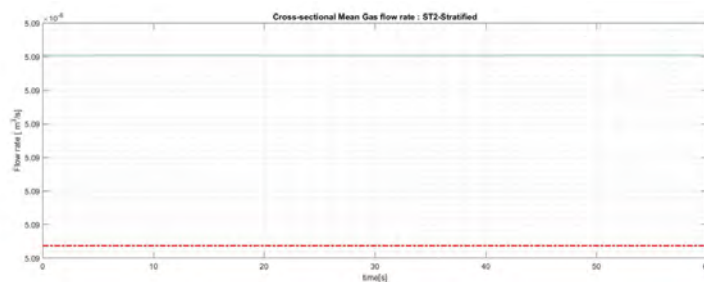
(d) Synthetic Stratified flow gas flow rate over time

Source: Personal collection.

B.3 SYNTHETIC STRATIFIED WAVY FLOW

Elongated Bubble:

- Velocity: $2.5 \, \mathrm{m \, s^{-1}}$

- Bubble Length: 0.25 m

- Piston Length: 0.25 m

Mean flow characteristics:

- Flow averaged void fraction: 52.1334 %

- Interface average transit velocity: $2.5 \mathrm{m \, s^{-1}}$

- Gas volumetric flow rate: $4.633748\text{E-}06 \, \mathrm{m^3 \, s^{-1}}$

Figure B.5: Synthetic Stratified wavy flow bubble cross-section design
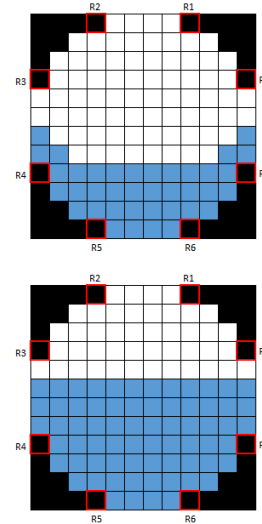
Source: Personal collection.

Figure B.6: Synthetic Stratified wavy flow parameters
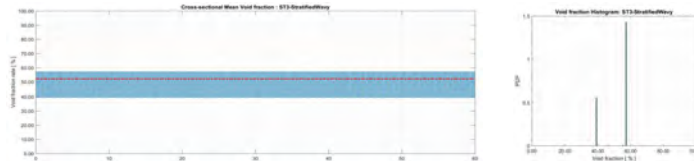
(a) Synthetic Stratified wavy flow void fraction over time

(b) Synthetic Stratified flow wavy void fraction hystogram
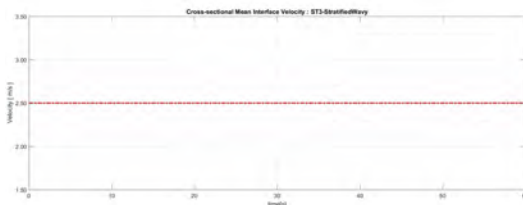
(c) Synthetic Stratified wavy flow axial velocity
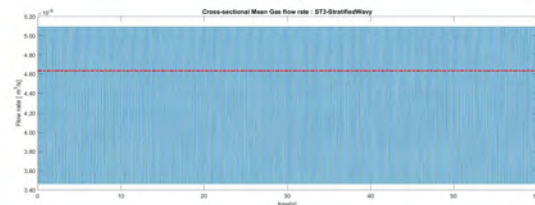
(d) Synthetic Stratified wavy flow gas flow rate over time

Source: Personal collection.

B.4   SYNTHETIC BUBBLY FLOW

Figure B.7: Synthetic Stratified wavy flow bubble cross-section design
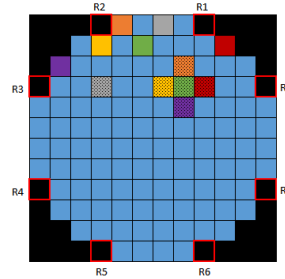
Source: Personal collection.

Bubbles:

- Bubble 1:

    – Velocity: $2.6\,\mathrm{m\,s^{-1}}$

    – Bubble Length: 0.05 m

    – Piston Length: 2 m

- Bubble 2:

    – Velocity: $2.2\,\mathrm{m\,s^{-1}}$

    – Bubble Length: 0.02 m

    – Piston Length: 2 m

- Bubble 3:

    – Velocity: $2.4\,\mathrm{m\,s^{-1}}$

    – Bubble Length: 0.02 m

    – Piston Length: 2 m

- Bubble 4:

    – Velocity: $2.9\,\mathrm{m\,s^{-1}}$

    – Bubble Length: 0.025 m

    – Piston Length: 2 m

- Bubble 5:

- – Velocity: $2.1\,\mathrm{m\,s^{-1}}$
- – Bubble Length: 0.015 m
- – Piston Length: 2 m

- Bubble 6:

   - – Velocity: $2.0\,\mathrm{m\,s^{-1}}$
   - – Bubble Length: 0.3 m
   - – Piston Length: 2 m

- Bubble 7:

   - – Velocity: $2.6\,\mathrm{m\,s^{-1}}$
   - – Bubble Length: 0.25 m
   - – Piston Length: 2 m

- Bubble 8:

   - – Velocity: 2.5m / s
   - – Bubble Length: 0.25 m
   - – Piston Length: 2 m

- Bubble 9:

   - – Velocity: $2.3\,\mathrm{m\,s^{-1}}$
   - – Bubble Length: 0.02 m
   - – Piston Length: 2 m

- Bubble 10:

   - – Velocity: $2.2\,\mathrm{m\,s^{-1}}$
   - – Bubble Length: 0.055 m
   - – Piston Length: 2 m

- Bubble 11:

   - – Velocity: $2.7\,\mathrm{m\,s^{-1}}$
   - – Bubble Length: 0.01 m
   - – Piston Length: 2 m

- Bubble 12:

  – Velocity: $2.0 \mathrm{m\,s}^{-1}$

  – Bubble Length: 0.15 m

  – Piston Length: 2 m

Mean flow characteristics:

- Mean void fraction = 0.5682 %

- Mean Velocity = $1.214776 \mathrm{\ m\,s}^{-1}$

- Volumetric flow = $4.930308\text{E-}08 \mathrm{\ m}^3 \mathrm{\,s}^{-1}$

Figure B.8: Synthetic Stratified wavy flow parameters
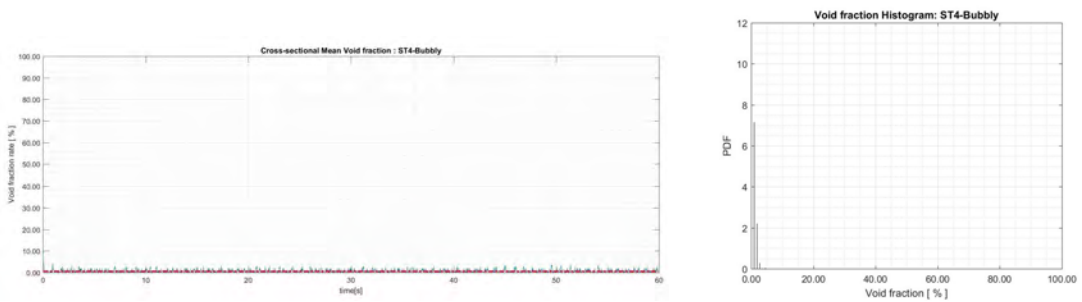
(a) Synthetic Stratified wavy flow void fraction over time

(b) Synthetic Stratified flow wavy void fraction hystogram
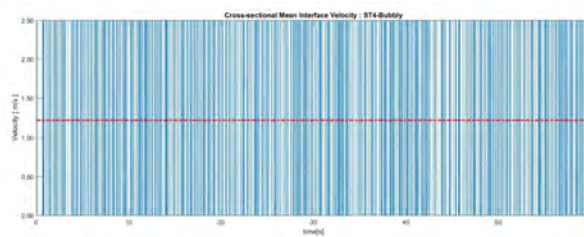
(c) Synthetic Stratified wavy flow axial velocity
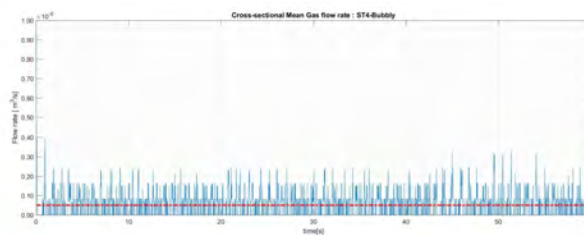
(d) Synthetic Stratified wavy flow gas flow rate over time

Source: Personal collection.

B.5   SYNTHETIC ANNULAR FLOW

Elongated Bubble:

- Velocity: $2.5 \, \mathrm{m\,s^{-1}}$

- Bubble Length: 0.5 m

- Piston Length: 0 m

Figure B.9: Synthetic Stratified wavy flow bubble cross-section design
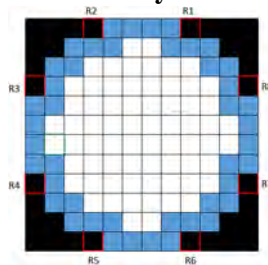
Source: Personal collection.

Mean flow characteristics:

- Flow averaged void fraction: 60.7143 %

- Interface average transit velocity: $2.5\mathrm{m\,s^{-1}}$

- Gas volumetric flow rate: $5.542052\text{E-}06 \, \mathrm{m^3\,s^{-1}}$

Figure B.10: Synthetic Stratified wavy flow parameters
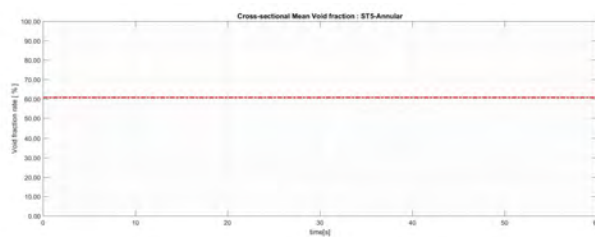
(a) Synthetic Stratified wavy flow void fraction over time
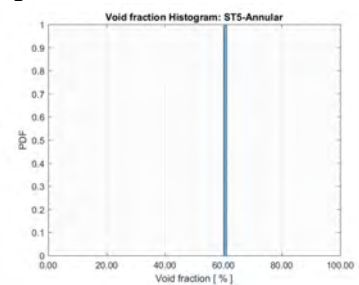
(b) Synthetic Stratified flow wavy void fraction hystogram

Source: Personal collection.

Figure B.11: Synthetic Stratified wavy flow parameters continuation
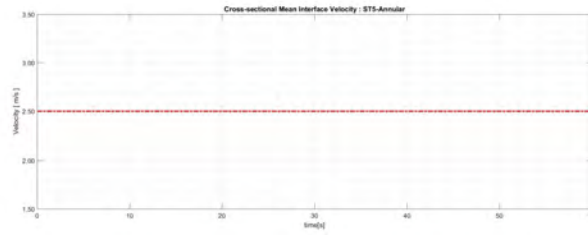
(a) Synthetic Stratified wavy flow axial velocity
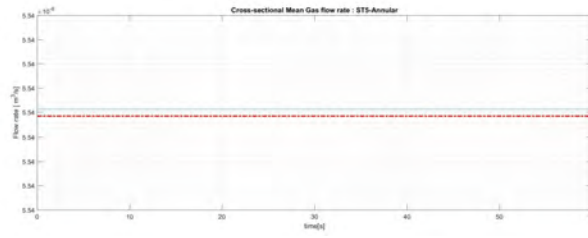
(b) Synthetic Stratified wavy flow gas flow rate over time

Source: Personal collection.

B.6   SYNTHETIC UNNATURAL FLOW

Bubbles:

- Bubble 1:

    - Velocity: $2.5\,\mathrm{m\,s^{-1}}$

    - Bubble Length: 0.5 m

    - Piston Length: 0.5 m

- Bubble 2:

    - Velocity: $4.5\,\mathrm{m\,s^{-1}}$

    - Bubble Length: 0.5 m

    - Piston Length: 0.5 m

- Bubble 3:

    - Velocity: $1.5\,\mathrm{m\,s^{-1}}$

    - Bubble Length: 0.5 m

    - Piston Length: 0.5 m

Figure B.12: Synthetic Slug flow bubble cross-section design
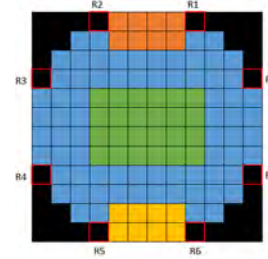
Source: Personal collection.

Mean flow characteristics:

- Mean void fraction = 17.9520 %

- Mean Velocity = $2.611522\,\mathrm{m\,s^{-1}}$

- Volumetric flow = $2.265860\text{E-06}\,\mathrm{m^3\,s^{-1}}$

Figure B.13: Synthetic slug flow parameters
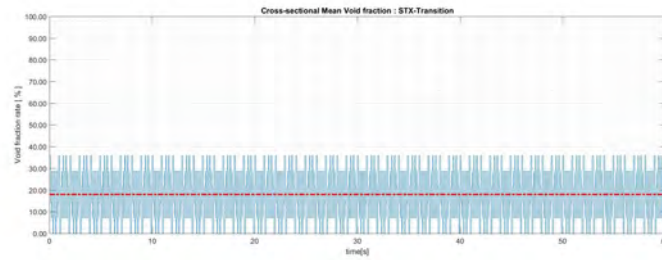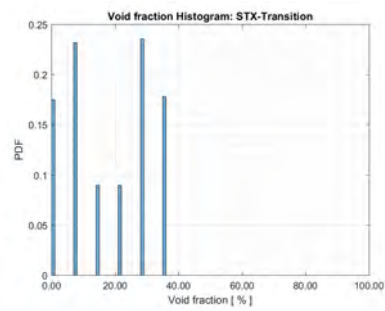
(a) Synthetic slug flow void fraction over time

(b) Synthetic slug flow void fraction hystogram
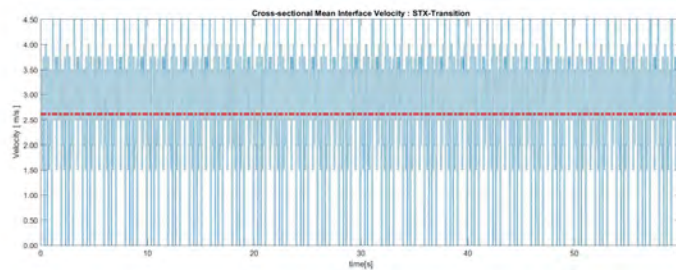
(c) Synthetic slug flow axial velocity
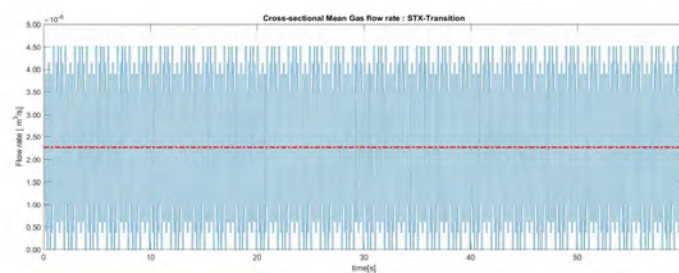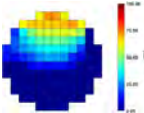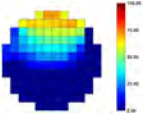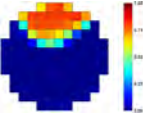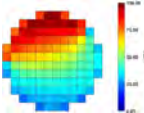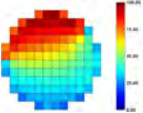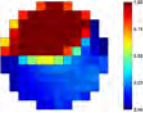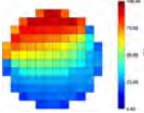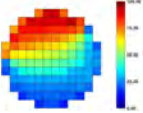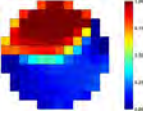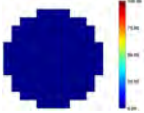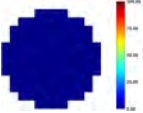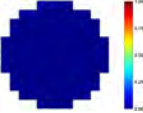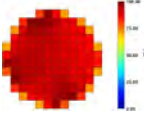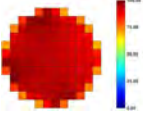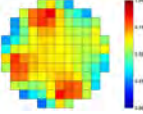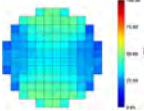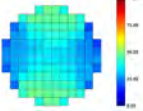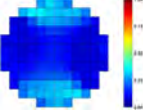
(d) Synthetic slug flow gas flow rate over time

Source: Personal collection.

B.7   RECONSTRUCTION RESULTS

This section brings more detailed results about the tests done with the reconstruction algorithms parameters and present the velocity profiles generated.

Table B.1: Void fraction profile estimations for the synthetic flows

Flow	Reference	Reconstruction		
		LBP	nBP	LIM
Slug flow	$\overline{\alpha_G} = 18.60\%$			
Stratified flow	$\overline{\alpha_G} = 57.14\%$			
Stratified Wavy	$\overline{\alpha_G} = 53.13\%$			
Bubbly flow	$\overline{\alpha_G} = 0.57\%$			
Annular flow	$\overline{\alpha_G} = 60.71\%$			
Unnatural flow	$\overline{\alpha_G} = 17.95\%$			

Velocity reconstructions

Table B.2: Synthetic velocities profiles reconstructions

Flow	Reference	Rec. Algorithm	Vel. Algorithm		
			CCOV	SAD	SSD
Synthetic Slug		LBP			
		NBP			
		LIM			
Synthetic Stratified		LBP			
		NBP			
		LIM			

Table B.2 continued from previous page
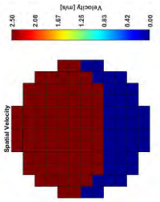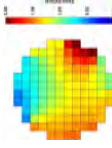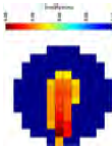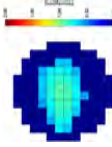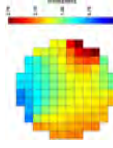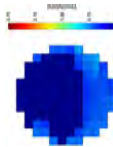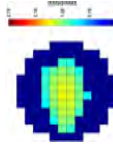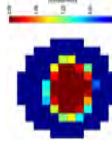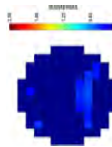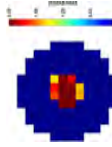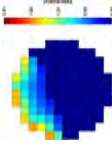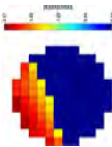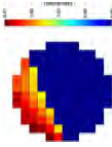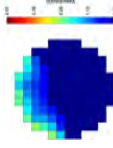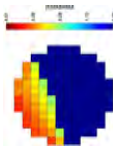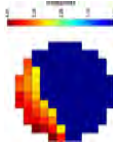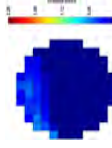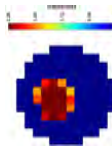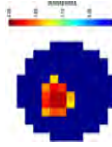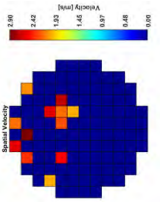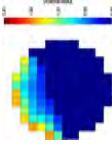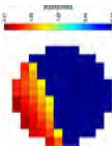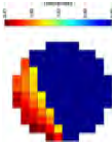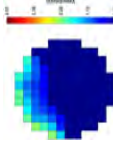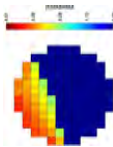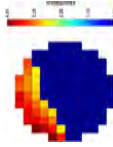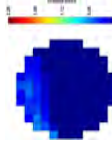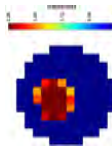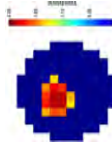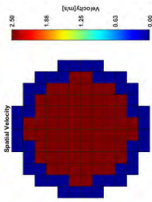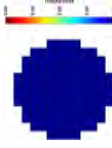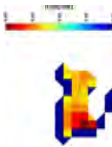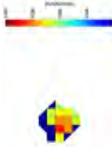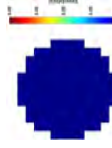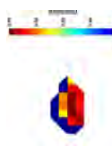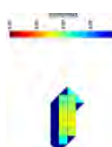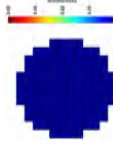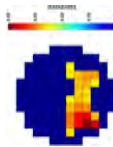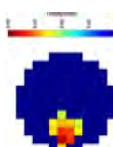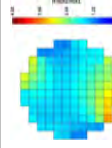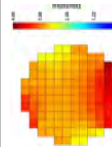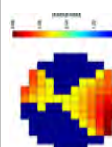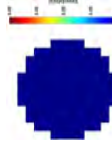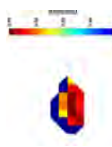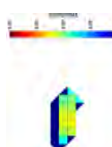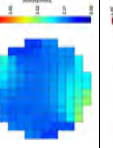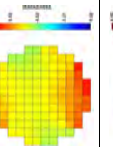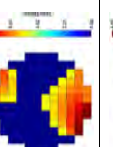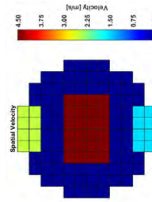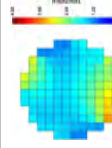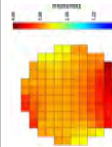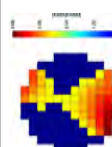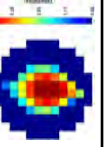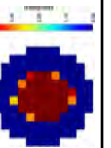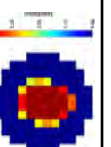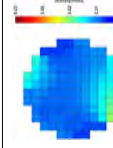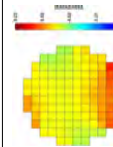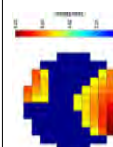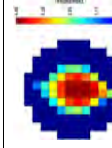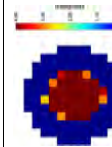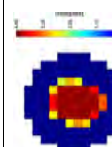
Flow	Reference	Rec. Algorithm	Vel. Algorithm		
			CCOV	SAD	SSD
Synthetic Stratified Wavy		LBP			
		NBP			
		LIM			
Synthetic Bubbly flow		LBP			
		NBP			
		LIM			

Table B.2 continued from previous page

Flow	Reference	Rec. Algorithm	Vel. Algorithm		
			CCOV	SAD	SSD
Synthetic Annular flow		LBP			
		NBP			
		LIM			
Synthetic Unnatural flow		LBP			
		NBP			
		LIM			

APPENDIX C – EXPERIMENTAL DATA

This appendix bring complementary information about the experimental flow analysis. These charts were placed in this section because, as mentioned in chapter 4, the facility instrumentation did not directly provide data for velocity and void fraction comparison. Therefore, these comparisons were not included in the main text. However, to illustrate the behavior of the reconstructions for velocity and void fraction this appendix was created.
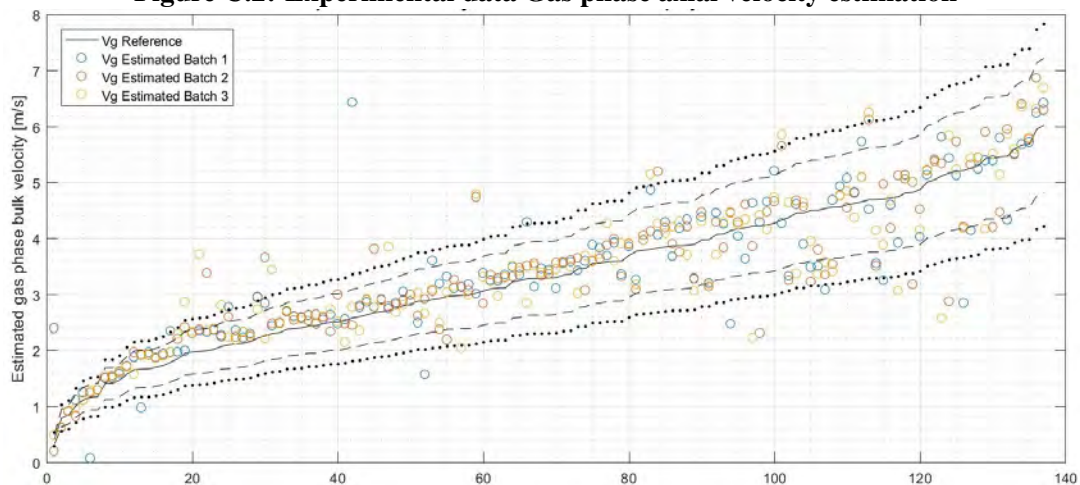
It is possible to observe the dependence off the flow pattern acting on the different parameters in the Figures C.2 and , which corroborates with the hypotheses raised in the text for the uncertainties.

Figure C.1: Experimental data Void fraction estimation
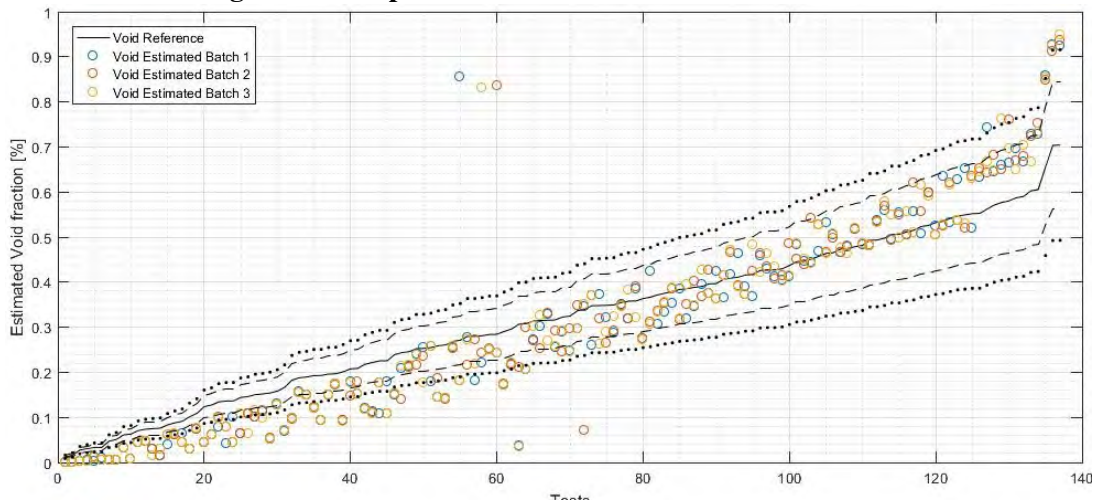
Source: Personal collection.

Figure C.2: Experimental data Gas phase axial velocity estimation

Source: Personal collection.